PRIMARY ELECTRIC PROPULSION TECHNOLOGY STUDY

R.L. Poeschel and J.R. Beattie

Hughes Research Laboratories
3011 Malibu Canyon Road
Malibu, CA 90265

November 1979

Contract NAS 3–21040

Final Report

For period 13 September 1977 through 13 June 1979

Sponsored By
NATIONAL AERONAUTICS AND SPACE ADMINISTRATION
Lewis Research Center
21000 Brookpark Road
Cleveland, OH 44135

TECHNICAL REPORT STANDARD TITLE PAGE

1. Report No.	2. Government Accession No.	3. Recipient's Catalog No.
NASA CR-159688		

4. Title and Subtitle	5. Report Date
PRIMARY ELECTRIC PROPULSION TECHNOLOGY STUDY	November 1979
	6. Performing Organization Code

7 Author(s)	8. Performing Organization Report No.
R.L. Poeschel and J.R. Beattie	

9. Performing Organization Name and Address	10. Work Unit No.
Hughes Research Laboratories 3011 Malibu Canyon Road Malibu, CA 90265	11. Contract or Grant No. NAS 3-21040

12. Sponsoring Agency Name and Address	13. Type of Report and Period Covered
National Aeronautics and Space Administration Lewis Research Center 21000 Brookpark Road Cleveland, OH 44135	Final Report 13 Sept 1977-13 June 1979
	14. Sponsoring Agency Code

15. Supplementary Notes

Project Manager: William R. Kerslake, NASA Lewis Research Center, Cleveland, Ohio

16. Abstract

The Primary Electric Propulsion Technology Study was a program for investigating the 30-cm engineering-model-thruster technology with emphasis placed on the development of models for understanding and predicting the operational characteristics and wear-out mechanisms of the thruster as a function of operating or design parameters. The study was divided into four independent tasks. Task 1 was an investigation of the wear mechanisms and wear rates that determine the useful lifetime of the thruster discharge chamber. The effect of varying operating and design parameters was explored, and a sputter-erosion model was formulated to relate wear rates to the dominant factors. Task 2 was an investigation of cathode lifetime as determined by the depletion of barium from the barium-aluminate-impregnated-porous-tungsten "insert" that serves as a barium reservoir. Cathode emission current was determined to be the major controlling factor, and a model was formulated relating cathode lifetime to cathode emission current. Task 3 was a study of accelerator-grid-system technology. The capability of describing accelerator-grid-system performance for the 30-cm thruster depends on gaining an understanding of grid deformation under thermal stress. A model for finite-element structural analysis of the 30-cm accelerator-grid system was developed, and preliminary results were obtained. Task 4 was a verification of the high-voltage propellant-flow-electrical-isolator design developed under NASA contract NAS 3-20395 for operation at 10-kV applied voltage and 10-A equivalent propellant flow with mercury and argon propellants. A model was formulated for predicting performance.

17. Key Words (Selected by Author(s))	18. Distribution Statement
Electric Propulsion 30-cm Ion Thruster Ion Sputtering Hollow Cathode Lifetime Ion Beams	UNCLASSIFIED — Unlimited

19. Security Classif. (of this report)	20. Security Classif. (of this page)	21. No. of Pages	22. Price*
UNCLASSIFIED	UNCLASSIFIED	181	

*For sale by the Clearinghouse for Federal Scientific and Technical Information, Springfield, Virginia 22151.

FOREWORD

The work described in this report was performed in the Ion Physics Department of Hughes Research Laboratories, a division of Hughes Aircraft Company. The Ion Physics Department is managed by Dr. J. Hyman. The work was performed under Contract NAS 3-21040, monitored by Mr. William R. Kerslake of NASA Lewis Research Center. Major technical contributions to this effort were made by:

R.L. Poeschel	Project manager and principal investigator
J.R. Beattie	Assistant project manager, discharge-chamber and ion-optics studies
P.A. Robinson, Jr.	Hollow-cathode and propellant-isolator studies
J.W. Ward	Ion-optics computer modeling
S. Kami	Ion-optics design, fabrication, and structural analysis
M.J. Burns	Instrumentation design, data collection and analysis
J. Mullane and J. Tyrrell	Data collection, instrumentation, and technical assistance

SUMMARY

The Primary Electric Propulsion Technology Study was an investigation of ion-thruster technology that is representative of the "state of the art" with the goal of formulating models for describing the capabilities and limitations of thruster performance. The work was conducted under four relatively independent tasks. The first and most important task was that of relating thruster discharge chamber wear rates and mechanisms to thruster operating parameters and ambient test-facility conditions. The second task was to explore the factors that limit the lifetime of thruster hollow cathodes. The third task called for relating the performance capabilities of the ion-accelerator grid system to the ion-optics design variables and operating parameters. The fourth task was that of continuing verification of propellant electrical isolator concepts and formulating a model to describe operating principles. The work reported here built on the results obtained under preceeding or concurrent NASA contracts (NAS 3-19703, NAS 3-20395, NAS 3-21052, NAS 3-21357, and NAS 3-18914). In 3 of the 4 tasks, performance descriptions were developed that are quite adequate for describing the LeRC/Hughes 30-cm mercury-ion-thruster technology.

In the first task, the major factors that affect discharge chamber lifetime were identified and quantitative relationships were developed for assessing wear rates and ultimate thruster lifetime. Factors that were investigated included thruster operating parameters (such as discharge voltage, discharge power, beam current, etc.), thruster design parameters (magnetic field configuration, accelerator grid transmission, etc.), and contaminant gases present in the testing environment (nitrogen, argon, methane, etc.). Nearly every parameter explored has some effect on wear rate, although the most important factors are discharge voltage, beam current, doubly charged ion density, magnetic field geometry, surface material, and the reactive contaminant gases present in the test environment.

The cathode-lifetime investigation performed here completed a performance model that relates the temperature of the barium dispensing porous-tungsten "insert" to thruster operating parameters. The most important variable in determining insert temperature was found to be cathode emission current. The performance model developed relates the lifetime of the cathode to the cathode emission current and the barium available within the porous-tungsten insert. The experiments performed also demonstrated that cathode emission properties (and insert temperature) are not sensitive to the changes in the thruster discharge-chamber properties that occur when an ion beam is extracted. Consequently, the results of hollow cathode research and testing performed under non-thruster conditions should be applicable to thruster cathodes provided that the voltages and currents are similar.

The investigation of accelerator-grid-system technology produced several of the prerequisites for formulating a performance model, but a comprehensive model was not obtained. In fact, we found that the accelerator-grid-system design would benefit from additional development before further efforts are invested in performance modeling. The principal requirement identified was for supporting the screen and accelerator grids in a manner that will withstand launch vibration, yet will permit thermal expansion of the grids without causing their deformation.

The high-voltage propellant-isolator design developed under a previous NASA contract (NAS 3-20395) was verified for operation at applied voltages greater than 10 kV and internal propellant pressure equivalent to more than 10-A equivalent propellant flow. Testing showed that the insulator deterioration observed previously was an anomalous event. No increase in leakage current was observed in a test of over 1,600 hr under this program. The isolator operated equally well with argon or mercury vapor. Voltage division measured across the isolator chambers was not linear and was governed by capacitive effects (at least for the

isolator that was instrumented for measuring voltage division). Although the analytic description of isolator behavior was not totally successful (since experimental data are required for determining the capacitance values), the high-voltage isolator design was verified empirically for the range of operation for which it was designed.

TABLE OF CONTENTS

LIST OF ILLUSTRATIONS

SECTION 1

INTRODUCTION

By the beginning of the present program, the technology of the LeRC/Hughes 30-cm mercury ion thruster had attained a relatively high level of maturity. The overall goals of the program were to consolidate the available thruster test results, perform experiments to complete the data base, and formulate analytic and descriptive models for characterizing the performance capabilities and limitations of the 30-cm thruster.

A. PROGRAM GOALS

The work was performed under four independent tasks. Task 1 required a formulation of the dependence of discharge-chamber wear rates on discharge-chamber design and operating parameters (and also on ambient test facility conditions). Task 2 required identification of factors that determine cathode lifetime. Task 3 required development of a description of the accelerator grid system performance capabilities and limitations. Task 4 required verification of a high-voltage (10 kV), high-current (10 A equivalent) propellant electrical isolator. Under each task, a performance model was to be developed that would provide an adequate description of the performance expected from a "state-of-the-art" thruster and would also enable predicting performance limitations. At the beginning of the study, the scope of each task was defined. Initial results obtained under this program, augmented by results obtained under other programs (NASA Contracts NAS 3-21052 and NAS 3-21357), increased the range of phenomena* that had to be considered under Tasks 1 and 3. Consequently, satisfying the goals of these tasks became more demanding than initially anticipated.

---

* In Task 1 it was found that all the reactive gases subjected to preliminary testing affected screen-grid wear rates, and in Task 3 it was found that a thermo-mechanical model of the accelerator system was necessary.

B. PROGRAM ACCOMPLISHMENTS

Under Task 1, the effects of ambient test conditions on discharge-chamber wear rates were thoroughly explored and quantitatively documented to validate the investigation of other parameters that affect wear rates. The effects of thruster operating parameters and thruster design parameters were investigated and a model was formulated for estimating discharge-chamber lifetime as a function of the more important parameters.

Under Task 2, a conceptual model of cathode operation was used to relate cathode lifetime to the temperature of the impregnated porous-tungsten insert. Tests were performed to determine which of the possible operational variables affect insert temperature. Cathode lifetime was ultimately found to be dependent primarily on cathode emission current.

Work under Task 3 led to the realization that accelerator grid system technology is not as mature as was originally thought. Performance of the accelerator grid system is critically dependent on the spacing between the grids. Existing data and analyses indicated that this spacing is strongly dependent on the temperature of the accelerator grids and their mounting ring. Progress was made in analytic modeling of the accelerator grid structure to determine the interelectrode spacing under thermal stress. The work performed here in effect established the basis for design of an improved mounting system instead of describing the state-of-the-art performance capabilities.

Task 4 efforts produced the empirical data required for verifying the high-voltage propellant-flow electrical-isolator design; however, some of the test results were rather unexpected. First, the isolator breakdown voltage was in excess of that anticipated. Second, the voltage division was found to be governed by capacitive rather than resistive effects. Therefore, the performance model developed requires the specification of capacitance values that would be difficult to determine for an operational propellant electrical isolator (as compared to one that is instrumented for test).

The work performed under each of the study tasks is described in detail in the following sections, one section being devoted to each task. The report also describes work performed under Hughes funding that enabled the contractual investigation to proceed more effectively.

Page intentionally left blank

SECTION 2

DISCHARGE-CHAMBER AND SCREEN-GRID EROSION

Throughout the evolution of the J-series 30-cm thruster, models have been formulated to describe the operation or performance of the thruster and many of its components. These models have increased our understanding of the operation of various elements of the thruster system and have made it possible to extrapolate beyond the normal operating envelope with a high degree of confidence. An example of this capability is a model developed from performance data obtained from measurements using the engineering-model thruster operated at a nominal specific impulse of 3000 sec. The success of this model in predicting the performance characteristics of an extended-performance thruster configuration was demonstrated under NASA Contract NAS 3-20395.[2-1] The model has since proven invaluable for various high-performance mission applications. A question that invariably arises when considering applications of the current thruster design or of an extended-performance version is that of lifetime. Since the lower lifetime limit of the 30-cm thruster is thought to be determined by sputter erosion of the interior surfaces of the discharge chamber, an understanding of the chamber-erosion phenomena is essential to the development of a model of thruster lifetime. This section presents the results of an investigation of parameters that affect the erosion rates of critical components of the 30-cm thruster. Based on measured experimental results, a model of sputter erosion is formulated in terms of the design, operational, and material characteristics of the thruster.

A. FACTORS CONSIDERED

Various factors known to affect the wear rates of critical discharge-chamber components were considered when planning the experimental investigation of sputter-erosion phenomena occurring in the 30-cm thruster. These factors, which included material, design, operational, and ambient (or facility-related) characteristics, are discussed in detail in Sections 2.A.1 through 2.A.4.

1. Thruster Operating Conditions

The thruster operating conditions that are thought to be most important in determining internal chamber wear rates are beam current and discharge (anode) voltage. The beam-current operating point determines the plasma density, which specifies the ion-arrival rate at the internal surfaces of the discharge chamber. The product of the effective ion-arrival rate and surface sputtering yield determines the rate of removal of surface material and the lifetime of the component under consideration. Short-term erosion-rate measurements conducted under NASA Contract NAS 3-19703[2-2] verified the anticipated increase in component erosion rate with beam current and demonstrated that the relationship is nonlinear. This nonlinearity is the result of an increase in the relative concentration of doubly charged ions that accompanies the increase in plasma density. Doubly charged ions have a substantially higher sputtering rate since they impact surfaces with twice the energy of singly charged ions, and the sputtering yields of materials commonly used in discharge chamber construction increase exponentially with ion energy in the low-energy range. The discharge voltage strongly affects chamber wear rates since this parameter determines the plasma potential, which in turn specifies the energy of the ions striking the chamber surfaces.

2. Thruster Design

Various aspects of thruster design were considered during the investigation of discharge-chamber and screen-grid erosion. For example, the discharge chamber of the thruster (SN 301) used for the majority of the investigation was modified to duplicate as closely as possible the interior geometry of the current J-series thruster design. These modifications included:

- Use of J-series (SHAG) electrodes.
- Installation of J-series cathodes, anode pole piece, baffle assembly, and sintered-mesh anode.
- Use of tantalum cladding on the baffle and cathode pole piece, and installation of wire-mesh flake control on the discharge-chamber backplate.

Figure 2-1, a photograph of the SN 301-J discharge chamber, illustrates the internal modifications listed above. It also shows the ion-optics mounting ring, which is electrically isolated from the thruster body, enabling the screen electrode to be biased with respect to surfaces at cathode potential.

Thruster design variables that are known to affect chamber wear rates strongly are the accelerator-electrode design and the plasma-density distribution. The open-area fraction of the accelerator electrode controls the neutral density within the chamber, and the concentration of doubly charged ions varies inversely with neutral density. A reduction in the open area of the accelerator electrode permits the neutral density within the chamber to be increased, which reduces the doubly charged ion density and chamber wear rates. The increase in neutral density also allows the discharge voltage to be reduced while maintaining constant propellant utilization. The reduction in discharge voltage further reduces wear rate by reducing the plasma potental and the rate-of-production of doubly charged ions. During this study, the effects of accelerator-electrode open-area fraction were investigated by performing short-term erosion-rate measurements using ion-optics assemblies that are representative of the 900- and J-series thruster designs (open-area fractions of 43% and 23%, respectively).

The effects of the plasma-density distribution on chamber wear rates were investigated using two alternate discharge-chamber designs. Since the rate-of-production of ions is proportional to the densities of both species involved (i.e., electrons and atoms), an increase in the production rate should be possible by increasing the density of either species. In this manner it may be possible to increase the ion density near the cylindrical chamber boundary, permitting the ion density and wear rates on-axis to be reduced (at constant beam current). The electron density

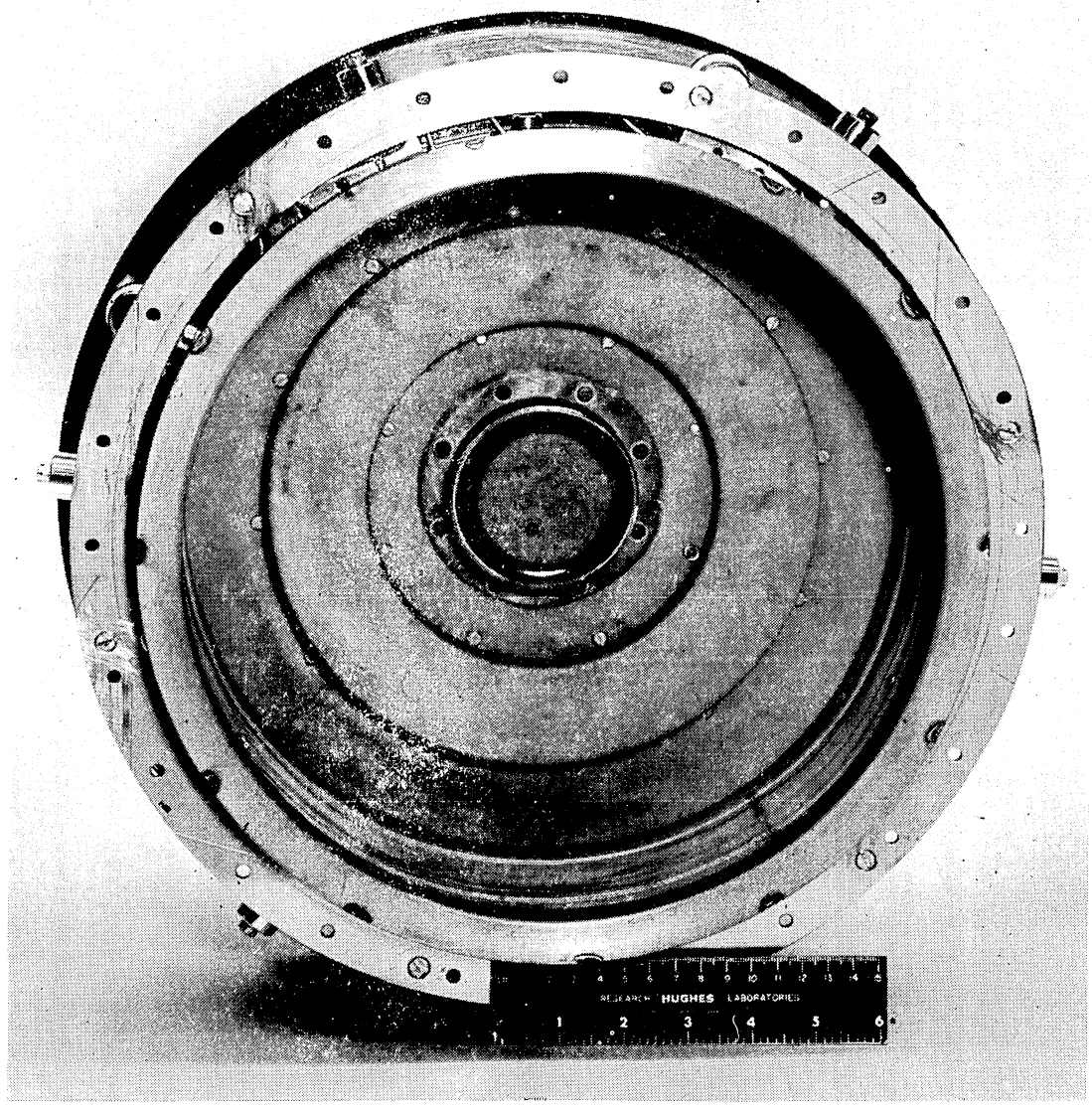

Figure 2-1. Photograph of SN 301-J thruster.

distribution is determined to a large extent by the geometry of the magnetic field existing within the chamber, since the magnetic field lines tend to "guide" the energetic electrons entering the chamber from the cathode-discharge plasma region. This aspect of controlling the plasma-density distribution was investigated using an alternate discharge-chamber design that employs a single-cusp-magnetic-field geometry to distribute and control the energetic ionizing electrons. This arrangement should produce a uniform plasma-density distribution and lower the erosion rate near the chamber axis. The other approach to altering the plasma-density distribution that we investigated during this study employed an anode geometry that was intended to increase the residence time of neutrals near the cylindrical chamber boundary. Results obtained using these alternate discharge-chamber geometries are presented in Section 2.C.9.

3. Fabrication Materials

The choice of materials for use in fabricating critical ion-thruster components is extremely important to lifetime considerations since the sputtering yield and number density of the material determine the wear rate of a given surface. The current J-series thruster design employs either molybdenum or tantalum for critical life-limiting components. However, there are other low-sputter-yield materials (such as niobium and tungsten) that might also be suitable for fabricating life-limiting components. Several low-sputter-yield metals were investigated during this study in an attempt to identify alternate materials for use in fabricating critical discharge-chamber components (such as the screen electrode).

4. Vacuum-Test-Chamber Residual Gases

The effects of vacuum-test-chamber residual gases on the erosion rates of thruster components must be understood in order to extrapolate the results of erosion-rate measurements conducted in vacuum chambers

to the near-perfect vacuum of space. Previous results[2-3] of an investigation of the effects of facility residual gases on the wear rate of the screen electrode indicated that the presence of a sufficient quantity of nitrogen can reduce the erosion rate of molybdenum. This reduction is apparently caused by the chemisorption of nitrogen atoms onto the surface, producing a molybdenum-nitrogen compound such as Mo_2N. Because of this surface coverage, the metallic sputtering rate is much lower than the value corresponding to a "clean" molybdenum surface. During the present investigation, the effects of residual gases on chamber wear rates were extended to include additional gases (such as oxygen, carbon dioxide, methane, cyanogen, and water vapor) that are commonly found in oil-diffusion-pumped vacuum chambers. The purpose of these tests was (1) to determine whether these gases have an effect on the wear rate of critical chamber components, (2) to determine the maximum partial pressure necessary to simulate the surface sputtering rates expected in space, and (3) to obtain quantitative measurements of the effects of facility-residual-gas pressure on the sputtering rate of critical discharge-chamber components.

B. MEASUREMENT TECHNIQUES

The experimental investigation of discharge-chamber and screen-grid erosion involved a variety of optical, pressure, wear-rate, and plasma-diagnostic measurements. The experimental apparatus and techniques used in performing these measurements are described below.

1. Optical Spectroscopy

The thin-film erosion-monitor technique (described in detail in Section 2.B.5) provides estimates of critical component lifetimes in test durations of less than 1/1000 that of the thruster design lifetime. Although this method is short term in comparison with the 15,000-hr lifetime goal of the J-series thruster, it requires approximately four days per test point for thruster setup, testing, and interpretation of results. Therefore, in an experimental investigation that involves many test parameters and large numbers of erosion-rate measurements, a fast

technique of assessing relative erosion rates is required. Optical spectroscopy provides a fast and nonperturbing means of obtaining plasma-diagnostic and relative-erosion-rate data. The usefulness of the spectroscopic approach in these applications has been demonstrated in past studies conducted by investigators at Hughes[2-3] and NASA LeRC.[2-4] The approach is based on the fact that excited atoms decay to the ground state by the spontaneous emission of radiation. The differences in energy of the two levels determines the wavelength of the emitted light; for optically thin plasmas, the intensity of the line observed at this wavelength is proportional to the density of the excited atoms. Excitation of these atoms occurs through electron bombardment of the ground-state atoms which are produced by sputter erosion of surfaces within the chamber, and, therefore, the measured line intensity is proportional* to the sputtering rate of the surface material. The line intensities corresponding to excited atoms such as molybdenum are conveniently measured using a monochromator equipped with a photomultiplier.

The physical arrangement of the optical system used in this study is presented in Figure 2-2. The thruster discharge chamber is viewed through a quartz window located at the downstream end of the vacuum chamber approximately 9° off-axis. Light passing through the window is collected by the first lens and focused onto the plane of the mask holder by the mirror and lens arrangement shown in the figure. Masks consisting of Plexiglass painted black in regions where light transmission is undesirable are placed in the holder, permitting light from selected regions of the discharge chamber to be focused onto the entrance slit of the monochromator using the lens arrangement indicated. Four masks were used in the measurements, permitting light from the entire discharge chamber or from equal-area regions located at the center and at one-half and two-thirds of the chamber radius to reach the entrance slit. The monochromator is equipped with a photomultiplier tube whose output

*The constant of proportionality varies with thruster operating conditions (such as discharge voltage V_D and beam current J_b) that influence the degree of excitation of the sputtered atoms.

8991–14R1

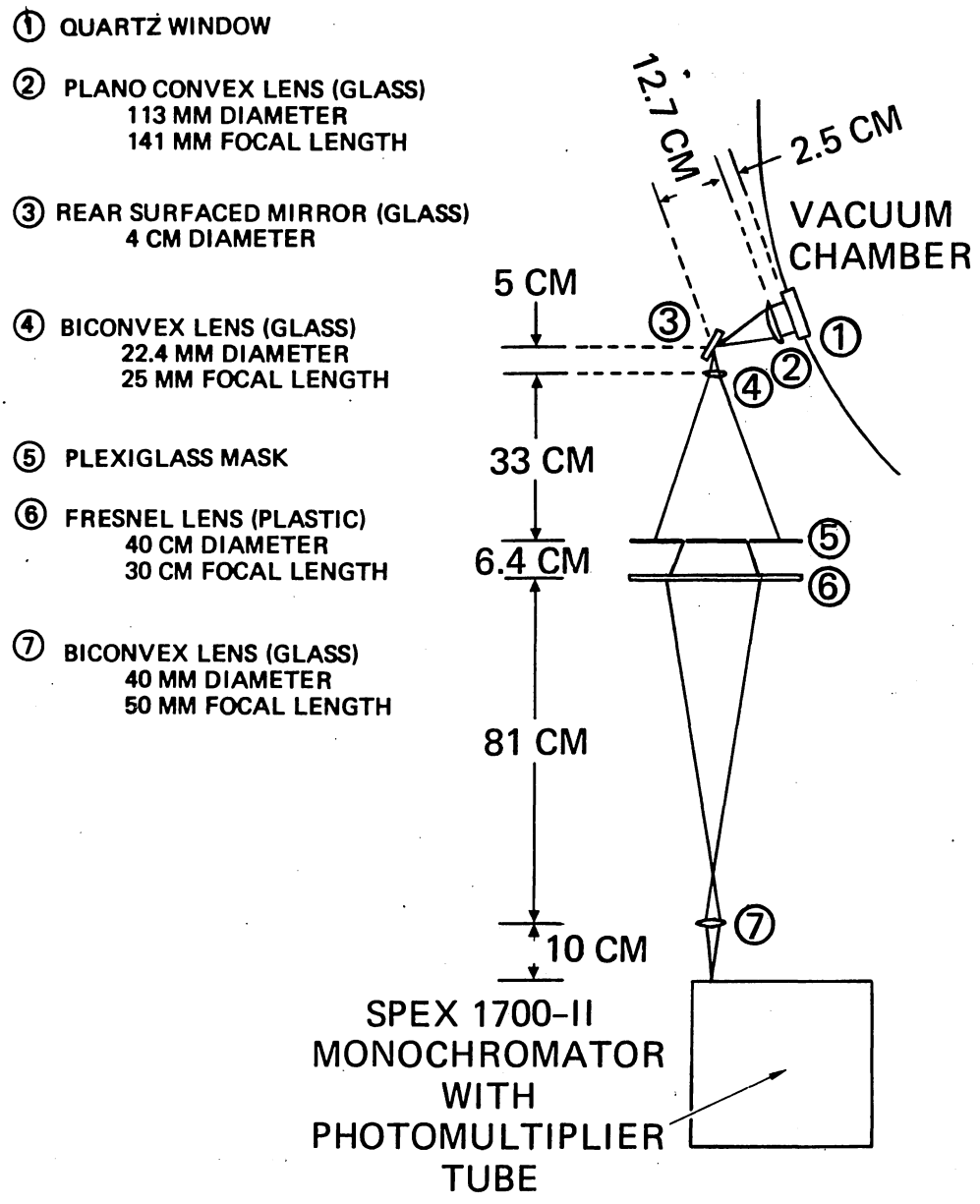

Figure 2-2. Optical setup used for measuring spectral line intensities.

current is measured using an electrometer. This signal is recorded along with a signal proportional to wavelength on either an x-y plotter or a strip-chart recorder. Wavelength variation is achieved through motorized control of the diffraction grating.

Monochromators having focal lengths of 1/4, 1/2, and 3/4 m were investigated at the beginning of the program: 3/4 m gave the best resolution of the three principal lines (corresponding to MoI, HgI, and HgII) in the wavelength range 3798 Å $\leq \lambda \leq$ 3807 Å. A 3/4-m Spex monochromator equipped with a Czerny-Turner side-by-side mount was used for all measurements obtained during this program. Figure 2-3 presents a typical variation of intensity versus wavelength for the three principal lines using 10-μm slit widths at the entrance and exit of the monochromator. The resolving power calculated from the center peak of Figure 2-3 is approximately $\lambda/\Delta\lambda = 4000$.

The useful wavelength range of the setup illustrated in Figure 2-2 is 3600 Å $\leq \lambda \leq$ 6000 Å, with the limits determined by one or more of the following limitations: (1) the transmission range of the glass lens system, (2) the grating efficiency of the monochromator, and (3) the spectral response of the phototube. The lines of interest in this investigation are listed in Table 2-1 according to species, wavelength, and relative intensity. The first three lines are of major interest since they are closely spaced in wavelength (minimizing wavelength scan-time) and provide an indication of the erosion rate of the molybdenum screen grid. A tantalum line indicative of the erosion rate of the baffle and pole piece is also of interest, but, unfortunately, the strongest tantalum lines occur at wavelengths below 3600 Å, which is the lower limit of the optical system used in this study.

2. Residual Gas Analysis

A quadrupole residual gas analyzer was used to measure the relative abundance of background gases in the Hughes 9-ft vacuum test chamber. This instrument was also used to perform partial-pressure measurements of various test gases that were introduced into the chamber. Figure 2-4 presents a sketch of the vacuum facility showing the relative location

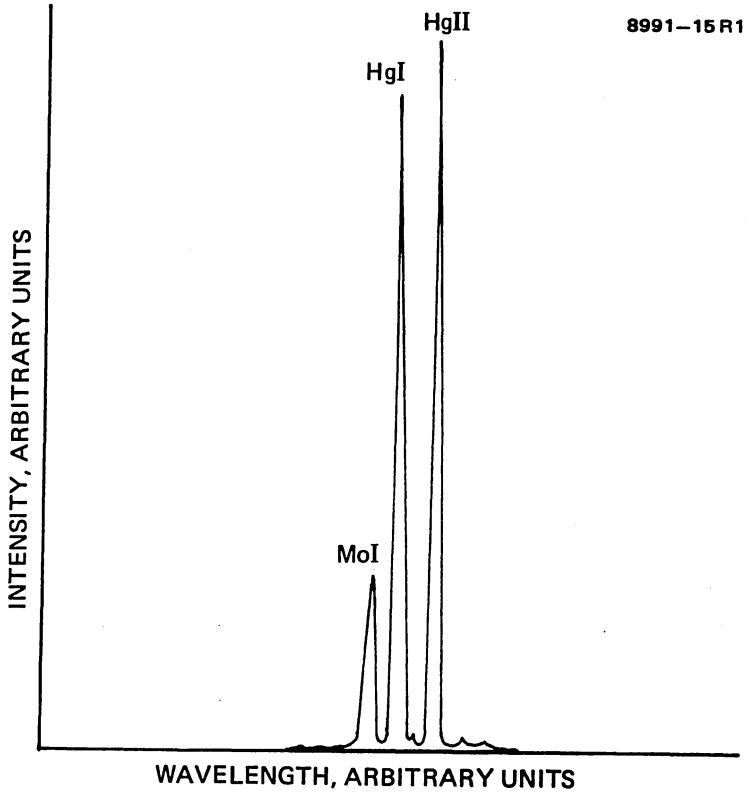

Figure 2-3.
Typical variation of line intensity versus wavelength showing the resolution of the MoI, HgI, and HgII lines at wavelengths of λ = 3798.3 Å, 3801.7 Å, and 3806.4 Å, respectively.

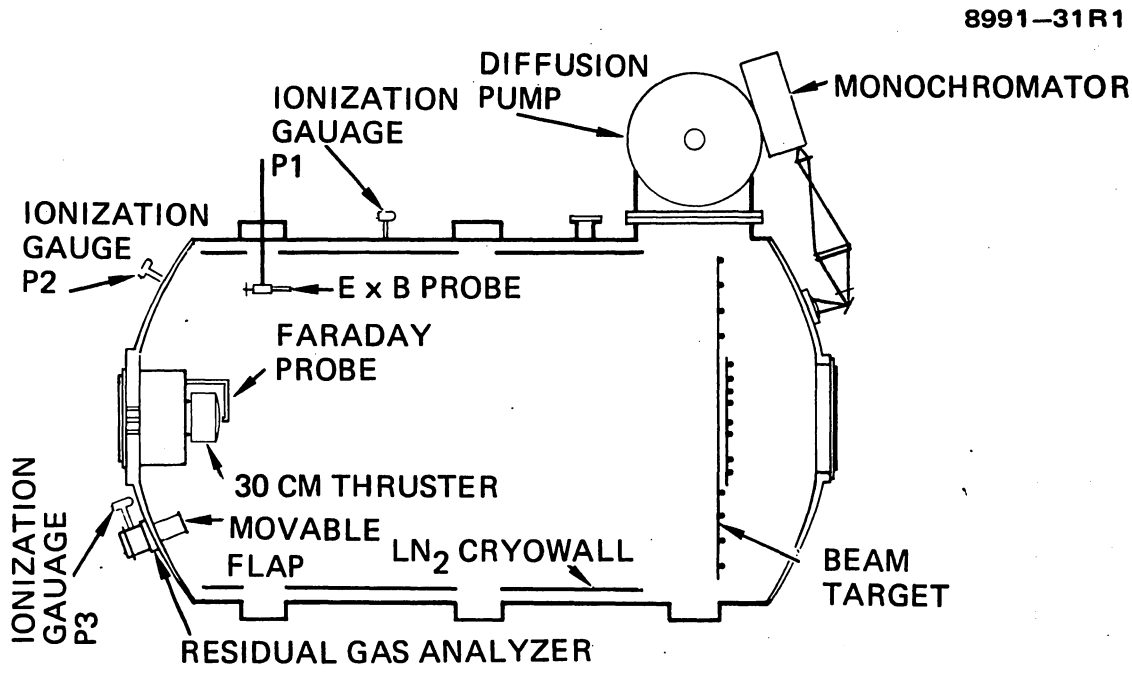

Figure 2-4. Top view of vacuum chamber and test equipment (ExB probe shown as side view for clarity).

of the thruster, residual gas analyzer, monochromator, and ExB probe. The gas analyzer is located at the thruster end of the vacuum chamber so that it is exposed to essentially the same particle flux as the thruster. The instrument is housed within a stainless-steel cylinder equipped with a movable flap at the entrance end. This arrangement serves to shield the analyzer from back-sputtered material when not in use and to isolate the analyzer within a small volume for calibration purposes.

The analyzer collector current is amplified by an electron multiplier; the amplified current is measured using an electrometer. The output of the electrometer is used as input to an x-y plotter when the analyzer is used in the scanning mode and is displayed on a digital panel meter in the partial-pressure mode. In the latter case, the digital output is directly proportional to the partial pressure of the gas corresponding to the mass peak selected. A typical recording of the mass spectra measured in the 0 to 50 amu range is presented in Figure 2-5, which shows the major consituents to be air, water vapor, and a heavy hydrocarbon. The resolution of the gas analyzer calculated from the peak at mass number 28 is approximately $m/\Delta m = 100$.

Table 2-1. Spectral Lines Selected for Study of Screen-Grid Erosion Rate

Excited Species	Wavelength,[a] Å	Relative Intensity[b]
Mo I	3798.25	50
Hg I	3801.66	10[c]
Hg II	3806.38	10
Mo I	3864.11	50
Hg II	4398.62	10
Hg III	4797.01	50

[a] Taken from MIT wavelength tables (Ref. 2-5).

[b] Taken from Kayser and Ritschl (Ref. 2-6).

[c] Taken from Figure 2-3.

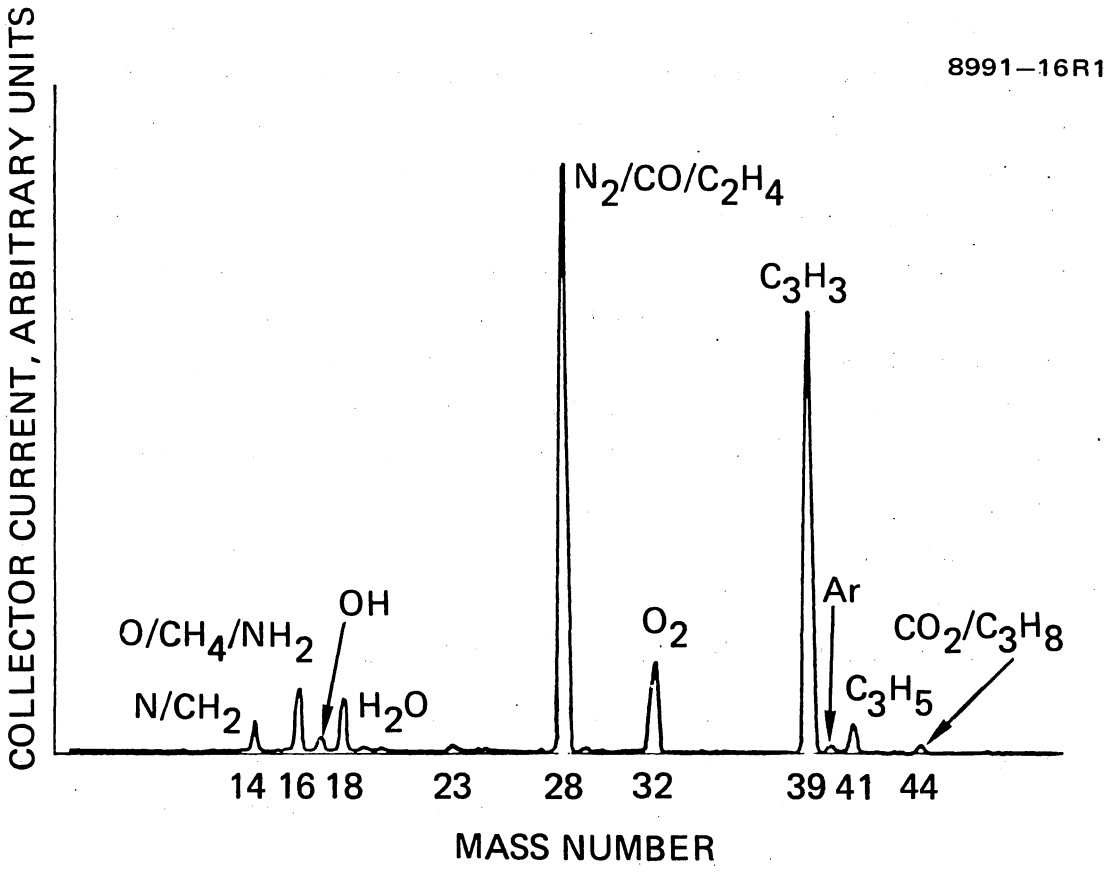

Figure 2-5. Typical mass spectra recorded in the Hughes 9-ft vacuum test chamber.

Partial-pressure measurements were performed by operating the gas analyzer in the manual mode and selecting one of the peaks in the 0 to 50 amu range corresponding to the test gas under study. The pressure was calculated by multiplying the analyzer output by the sensitivity factor corresponding to this gas. The sensitivity of the gas analyzer to each test gas investigated was determined by performing an in-situ calibration of the instrument prior to each test. The calibration was accomplished by isolating the gas analyzer in the small volume of the stainless-steel cylinder and increasing the pressure in this region by admitting small quantities of the test gas. In this manner, the gas analyzer could be calibrated over a pressure range as high as 10^{-3} Pa (10^{-5} Torr) while maintaining the vacuum-test-chamber pressure as low as 10^{-5} Pa (10^{-7} Torr). The residual-gas-analyzer calibration procedure and sensitivity calculation are described in detail in Appendix A.

3. Residual-Gas Injection and Tank-Pressure Control

The effects of various contaminant gases on the erosion rates of critical chamber components such as the baffle and screen grid were investigated by introducing these gases into the vacuum test chamber at a rate sufficient to raise the tank pressure to the desired value. Figure 2-6 is a schematic of the gas-flow system used for admitting and controlling the flow of gas into the vacuum test facility. Valves A and B permit the gas to flow directly into the vacuum test chamber or, for calibration purposes, into the residual-gas-analyzer enclosure. Precise control of the gas flow rate is accomplished using a Veeco PV-10 piezoelectric leak valve. Valve C permits the precision leak valve to be bypassed for rapid evacuation of the entire flow-control system into the vacuum facility or, by using an auxiliary pump and valve D, into the atmosphere.

The tank pressure level was maintained constant by controlling the flow through the piezoelectric leak valve in proportion to the output of an ionization gauge for total-pressure control or to the

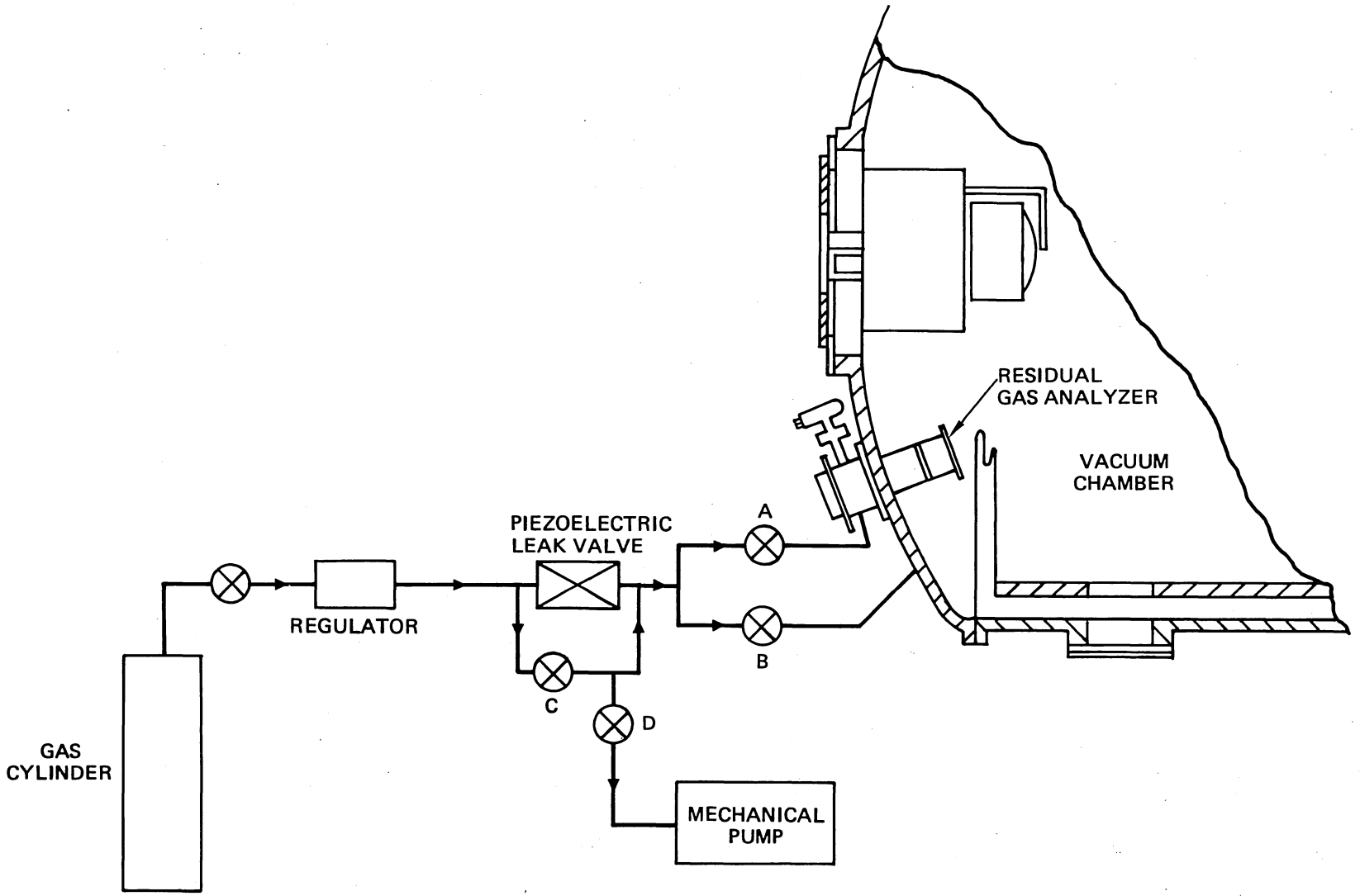

Figure 2-6. Schematic of gas-flow system used for admitting contaminant gases into the vacuum test chamber.

output of the residual gas analyzer for partial-pressure control. Figure 2-7 is a block diagram of a Hughes-built proportional-flow-control system furnished to this contract for use in the residual-gas studies. The controller supplies up to 100 V to the fast-response piezoelectric leak valve in proportion to the 0 to 2 V output of the ionization-gauge controller or the 0 to 5 V output of the residual-gas-analyzer electrometer. This system performed extremely well and enabled precise tank pressure control to be maintained over extended periods.

4. Total Pressure

Total-pressure measurements were made using Bayard-Alpert type ionization gauges that employ thoria-coated iridium filaments and Pyrex enclosures. The ionization gauge, controller, and interconnecting cables were calibrated as a unit in the Hughes Primary Standards Laboratory. The calibration is based on a set of interim standards maintained by the Primary Standards Laboratory, since the National Bureau of Standards does not provide a calibration service for the vacuum range below 1 Pa (10^{-2} Torr). The long-term drift of the ionization gauge/controller assemblies is approximately ±25% based on the Primary Standards Laboratory history of calibration of these instruments using dry contaminant-free nitrogen gas.

The relationship between indicated and true pressure was found to be linear over each decade of the pressure range 10^{-6} Pa $\leq p \leq$ 10^{-2} Pa (10^{-8} Torr $\leq p \leq 10^{-4}$ Torr) so that the true pressure P_{true} is given by the expression

$$P_{true} = afP_{indicated} + b \quad , \tag{2.1}$$

where a and b are the calibration constants, $P_{indicated}$ is the pressure indicated by the controller, and f is the gauge factor of the test gas. The gauge factors are summarized in Table 2-2 for the gases investigated during this study.

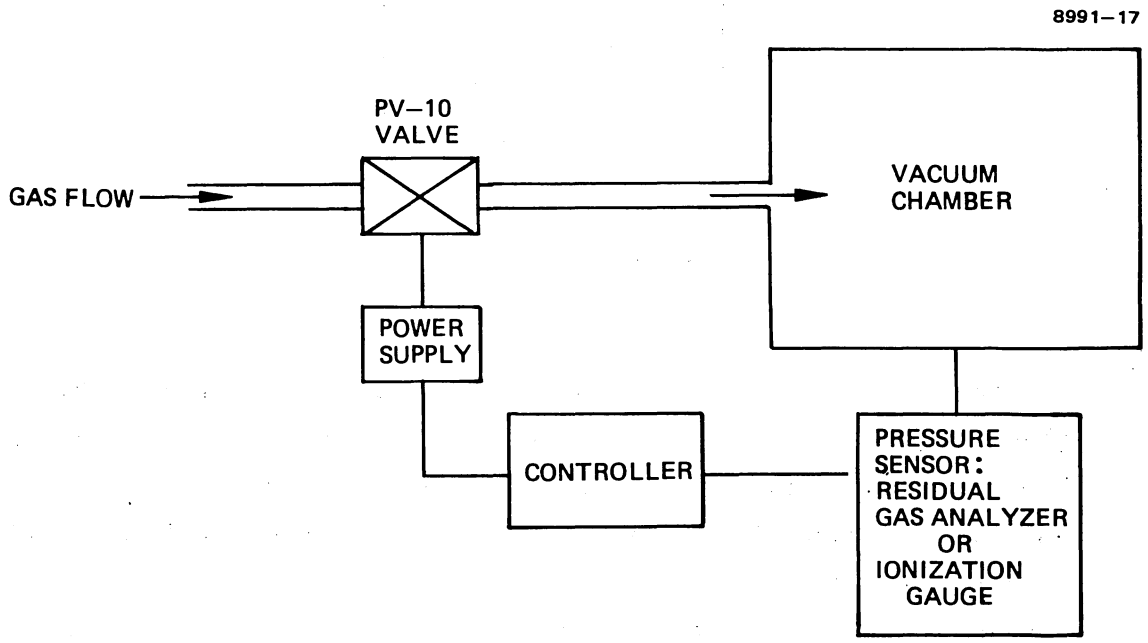

Figure 2-7. Block diagram of proportional-flow-control system used to maintain constant-pressure conditions in the vacuum test chamber.

Table 2-2. Ionization Gauge Factors
(Taken from Ref. 2-7)

Gas	Gauge Factor
Air	1.0
Ar	0.76
CH_4	0.64
C_2N_2	0.36
CO_2	0.66
H_2O	1.0
N_2	0.90
O_2	1.1

6758

Figure 2-4 shows the location of the ionization gauges on the Hughes 9-ft vacuum test chamber. Gauge P2 is located upstream from and slightly above the thruster. Because of its location, the pressure sensed by this gauge is representative of the pressure environment of the thruster. Gauge P3, located within the residual-gas-analyzer enclosure, is used when calibrating this instrument. The remaining gauge, P1, is located behind the chamber cryowall and has no direct line of sight to the interior chamber walls. The pressure indicated by each gauge is approximately the same for beam-off conditions. With the beam on, however, gauge P1 is shielded from the particle flux caused by beam ions striking the cryowall and beam collector and indicates an order-of-magnitude-lower pressure than either gauges P2 or P3. The nearly steady-state pressures indicated by the end and side gauge after 10 to 12 hours of thruster operation at full-thrust beam conditions are nominally 1×10^{-4} Pa (9×10^{-7} Torr) and 1×10^{-5} Pa (9×10^{-8} Torr), respectively.

5. Thin-Film Erosion Monitors

Short-term erosion-rate tests were conducted using thin-film monitors that were prepared in the Sputtering Processes Laboratory at Hughes. These monitors consist of alternating layers of color-contrasting materials (such as tantalum and copper, or molybdenum and copper) that were sputter deposited onto a tantalum or stainless-steel substrate. Layer thickness was carefully controlled during the application process by holding the sputtering-ion-beam voltage and current constant and by precisely timing the deposition. A small piece of polished material (sputter-deposited during preparation of the multilayer monitor material) was used for calibrating layer thickness using a surface profilometer. Layer thickness was calibrated by measurements on the coated, polished sample as follows. First, a pattern of 25-μm lines and spaces was established on the sample surface using optical exposure of photo-resist through a suitable mask. The multilayer material was then ion-beam machined away as shown in Figure 2-8 to make the layer interfaces readily identifiable. After this step, the photoresist mask was removed chemically, and the original polished surface provided the necessary bench mark for Dektak* measurements of the layer thickness.

The monitors had 8 tantalum or molybdenum layers and 7 copper layers; the thickness of the first layer (either tantalum or molybdenum) applied to the substrate was double that of the others. Because copper erodes about 20 to 40 times faster than molybdenum and tantalum, the copper layers were factored into the analysis as only a portion of a layer. Therefore, the total equivalent thickness of a 15-layer (8 tantalum or molybdenum plus 7 copper layers) monitor having 60-nm-thick layers was approximately 560 nm of molybdenum or 550 nm of tantalum.

a. Test Procedure

The baffle and screen grid were the critical chamber components selected for the erosion-rate measurements performed during this

*Dektak Surface Profilometer, Sloan Instrument, Inc., Santa Barbara, CA.

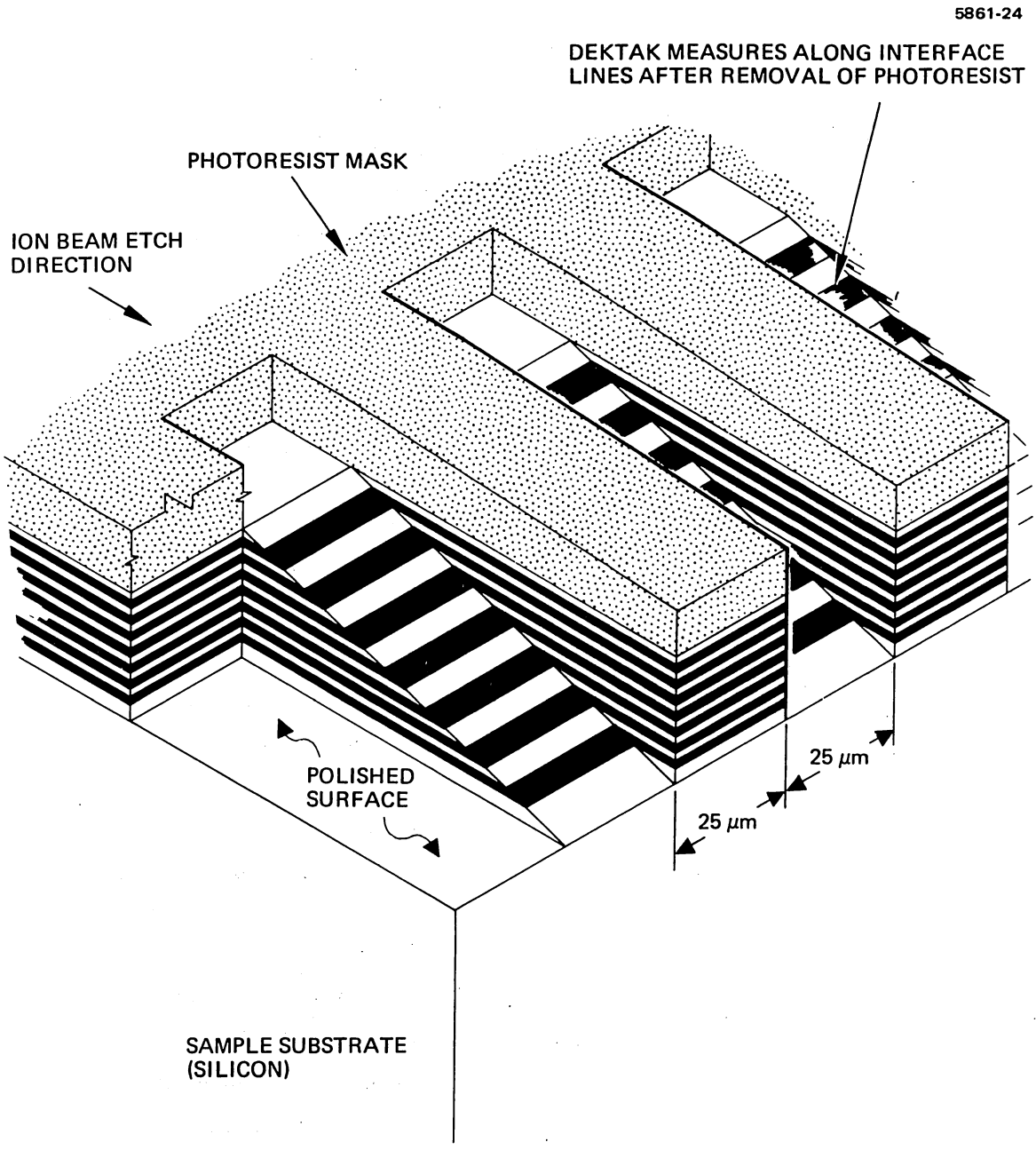

Figure 2-8. Illustration of the ion-machining technique used to determine the layer thickness of thin-film erosion monitors.

investigation. Small pieces of the appropriate monitor material were spot-welded to these surfaces prior to the test. The screen-grid monitors were perforated, with the dimensions selected to account for the screen-electrode compensation. A small area of the baffle erosion monitors was masked-off during the test to aid in determining the number of layers eroded during the exposure.

Several precautions were taken during the erosion-rate tests to ensure the validity of the test results. For example, discharge-chamber operating conditions were carefully monitored and controlled by the use of vaporizer control loops and stable power supplies. The vacuum conditions of the test chamber are crucial in obtaining valid erosion-rate measurements, since the presence of certain residual gases is known to substantially reduce the surface sputtering yield. The procedures followed during the erosion-rate tests included:

- Venting the vacuum test chamber with gaseous nitrogen during thruster removal/installation operations.
- Pumping sufficiently to achieve chamber pressures in the low 10^{-4} Pa (10^{-6} Torr) range using the oil-diffusion pump and LN_2 baffle arrangement in the Hughes 9-ft vacuum test chamber.
- Cryopumping prior to thruster startup to achieve chamber pressures in the range 10^{-6} Pa $\leq p \leq 10^{-5}$ Pa (10^{-8} Torr $\leq p \leq 10^{-7}$ Torr).
- Recording periodically total-pressure conditions and relative-abundance measurements using ionization gauges, and the scan mode of the quadrupole residual gas analyzer.
- Maintaining the partial pressure constant using the proportional-flow-control system described earlier during those tests where contaminant gases were admitted into the vacuum chamber.
- Recording periodically the molybdenum line intensities to verify the constancy of the screen-grid erosion rate during the 10 to 12 hr required for erosion-rate measurements.

- Scaling the thruster operating time to remove several, but not all, of the erosion-monitor layers to minimize the uncertainty in the measured erosion rates.

b. Interpretation of Results

After completing the test, the erosion monitors were removed from the baffle and screen grid for analysis. Each monitor was diagnostically etched using an argon ion beam to expose the reamining layers and facilitate identifying the layer interfaces. During this investigation, we developed a new technique to enhance the color contrast between the copper and molybdenum or tantalum and hence to facilitate identifying and counting the remaining layers. The color-enhancement technique involves accelerated oxidation of the erosion-monitor surface after performing the diagnostic etch. This was accomplished by heating the erosion monitors for ∿45 min in an air furnace maintained at a temperature of ∿200°C. Oxidation of the exposed copper layers darkens them considerably, and this color enhancement makes it much easier to accurately count the remaining layers. Figure 2-9 is a color photograph that illustrates the dramatic improvement in the visibility of the copper layers of a screen-grid erosion monitor after applying the color-enhancement technique. The copper layers (a total of seven) appeared as faint streaks prior to heating but as easily identifiable dark red or black lines after the heat treatment. The light-colored lines in the photograph are molybdenum layers, and the double-thickness molybdenum layer is clearly visible at the top of the photo. The apparent variation in the thickness of the remaining layers is caused by the nonuniform slope of the thickness profile produced by the diagnostic etch.

After the number of copper layers remaining was determined, the erosion rate W was calculated using the expression

$$W = [(N - N' + 0.5)\ \delta_{Mo,Ta} + (N - N')\ \delta_{Cu}/\gamma]/\tau \quad , \qquad (2.2)$$

where N and N' are the initial and final numbers of copper layers, respectively; δ is the layer thickness; τ is the test time; and γ accounts for

8991–33

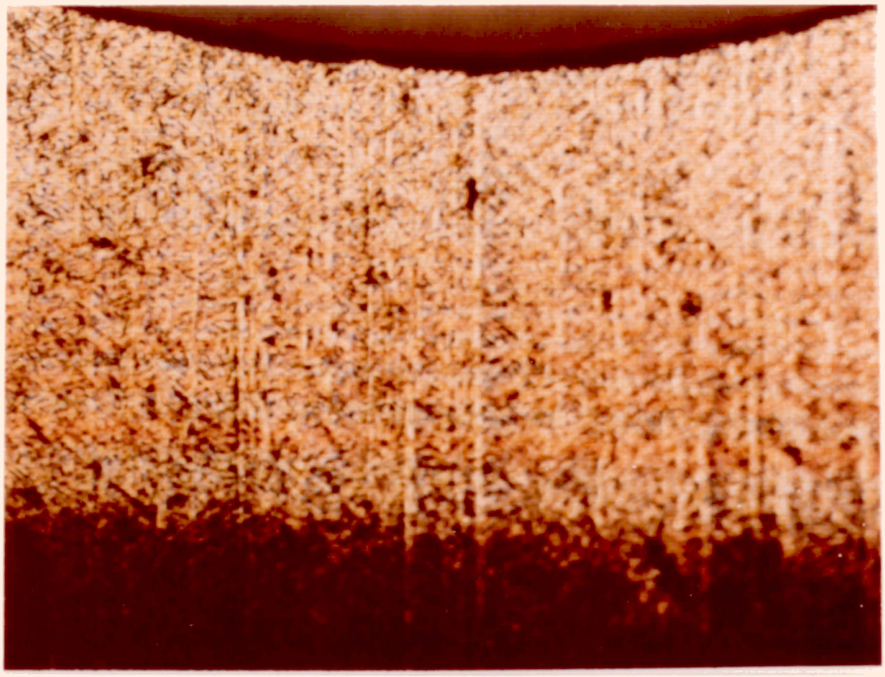

A. BEFORE HEATING

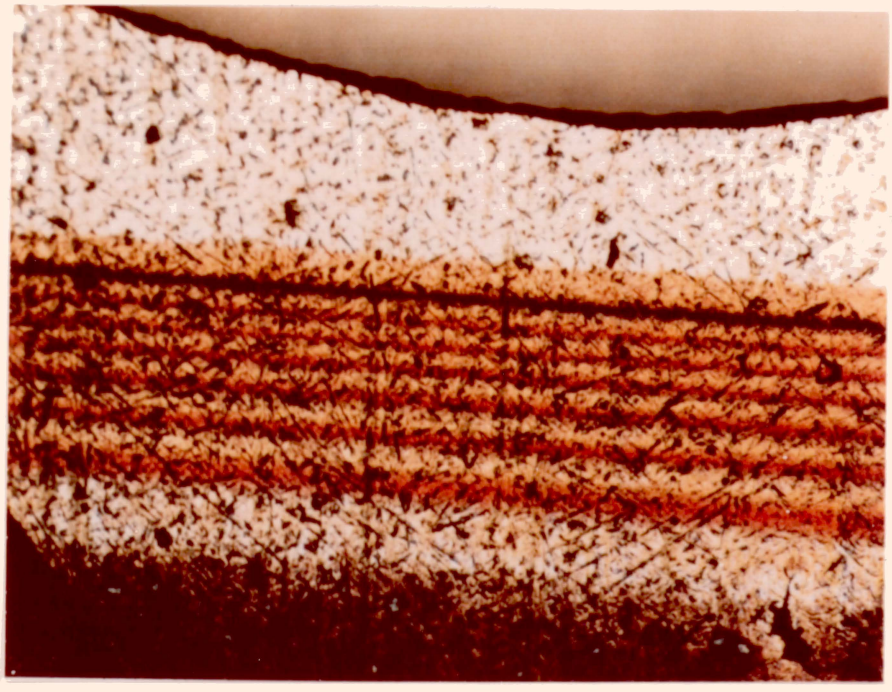

B. AFTER HEATING TO 200°C FOR 45 MINUTES

Figure 2-9.
Photographs of the web region of a screen-grid erosion monitor showing the dramatic improvement in color contrast achieved by heating the sample.

Page intentionally left blank

the increased erosion rate of copper (γ = 20 for molybdenum monitors and γ = 40 for tantalum monitors). The first term in the numerator of Eq. 2.2 represents the thickness of eroded tantalum or molybdenum, with the constant 0.5 introduced to account for the unknown fraction of the tantalum or molybdenum layer remaining above the highest visible copper layer. The second term in Eq. 2.2 accounts for the copper layers eroded; the factor $1/\gamma$ converts copper layer thickness to equivalent tantalum or molybdenum layer thickness. For equal layer thickness, Eq. 2.2 reduces to

$$W = \left[(N - N') \left(\frac{\gamma + 1}{\gamma}\right) + 1/2\right] \delta/\tau \ . \qquad (2.3)$$

Adopting the above definition of the unknown remaining layer thickness, the uncertatinty in the number of eroded layers is 0.5. This results in an erosion-rate uncertainty U given by

$$U = \pm\frac{\delta}{2\tau} \ . \qquad (2.4)$$

6. Screen-Grid Ion Flux

The ion-optics mounting ring of the SN 301 thruster is electrically isolated from the thruster body, permitting electrical bias of the screen electrode. In this way, the ion arrival rate at the screen grid could be measured by biasing this electrode up to 30 V negative of the cathode. The ion-current/bias-voltage relationship was recorded on an x-y plotter through the use of isolation amplifiers, and the ion-saturation current was found by extrapolating this curve to zero (cathode) potential.

Measurements of the local ion flux to the screen electrode were attempted using the probes shown in Figure 2-10. These probes were fabricated from the 0.05-mm stainless-steel substrate material used in fabricating the thin-film erosion monitors described above. A ceramic-coated lead wire was spot-welded to the collector (plasma) side of the probe, and the screen-grid side was coated with a sputter-deposited

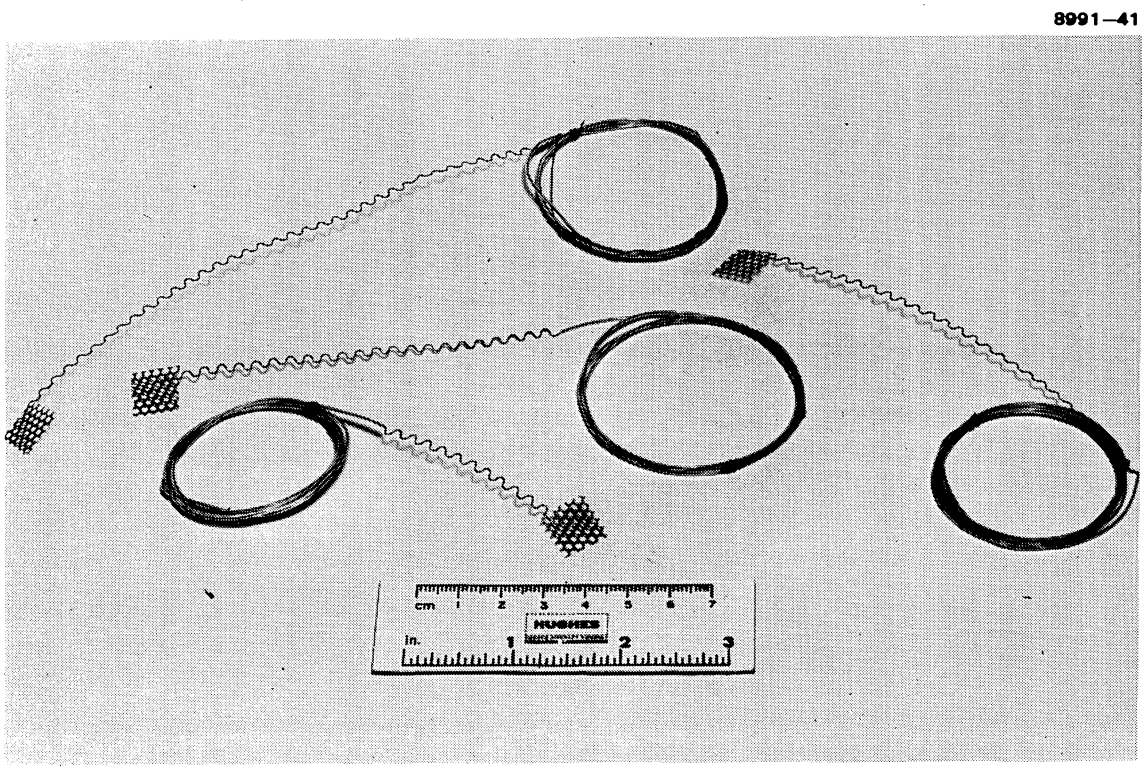

Figure 2-10. Photograph of screen-grid ion-flux probes.

layer of SiO_2, forming a dielectric coating on this surface. The probes and lead wire were cemented in place using a high-temperature, dielectric adhesive. Short-term use of these devices in an operating thruster was successful, but, within one or two hours, the probes invariably shorted to the screen grid due to contamination of the exposed adhesive interface between the probe and screen grid. A laborious attempt was made to undercut the adhesive to provide shadow shielding of this interface, and although this procedure allowed a shorted probe to be open-circuited, the undercut would eventually become coated with sputtered conducting material, causing the probes to short to the screen electrode.

7. Plasma Potential

The local plasma potential was the plasma property of primary interest in the investigation of discharge-chamber and screen-grid erosion, since this parameter determines the energy of the ions striking the chamber surfaces. Plasma-potential measurements were obtained at various locations within the discharge chamber using the automated Langmuir-probe system described in Ref. 2-3.

8. Beam Diagnostics

The radial distribution of singly and doubly charged ions is necessary to provide an understanding of localized chamber-erosion phenomena. The total-current-density profile determines the radial location of maximum chamber wear rate, and the approximate shape of this profile was obtained from beam-current-density measurements. These data were obtained using a Faraday-cup probe which could be swept through the ion beam at a distance $\sim$6 mm downstream from the center of the accel electrode. The distributions of the singly and doubly charged ions were obtained by use of the articulating ExB probe[2-8] shown in Figure 2-4.

C. EXPERIMENTAL RESULTS

The investigation of discharge-chamber and screen-grid erosion required numerous experiments to provide a data base on which a model of wearout lifetime could be formulated. The studies involved an investigation of the thruster design, operational, and material characteristics as well as the facility-related parameters that were known or thought to affect the sputter rates of critical discharge-chamber components. The study began with preliminary experiments that were designed to confirm the validity of the spectroscopic technique of assessing relative erosion rates and progressed through a series of tests that investigated the thruster and environmental parameters that were considered fundamental to understanding the chamber-erosion phenomena. The experimental results obtained during these studies are presented in Sections 2.C.1 through 2.C.9.

1. Preliminary Optical-Spectroscopy Measurements

A preliminary investigation of the effects of thruster operating conditions on the intensity I of light measured at various wavelengths corresponding to excitation of molybdenum, mercury, and copper atoms was conducted at the outset of this study. The purpose of these preliminary experiments was to establish the validity and sensitivity of the spectroscopic method of assessing relative changes in the screen-grid erosion rate. Since two sources of molybdenum — the screen and the accel electrodes — could contribute to the MoI line-intensity measurement, it was necessary to establish the source of the sputtered molybdenum producing the observed line intensity. Erosion of the accel electrode due to the impingement of either charge exchange or primary beam ions can be expected to vary with accelerator voltage, since this parameter determines the energy of the ions striking the electrode and affects the focusing of the beamlets formed by the accelerator system. Therefore, any change in the molybdenum line intensity due to variations

in the accelerator voltage would indicate a change in the erosion rate of this electrode. Conversely, the absence of any change in line intensity would confirm the screen electrode as the primary source of sputtered molybdenum within the chamber. Figure 2-11 presents the measured ratio of the intensities of the MoI and HgI spectral lines at wavelengths of λ = 3798.3 Å and λ = 3801.7 Å, respectively, as a function of accelerator voltage. The constancy of the intensity ratio over a wide voltage range confirmed the screen electrode as the primary source of the observed molybdenum line intensity.

Having established the screen electrode as the primary source of sputtered molybdenum, it was then possible to demonstrate the sensitivity of the measured molybdenum line intensity to variations in parameters known to affect surface erosion rates. The parameters selected were the discharge voltage, beam current, and surface area of the sputtering source. Our results are discussed in Sections 2.C.1.a through 2.C.1.d.

a. Discharge-Voltage Sensitivity

Figure 2-12 presents the measured variation of the normalized molybdenum-line-intensity ratios with discharge voltage. These results verified the dependence of the molybdenum-line-intensity measurements on a thruster operating parameter that was known to affect the wear rate of the screen electrode; they also demonstrated the sensitivity of the spectroscopic method. The presence of the same trend in all the normalized curves of Figure 2-12 indicates that both the HgI and HgII spectral lines are suitable for normalization of the MoI line intensity. Use of the HgI line intensity as a normalizing quantity results in a somewhat greater sensitivity to discharge-voltage variations, since, for constant beam current, the neutral density decreases with increasing discharge voltage. The nonlinearity in the intensity-voltage variation of Figure 2-12 reflects the nonlinear dependence of both the molybdenum sputtering yield and the doubly charged ion concentration on the discharge voltage.

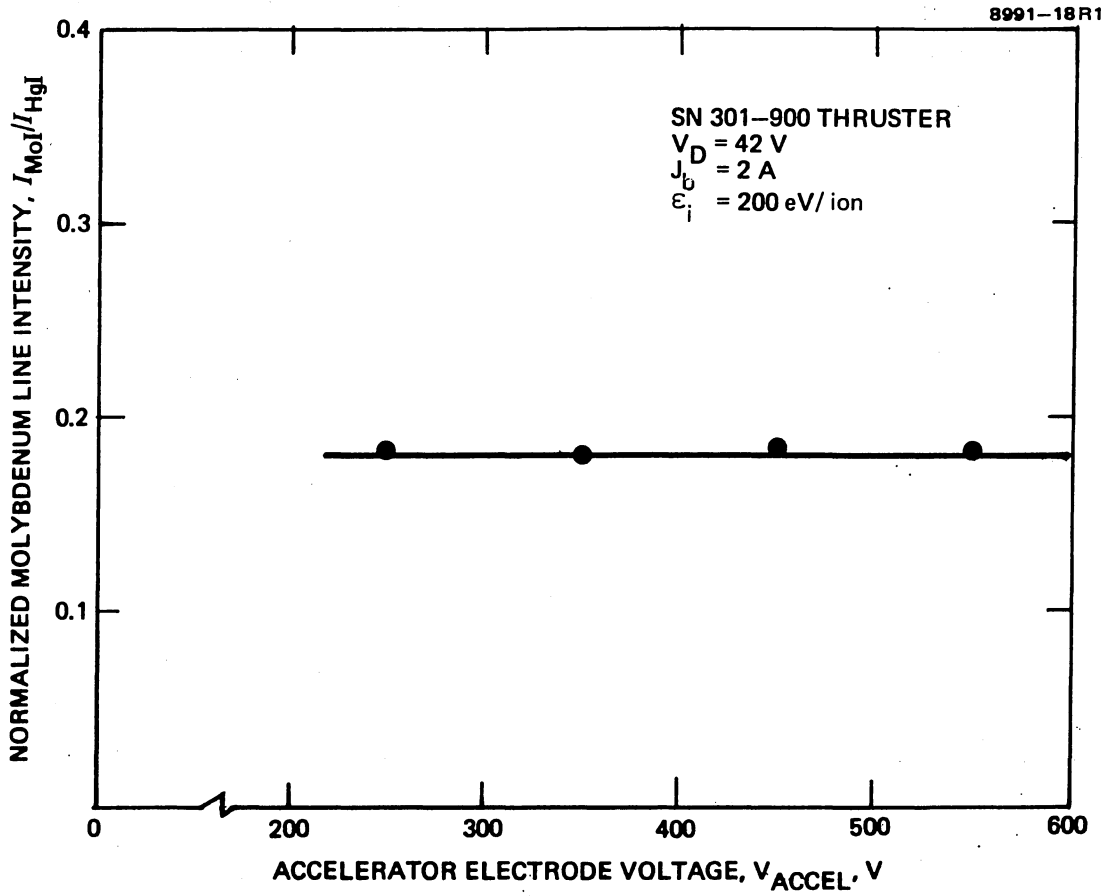

Figure 2-11. Variation of normalized molybdenum line intensity with accelerator voltage. (λ_{MoI} = 3798.3 Å, λ_{HgI} = 3801.7 Å).

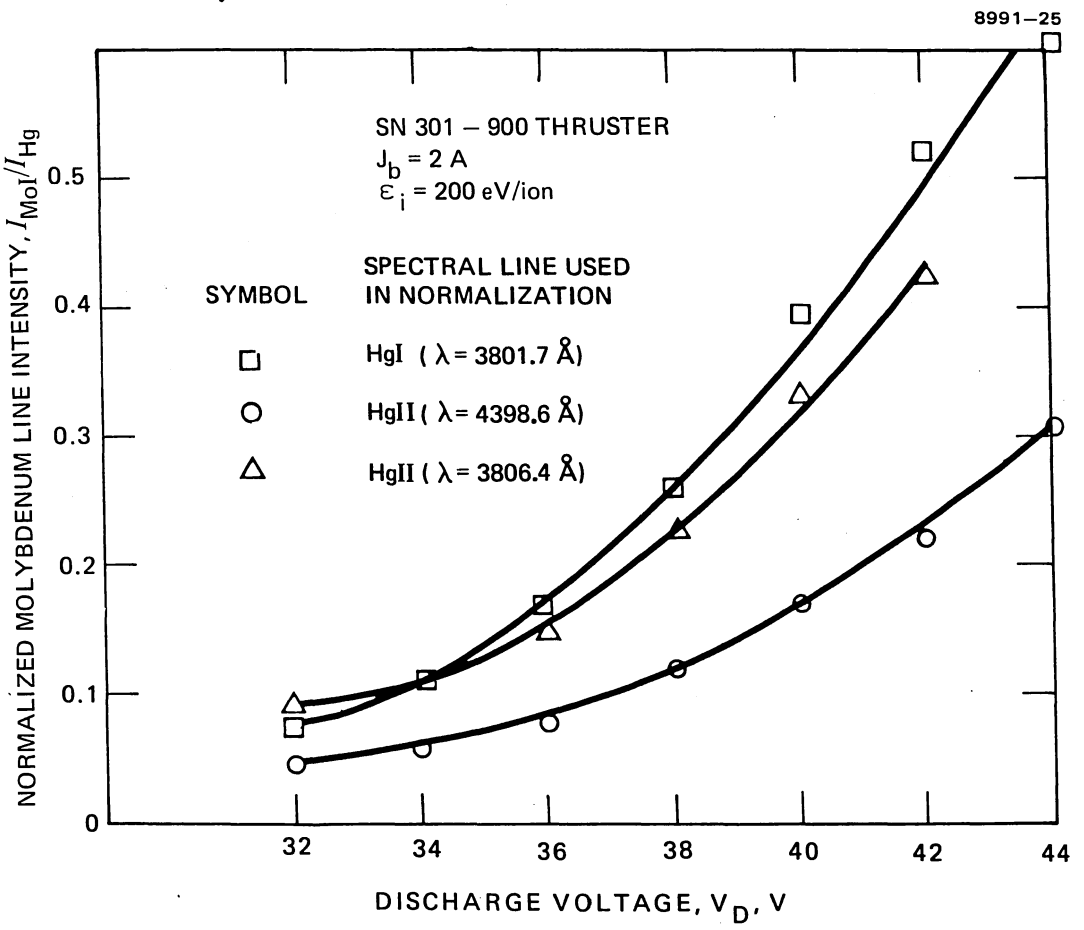

Figure 2-12. Variation of molybdenum line intensity with discharge voltage. (MoI line measured at a wavelength of λ = 3798.3 Å).

b. Beam-Current Sensitivity

The measured variation of the normalized molybdenum-line-intensity ratios with beam current is presented in Figure 2-13. The sensitivity of the normalized line intensities to beam current is clearly evident, with the relationship either linear or nonlinear depending on whether an HgII or HgI line was used in the normalization. These trends can be explained on the basis of the variations in the ion and neutral densities with beam current. The screen-grid erosion rate is known to vary nonlinearly with beam current. This strong dependence is due to the combined effects of the linear increase in plasma density and the resultant linear increase in doubly charged ion concentration with beam current.

The neutral density in the discharge chamber of the 30-cm thruster remains nearly constant as the beam current is varied, which results in a nearly constant value of the line intensity corresponding to excitation of neutral mercury atoms. Therefore, normalization of the molybdenum line intensity by the intensity of the atomic mercury line should result in a quantity that is proportional to erosion rate. The normalized quantity should vary nonlinearly with beam current; this trend is evident in Figure 2-13. The mercury ion density within the discharge chamber varies nearly linearly with beam current, and normalization of the molybdenum line intensity by the line intensity corresponding to excitation of mercury ions results in a normalized parameter of the form

$$\frac{I_{MoI}}{I_{HgII}} \propto \frac{W}{J_b} \quad , \tag{2.5}$$

where W is the screen-grid erosion rate, and J_b is the beam current. Similarly, the constant-neutral-loss-rate argument resulted in the proportionality,

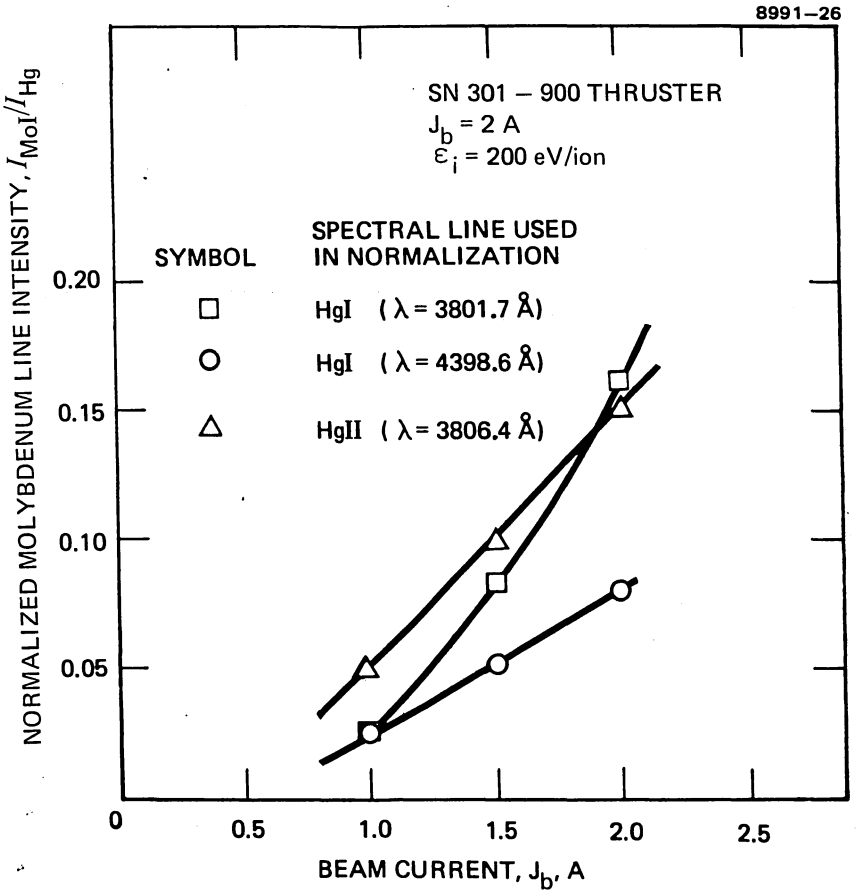

Figure 2-13. Variation of molybdenum line intensity with beam current. (MoI line measured at a wavelength of λ = 3798.3 Å).

$$\frac{I_{MoI}}{I_{HgI}} \propto W \quad . \tag{2.6}$$

Combining these expressons yields the following proportionality between the normalized quantities

$$\frac{I_{MoI}}{I_{HgII}} \propto \frac{1}{J_b}\left(\frac{I_{MoI}}{I_{HgI}}\right) . \tag{2.7}$$

The validity of this expression can be demonstrated by dividing the nonlinear data of Figure 2-13 (corresponding to normalization by the HgI line) by the beam current and observing whether the derived quantity is a linear function. The results of these calculations are presented in Figure 2-14, which shows the linearization that results from multiplying the normalized intensity I_{MoI}/I_{HgI} by the quantity $1/J_b$.

c. Surface-Area Effects

A linear variation of line intensity with the surface area of the sputtering source is expected for conditions of constant ion density and plasma potential. This aspect of surface sputtering was investigated in an operating thruster using a movable copper rod to vary the surface area of the primary source of the CuI line emitted at a wavelength of λ = 3248 Å. Figure 2-15 presents the measured variation of the copper line intensity with rod position, or surface area. The relatively small change in intensity in the region defined by $0 \leq \ell \leq 5$ cm is due to the low plasma density in the region upstream from the critical magnetic field line. In the region defined by $\ell \geq 5$ cm, the line intensity increases rapidly, with the nonlinearity produced by the gradient in plasma density occurring downstream from the critical field line.

The results given in Figure 2-15 confirmed the sensitivity of the measured line intensity to the surface area of the source of sputtered material and indicated that even small sources of sputtered material

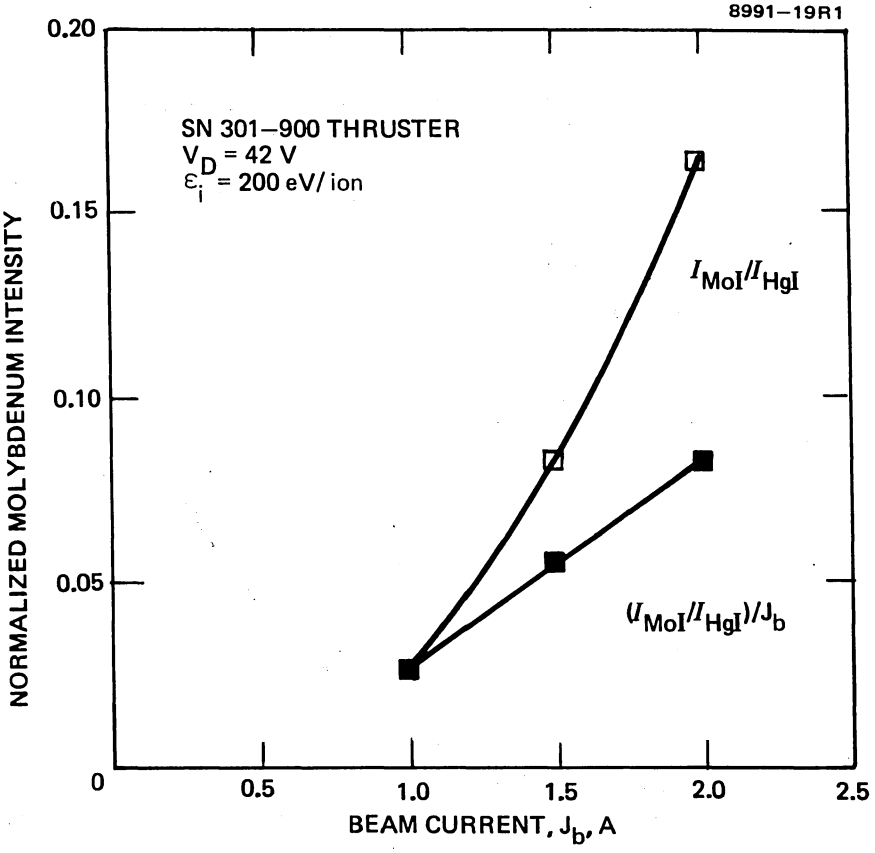

Figure 2-14. Linearization achieved by multiplying the normalized molybdenum line intensity by the reciprocal of beam current.

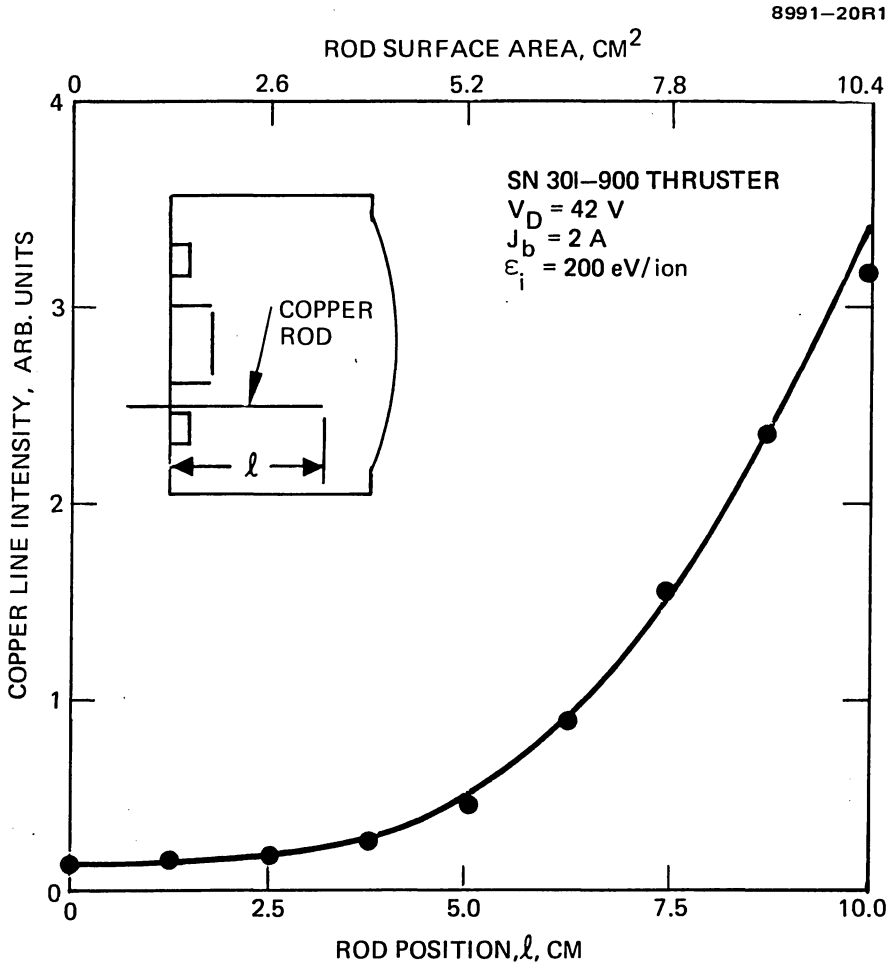

Figure 2-15. Variation in copper line intensity (λ = 3248 Å) with surface area.

located in regions of the chamber where the plasma is relatively dense are detectable using the optical system described above. These results suggested an alternate approach for obtaining quantitative erosion-rate data through the combined use of thin-film erosion monitors and optical spectroscopy. The proposed technique is based on (1) the observation that the line intensity produced by the sputtering of small sources of copper is detectable and (2) the assumption that small thin-film erosion monitors erode uniformly across their exposed surface. If these conditions are satisfied, the intensity of the copper line corresponding to this source should exhibit a periodic variation, with the period equal to the time required to erode through one copper layer and one layer of the intervening material (which is chosen to be the same as the material of the surface under study). If successful, this technique would provide quantitative erosion-rate data in essentially real time, and thruster setup time could be minimized through the use of many-layered thin-film monitors. Because of its potential usefulness, a limited study of this technique was considered worthwhile. Although preliminary results were promising, the merits of such a technique could not be demonstrated conclusively in a reasonable length of time and further study was not considered justified under the present program.

d. Correlation of Spectroscopic Measurements with Beam-Diagnostic Data

Spatial resolution of the molybdenum- and mercury-line-intensity data was demonstrated using the mask arrangement described in Section 2.B.1. That the observed line intensities were representative of local densities was verified by showing good correlation between the local line-intensity data and data from more direct measurements (ExB probe) of the same properties. This was accomplished by measuring the intensities of the HgII and HgIII lines (corresponding to wavelengths of λ = 3806.4 and 4797.0 Å, respectively) using three different mask geometries that permitted light from select regions of the chamber to reach the entrance slit of the monochromator. These measurements were performed while varying the discharge voltage over the range

$30 \leq V_D \leq 40$ V. At each discharge-voltage level, the relative abundance of the doubly and singly charged beam ions was measured using the ExB probe shown in Figure 2.4. Figure 2-16 presents the correlation of the line-intensity measurements with the probe results for the chamber centerline, mid-radius, and entire chamber area. A linear least-squares regression of the data in Figure 2-16 results in correlation coefficients in the range $0.97 \leq r^2 \leq 0.99$. The successful correlation of these results demonstrates the ability of the spectroscopic technique to provide both average and local diagnostic information. The extremely linear correlation of the results of Figure 2-16 illustrates the utility of the fast spectroscopic method in assessing relative changes in critical thruster performance parameters such as the ratio of doubly to singly charged ion densities.

2. Erosion-Rate Measurements

Measurements of the screen-grid and baffle erosion rates were performed using the thin-film technique described in Section 2.B.5. The screen-grid centerline is considered the most critical chamber surface from a lifetime standpoint, and primary emphasis was placed on assessing the erosion rates of this region under a variety of test conditions. The baffle, on the other hand, is not considered a life-limiting component since it is amenable to cladding with a low-sputter-yield material such as tantalum. However, because of its central location and resultant exposure to the dense discharge plasma, the baffle was also selected for erosion-rate measurements. Test times were scaled (based on calculated erosion rates) to result in the removal of 12 to 13 layers of the erosion monitors located at the center of the screen grid. Because of the nonuniform plasma-density distribution of the 30-cm thruster, this test-time criterion results in the removal of about one-half this many layers at the mid-radius location. At the full-thrust

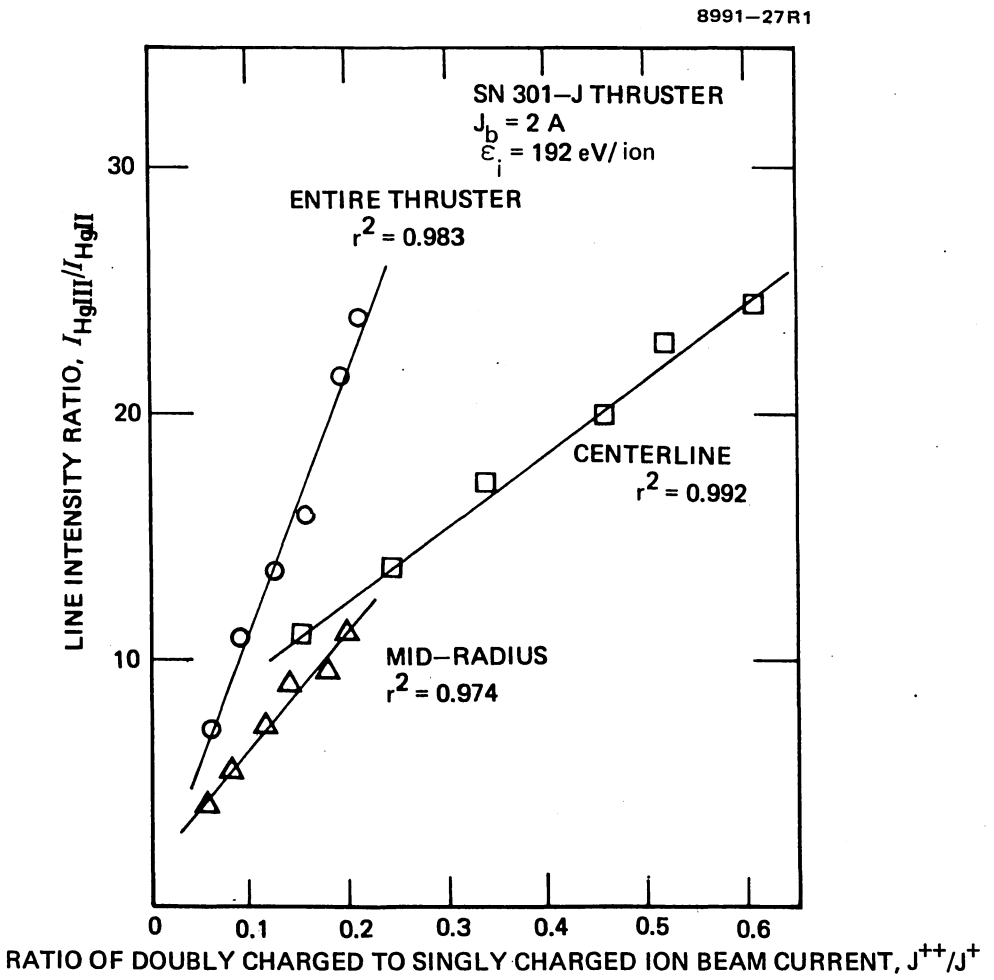

Figure 2-16. Correlation of spectroscopic measurements of discharge-plasma properties with ion-beam-probe results. (To obtain these data, the discharge voltage was varied over the range 30 V ≤ V_D ≤ 40 V in 2-V increments.)

beam and discharge conditions of the J-series thruster, a test time of approximately 12 hr is required to remove the upper 12 to 13 layers of the screen-centerline monitor. Because of the large number of test conditions investigated, 12 hr was considered the practical upper limit to the length of a continuous test. Longer duration tests could have been broken into shorter segments, but this approach is undesirable since it introduces an additional uncertainty into the test results due to the effects of both thruster and facility starting transients. Therefore, the lower limits on discharge voltage and beam current that would nearly satisfy the test-time criteria were 29 V and 2 A, respectively. For those studies where nitrogen was added to the vacuum test chamber (Section 2.C.4), the discharge voltage was increased to 36 V to minimize the test-time requirement (and also to enhance the effects of a contaminant gas on erosion rate).

Table 2-3 represents the erosion-rate test results obtained during the parametric study of the effects of discharge voltage, screen-electrode bias, and acclerator-electrode design. A complete dicsussion of these results is presented in Sections 2.C.2.a through 2.C.2.c. However, some general comments on the results of Table 2-3 are warranted before discussing the more detailed aspects of the parameter-variation test results. First, the uncertainty in the measured erosion rates, defined as one-half a layer thickness divided by the test time, is due to the unknown fraction of the remaining molybdenum or tantalum layer that lies above the highest visible copper layer. Based on this definition and the test duration criteria, the uncertainty is proportional to the maximum erosion rate and is, therefore, greater for the shorter tests. Second, the ratios of doubly charged to singly charged ion currents presented in Table 2-3 exhibit the expected increase with discharge voltage, and generally the mid-radius value of this ratio agrees closely with the values obtained by averaging over the beam area. Third, the ratio of the average to the maximum beam current density F is about 0.5 and independent of any of the indicated parameter variations. As a

Table 2-3. Summary of Erosion-Rate Test Results Obtained using Thin-Film Erosion Monitors

No.	V_D, V	V_{Bias}, V	Erosion Rate, nm/hr				U, nm/hr	Test Time, τ, hr	Optics Series	V_b, V	V_{Accel}, V	J_{MB}, A	ε_i, eV/ion	η_u, %	Doubly to Singly Charged Ion Current Ratio, J, %			F
			Screen Grid		Baffle										Avg.	r = 0	r = $R_T/2$	
			r = 0	r = $R_T/2$	Discharge Side	Cathode Side												
1	29	0	10.4	—	2.5	2.5	2.5	12.0	J (SN 828)	1400	-500	1.2	192	82.8	5.4	10.4	5.4	0.53
2	32		21.4	11.3	3.6	3.6	3.6	8.25				1.7		86.8	—	—	—	0.55
3	32		23.5	—	2.5	2.5	2.5	12.0				1.7		88.1	10.3	25.6	9.5	0.55
4	36		54.0	23.4	28.9	15.3	5.0	6.0				2.6		91.0	16.7	40.6	16.8	0.49
5	36		54.4	—	27.6	5.0	5.0	6.0				2.6		91.7	16.3	45.2	14.3	0.50
6	32	-15	92.2	50.1	6.7	6.7	6.7	4.5				1.6		89.5	11.8	29.8	11.0	0.53
7	32	-15	92.6	62.6	8.6	8.6	8.6	3.5				1.6		—	--	—	—	0.51
8	36	0	52.9	24.5	41.9	25.5	5.0	6.0	900 (SN 653)	1100	-300	2.4	200	87.3	17.7	46.4	17.4	0.45
9	36	0	53.0	26.0	—	—	5.0	6.0	900 (SN 653)	1100	-300	2.4	200	87.6	16.5	47.4	16.3	—

Definitions of symbols not previously used:

V_{Bias} = Screen bias

r = Radius

R_T = Thruster radius

V_b = Beam voltage

V_{accel} = Accel voltage

J_{MB} = Magnetic baffle current

ε_i = Discharge loss

η_u = Propellant utilization efficiency (measured)

F = Beam flatness parameter

result, the screen-grid erosion at the center is about twice that at the mid-radius. Fourth, the results of Table 2-3 are generally quite repeatable, and repeated data agree within the uncertainty of the measurements.

a. Discharge-Voltage Effects

The effects of discharge-voltage variations are presented in lines 1 through 5 of Table 2-3. The expected increase in both doubly charged ion density and chamber erosion is evident in these data, which show a five-fold increase in both quantities as a result of increasing the discharge voltage from 29 to 36 V. The baffle erosion rates measured at discharge voltages of 29 and 32 V are equal to the uncertainty in the measurements, indicating that the erosion of this surface is much lower than that of the screen-grid centerline. Baffle erosion, particularly on the discharge side, increases substantially with discharge voltage in the range $32\ V \leq V_D \leq 36\ V$.

b. Ion-Optics Effects

The results of Table 2-3 indicate that chamber wear rates are independent of accelerator open-area fraction unless the discharge operating conditions are varied. From these results, it is apparent that the discharge voltage, doubly charged ion concentration, and plasma-density distribution determine the chamber wear rates.

c. Screen-Electrode Bias Effects

The screen-grid erosion rate increased by a factor of five as a result of biasing the screen grid 15 V negative of cathode potential. The extreme sensitivity of erosion rate to screen bias reflects the nearly exponential increase in sputter yield with ion energy. As expected, there was no effect of screen-electrode bias on the baffle erosion rate.

The strong effect of screen-grid bias on the erosion rate of this electrode suggests that the lifetime of this component could be substantially increased by allowing it to float with respect to the

cathode. Using this arrangement, the screen grid would assume a potential intermediate to that of the cathode and plasma, resulting in a reduction in the energy of the ions striking its surface. This aspect of controlling screen-grid lifetime was not pursued under the present investigation.

d. Comparison of Erosion-Monitor and Long-Term Test Results

The screen-grid erosion rates presented in Table 2-3 for the 900- and J-series thruster configurations (operated at standard discharge conditions) are about twice as high as the corresponding results obtained during long-term testing where surface thickness changes were measurable.[2-2,2-4] The maximum erosion rate of about 22.5 ± 2.5 nm/hr listed in Table 2-3 for the standard J-series thruster operating condition does not compromise the lifetime goal of 15,000 hr (assuming that 90% wearout of the screen electrode near the center is tolerable), but the discrepancy in these measured results is disconcerting. There are several factors that could contribute to the differences in the measurements:

- Effects of facility residual gases
- Errors in determining the layer thickness of the thin-film monitors
- Differences in the densities and sputter yields of bulk and sputter-deposited metals.

Facility pressure effects can be ruled out as the source of the discrepancy since the chamber pressures were comparable in the long- and short-term tests. The thickness of the erosion-monitor layers was checked using a surface profilometer and found to be within 2% of the calibrated value, thus eliminating this factor as the source of the discrepancy. Sputter-deposited thin films are amorphous, whereas the bulk materials have a polycrystalline structure. Because of these surface geometries, the amorphous films tend to erode in a manner that preserves the planar nature of the surface, while the polycrystalline surfaces tend to become faceted as a result of variations in the incidence angle of the ion beam and the variously oriented crystal planes.

Also, the density of sputter-deposited films could be less than that of bulk materials (which may have been rolled and heated). Although these latter effects are probably small, they could increase the erosion rate of sputter-deposited films over that of the bulk material. In a recent Hughes experiment, we compared the sputter rates of bulk and sputter-deposited molybdenum and found that they agreed to within 10%. This test was conducted by first using a 150-eV argon ion beam to sputter the two samples and then measuring the etch depth using a surface profilometer. Although this represents only one datum point, the close agreement suggests that differences in the sputter yields of bulk and sputter-deposited metals such as molybdenum do not explain the consistently higher erosion rates of thin-film monitors.

The fundamental question of whether sputter-deposited layers erode at the same rate as bulk metals remains only partially answered. Until enough data are obtained to demonstrate conclusively that the sputter erosion rates are the same, or a calibration can be established, the results obtained with the thin-film monitors should be interpreted in a relative sense.

3. Correlation of Erosion-Rate and Line-Intensity Measurements

The basis for using molybdenum-line-intensity measurements to infer the erosion rate of the screen grid was discussed in Section 2.B.1. The validity of the spectroscopic technique can be established by demonstrating a correlation between the measured line intensities and the screen-grid erosion rates. Figure 2-17 presents the correlation of normalized molybdenum line intensities and screen-grid erosion rates measured at the centerline and mid-radius locations. The linear relationship indicated in Figure 2-17 demonstrates the utility of using line-intensity measurements as an indication of relative changes in the local erosion rate of the screen grid. The successful correlation of these measurements permits the spectroscopic technique to be used with confidence in applications (such as the contaminant gas study described in Section 2.C.4) where many test conditions must be evaluated.

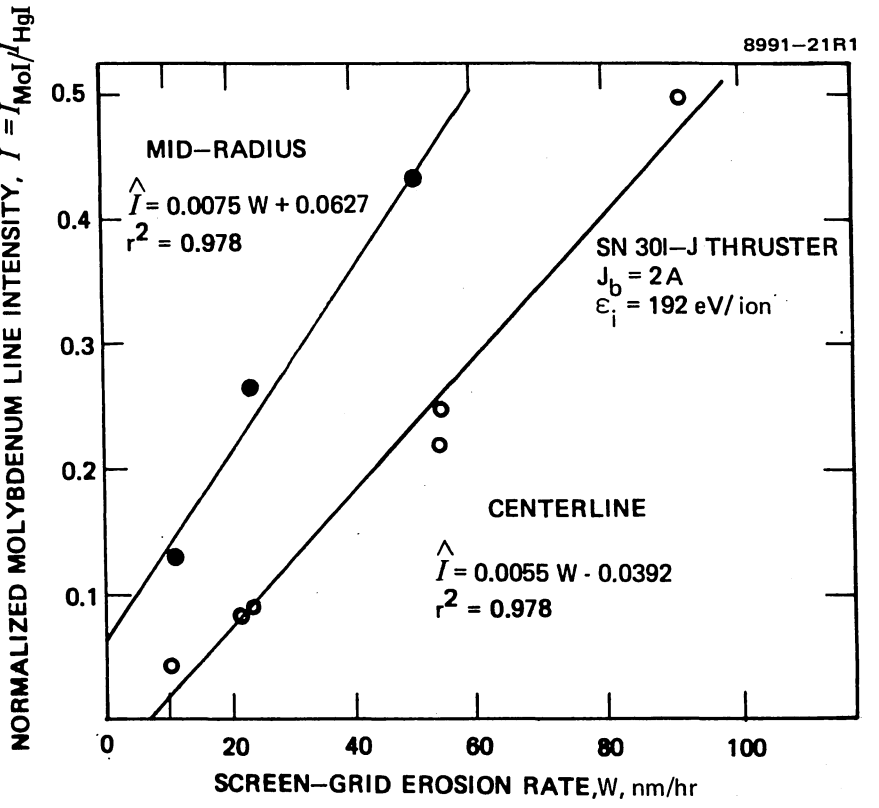

Figure 2-17. Correlation of molybdenum line intensities with screen-grid erosion rates. (λ_{MoI} = 3798.3 Å, λ_{HgI} = 3801.7 Å).

4. Effects of Residual Gases on Discharge-Chamber Erosion Rates

The presence of sufficient quantities of reactive residual gases (such as nitrogen) in the discharge chamber of the 30-cm thruster has been shown[2-4] to reduce the sputtering yield of the molybdenum screen grid. The reduction in wear rates is caused by chemisorption of the reactive gases onto this surface (and probably other chamber surfaces), resulting in the formation of a surface compound such as Mo_2N that has a lower sputter yield than the bare-metal surface. This phenomenon has been observed by other investigators[2-9 through 2-16] in various plasma devices; the reaction process is described in Section 2.D.4. The tests conducted at NASA LeRC[2-4] indicated that when sufficient quantities of nitrogen or air were admitted into an operating 30-cm thruster (either directly or indirectly, by admitting the gases into the vacuum test chamber) the erosion rate of the molybdenum screen grid was reduced. Admitting argon, on the other hand, did not reduce the erosion rate, suggesting that the surface phenomenon involving either nitrogen or air was a chemical reaction. In the present study, the effects of residual gases on surface wear rates were extended to include other gases that are commonly found in vacuum test chambers used in ion-thruster testing. The objectives of this investigation were (1) to determine which of these gases have an effect on the wear rates of critical chamber components, (2) to determine the maximum partial pressures required to simulate the surface sputtering rates expected in space, and (3) to obtain quantitative measurements of the effects of facility-residual-gas pressure on the sputtering rates of critical discharge-chamber components. The results obtained for each of these objectives are discussed below.

a. Line-Intensity Measurements

Measurements of the intensities of each of the spectral lines listed in Table 2-1 were performed while admitting various residual gases into the HRL 9-ft vacuum test chamber using the proportional-control and gas-flow system described above. Figure 2-18 presents the measured

variation of these line intensities that was produced by admitting cyanogen gas into the vacuum chamber. Similar results were observed for all gases investigated (with the exception of argon, which was used as a test case). The pressure data of Figure 2-18 provide only an indication of the pressure rise produced by the admission of the test gas and do not represent either the partial or total pressure near the thruster since they were recorded on the ionization gauge (P1) located behind the chamber cryowall. Figure 2-18 shows that the intensities of the measured mercury lines remained nearly constant as the pressure was increased by about four orders of magnitude. The two molybdenum lines, on the other hand, indicate a factor-of-three reduction in intensity as a result of the presence of the test gas. The observation that the line intensities corresponding to mercury atoms (HgI), singly charged ions (Hg II), and doubly charged ions (Hg III) are insensitive to pressure variation suggests that the average plasma properties are unaffected by the admission of the test gas. Therefore, the change in the molybdenum line intensity should be due to an increase in the density of this material, and good correlation of the line-intensity measurements with direct measurements of screen-grid erosion can be anticipated.

Having confirmed the molybdenum line intensity as the only line source influenced by the increase in pressure caused by introducing residual gases into the test chamber, we proceeded to investigate the sensitivity of the molybdenum line intensity measured at a wavelength of λ = 3798.3 Å to the presence of other contaminant gases such as nitrogen, oxygen, methane, carbon dioxide, and water vapor. For these tests, the SN 301 thruster was equipped with a 900-series ion-optics assembly (SN 653) and was operated at a discharge voltage of V_D = 42 V to accentuate the variation of the molybdenum line intensity with partial pressure. Figure 2-19 presents the measured variation of the molybdenum line intensity (λ = 3798.3 Å) with pressure (recorded on ionization gauge P1), where the pressure rise was produced by admitting the indicated test gases. The line-intensity data have been normalized

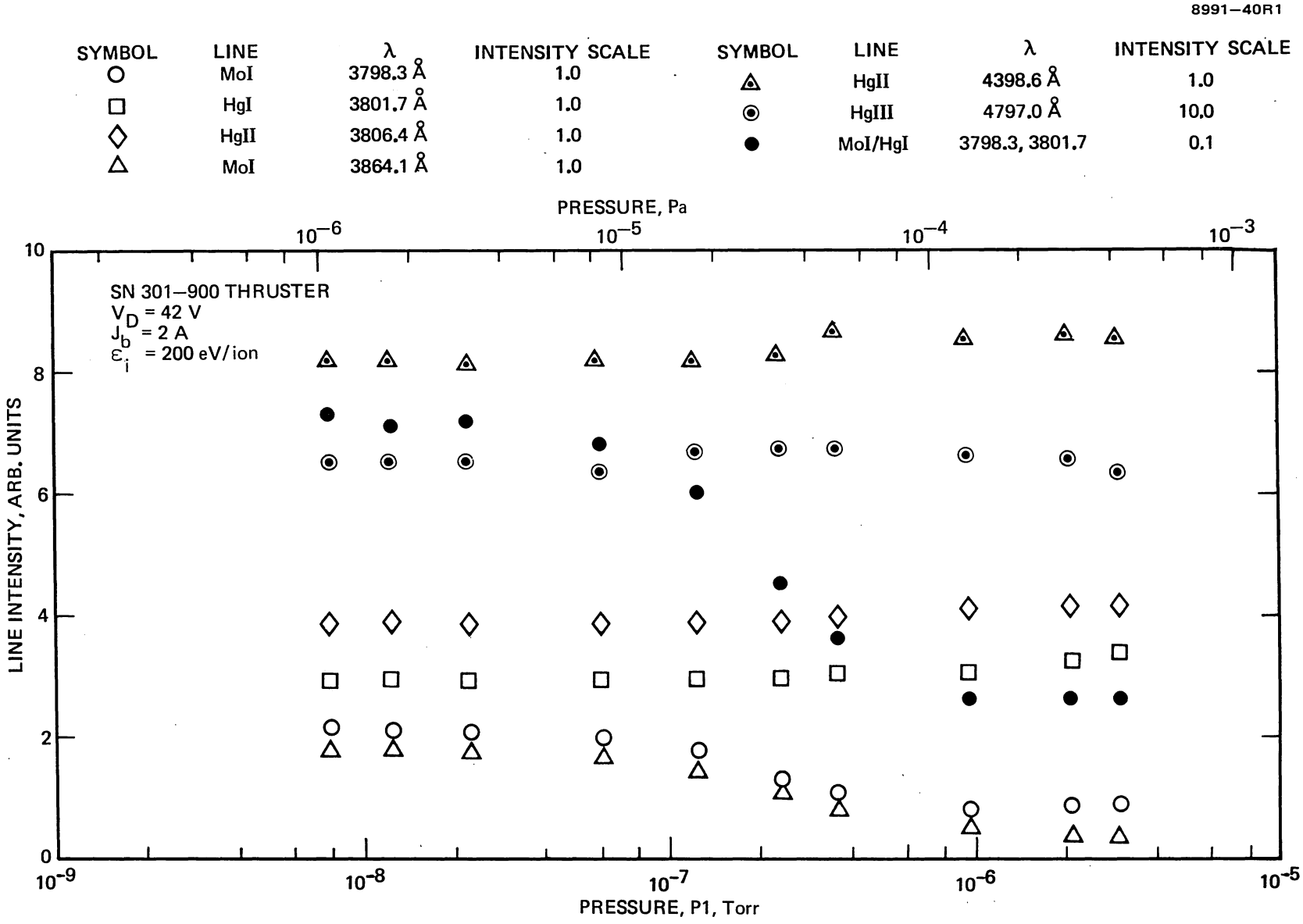

Figure 2-18. Variation of molybdenum and mercury line intensities caused by admitting cyanogen into the vacuum test chamber.

to unity at the lowest pressure point (P_{min}), since at very-low pressures the molybdenum line intensity should be representative of the erosion rate of the bare metal, which is independent of the test gas under consideration. The results of this preliminary survey indicated that each of the candidate contaminant gases produced a substantial reduction in the erosion rate of the screen electrode of the 30-cm thruster. Argon did not lower* the screen-grid erosion, substantiating the suspected chemical nature of the residual-gas effects on surface sputtering. Having identified at least six contaminant gases that retard the screen-grid erosion rate, four of these gases (nitrogen, oxygen, cyanogen, and methane) were selected for further testing to determine the upper bounds on partial pressure levels that must be achieved in vacuum test chambers in order to simulate the surface erosion expected in space. In these tests, the SN 301 thruster was operated with a J-series ion-optics assembly (SN 828) at the standard operating conditions of V_D = 32 V and J_b = 2 A. The variations of the normalized molybdenum line intensity with the partial pressure of nitrogen, oxygen, cyanogen, and methane are presented in Figures 2-20 through 2-23. Because of the substantial reduction in screen-grid erosion achieved with the J-series thruster design, the molybdenum line intensity is significantly lower, resulting in the scatter of the normalized data apparent in these figures. In fact, at the middle and two-thirds chamber-radius locations, the molybdenum line intensity is comparable to the signal noise produced by the dark current of the photomultiplier tube. Smoother curves similar to Figure 2-19 could have been obtained by operating under conditions (such as increased discharge voltage or screen bias) that increase the sputter rate of the screen electrode, but these artificial conditions change the plasma properties and/or ion energy to the extent that the final results may not be representative of standard operating conditions (see Figure 2.23).

---

*The argon data of Figure 2-19 suggest that the erosion rate increases with pressure. This misleading effect is caused by normalization of the molybdenum line intensity by the HgI line intensity, which decreases slightly with pressure in the high-pressure range.

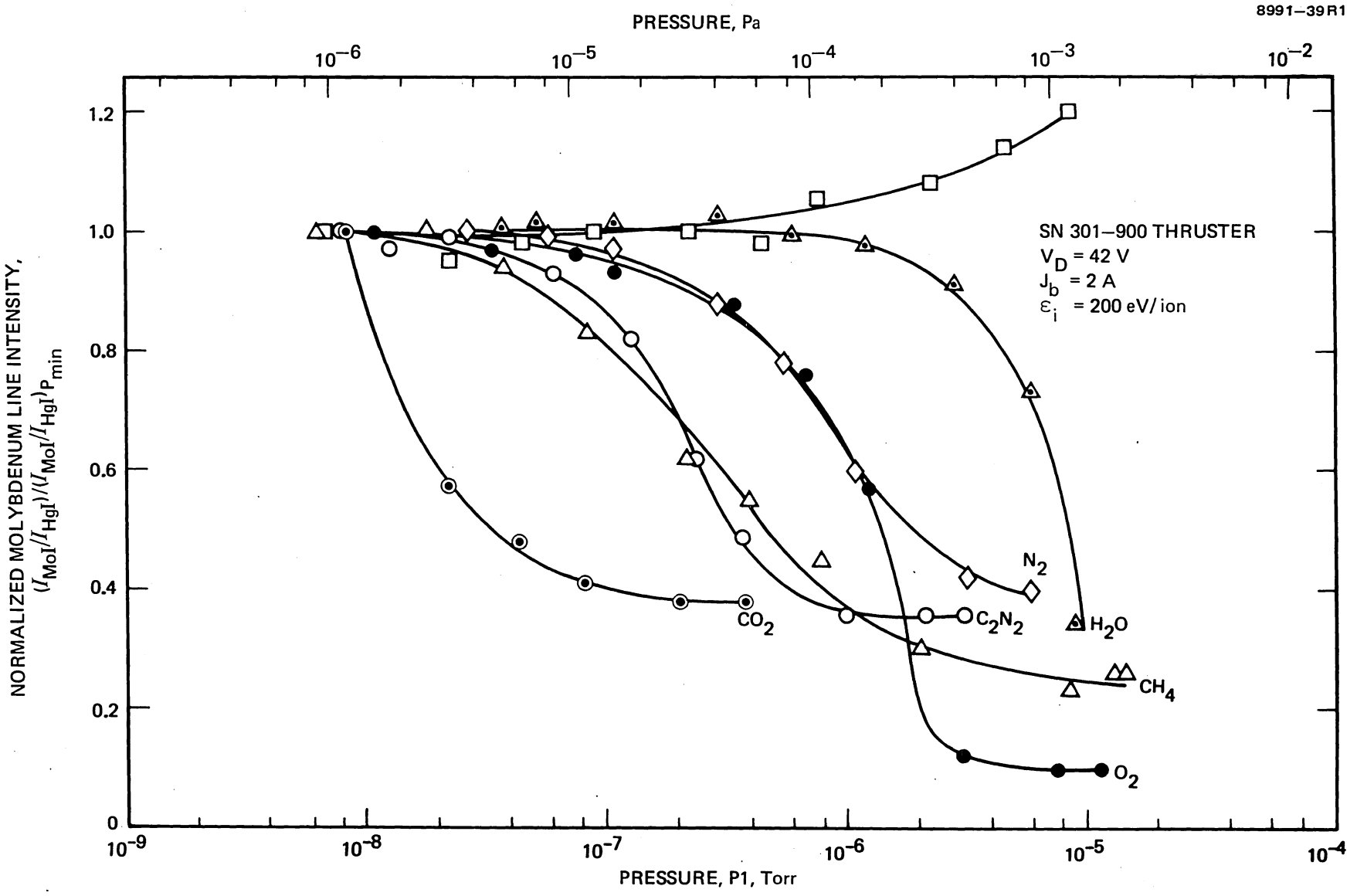

Figure 2-19. Variation of normalized molybdenum line intensity produced by admitting nitrogen, oxygen, carbon dioxide, methane, cyanogen, argon, and water vapor into the vacuum test chamber. (λ_{MoI} = 3798.3 Å, λ_{HgI} = 3801.7 Å).

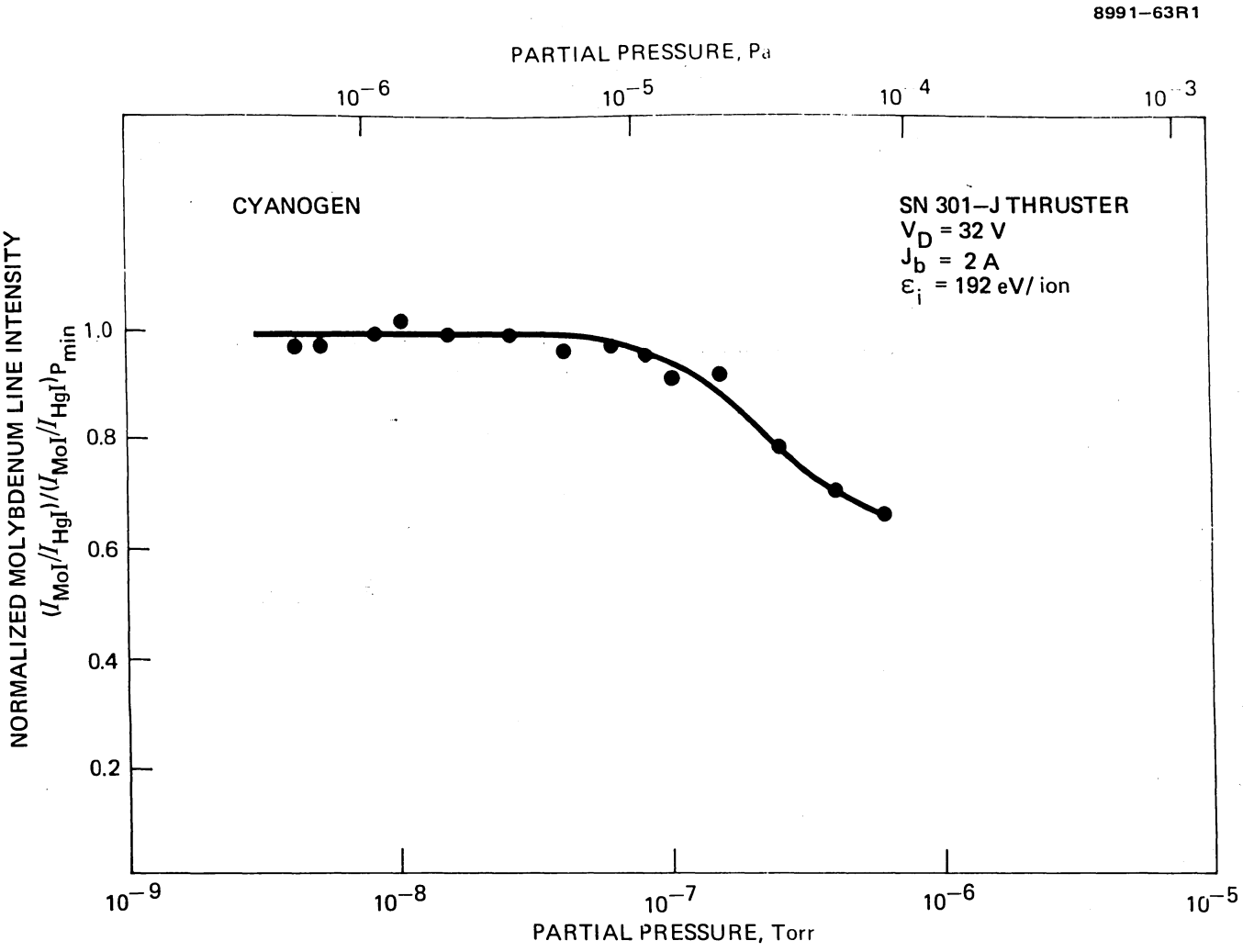

Figure 2-20. Variation of normalized molybdenum line intensity with the partial pressure of cyanogen. (λ_{MoI} = 3798.3 Å, λ_{HgI} = 3801.7 Å).

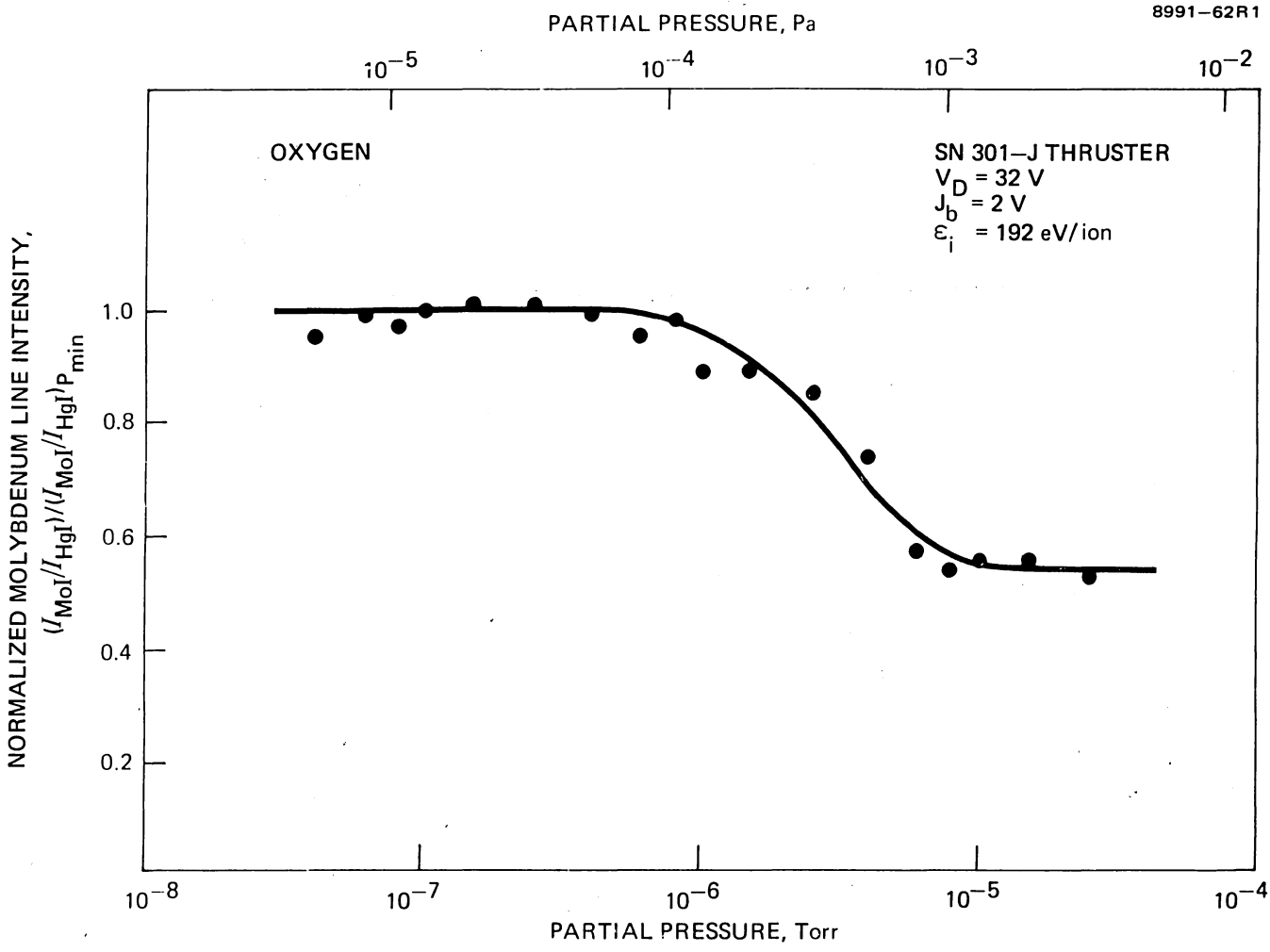

Figure 2-21. Variation of normalized molybdenum line intensity with the partial pressure of oxygen. (λ_{MoI} = 3798.3 Å, λ_{HgI} = 3801.7 Å).

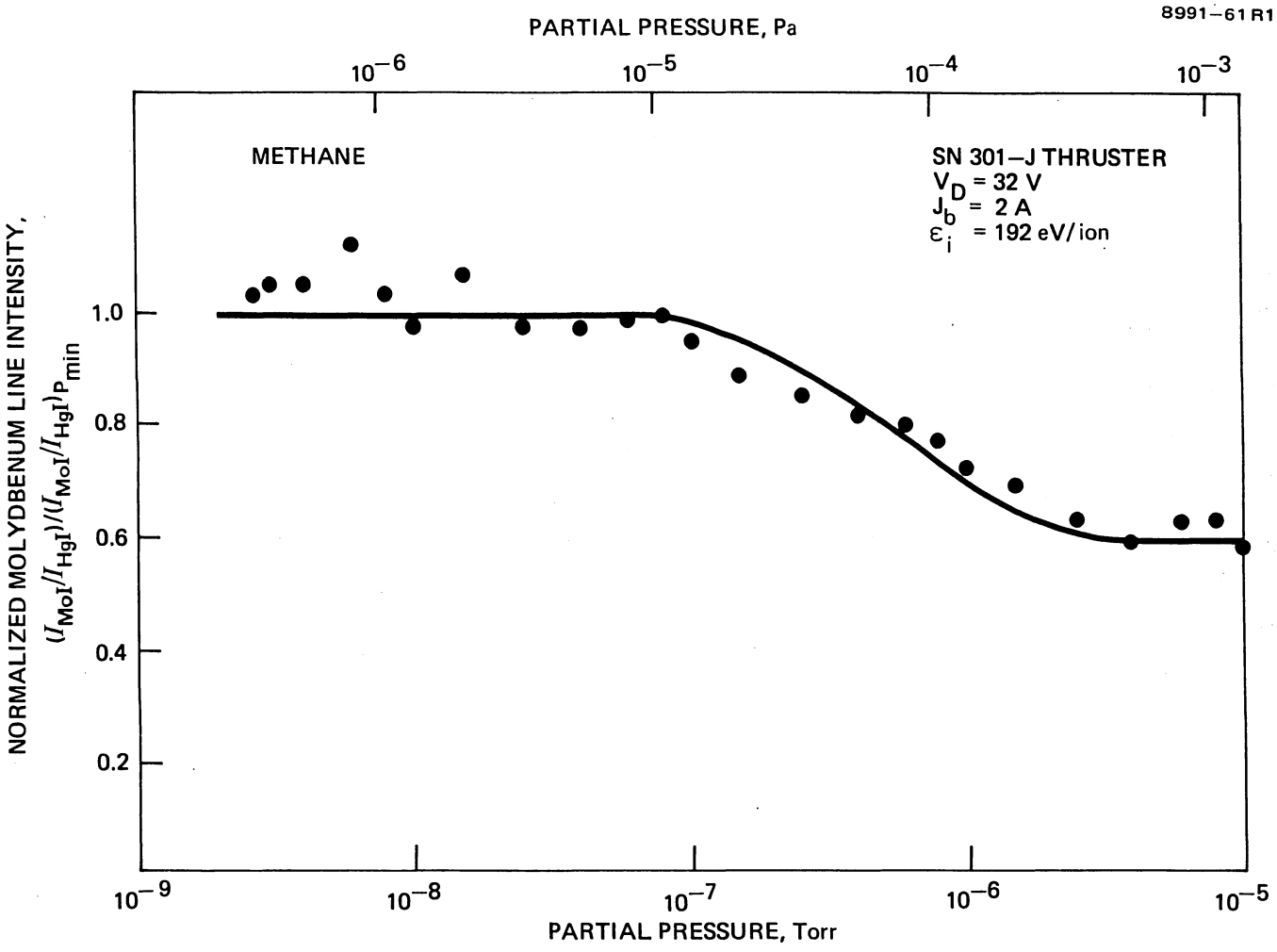

Figure 2-22. Variation of normalized molybdenum line intensity with the partial pressure of methane. (λ_{MoI} = 3798.3 Å, λ_{HgI} = 3801.7 Å).

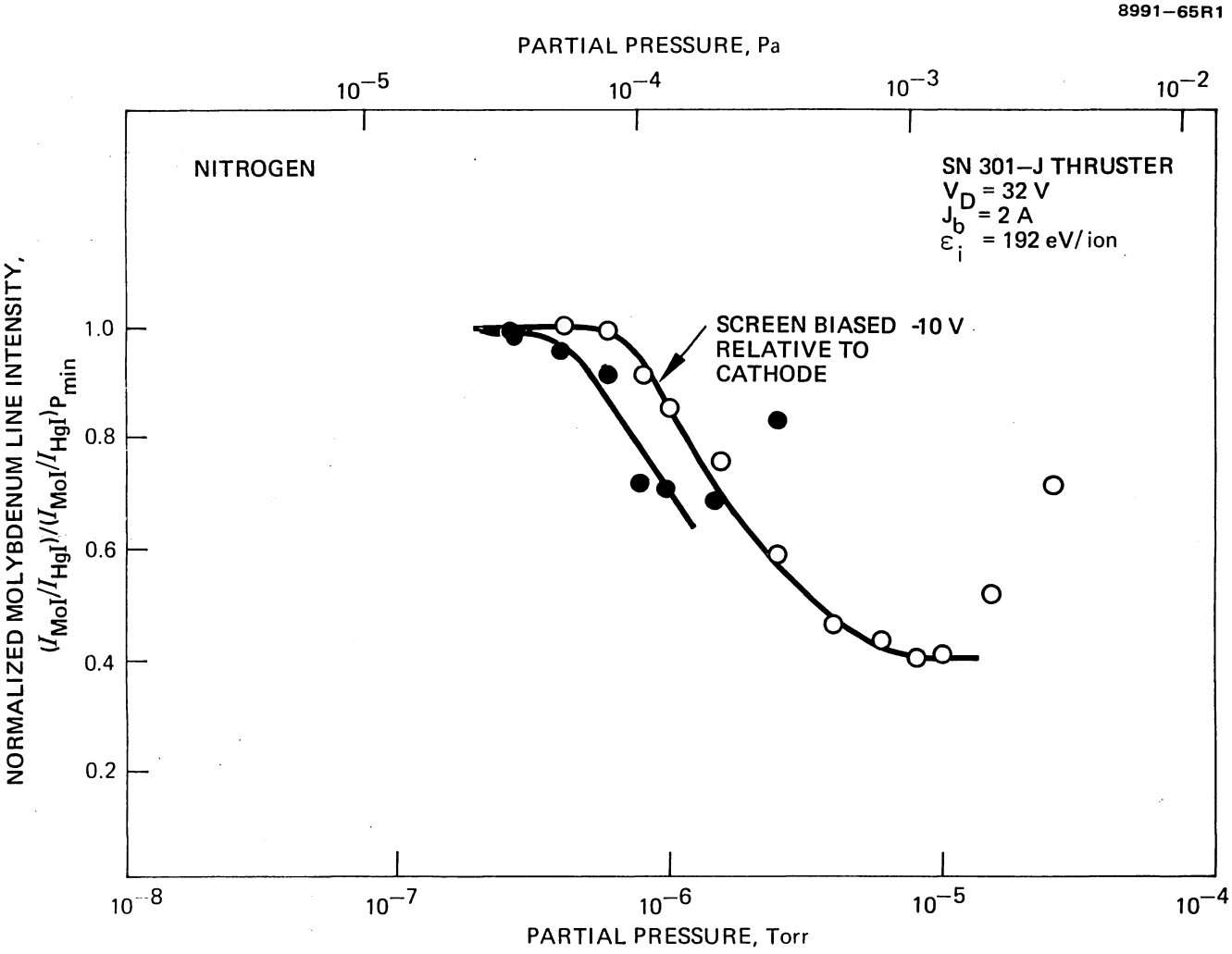

Figure 2-23. Variation of normalized molybdenum line intensity with the partial pressure of nitrogen. The increase in normalized molybdenum line intensity observed at high pressures is caused by an increase in the intensity of the nitrogen line at λ = 3804.9 Å. (λ_{MoI} = 3798.3 Å, λ_{HgI} = 3801.7 Å).

The results given in Figures 2-20 through 2-23 were used to estimate the maximum partial pressure of each test gas that is required to simulate the surface sputtering expected in space. This upper bound on critical pressure was arbitrarily defined as the partial pressure at which the normalized molybdenum line intensity dropped to 0.95, based on the faired curves of Figure 2-20 through 2-23. Table 2-4 presents the values of the critical partial pressures determined in this manner and indicates that partial pressures below the 10^{-5} to 10^{-4} Pa (10^{-7} to 10^{-6} Torr) range are required for these gases to simulate a screen-electrode sputtering-rate that is ∿95% of the value anticipated in space.

b. Erosion-Rate Measurements

Erosion rates of the baffle and screen electrode of the SN 301 thruster were measured at various nitrogen partial pressure levels in the range 10^{-5} Pa $\leq p \leq 10^{-3}$ Pa (10^{-7} Torr $\leq p \leq 10^{-5}$ Torr). For these tests, the 900-series ion-optics assembly (SN 653) was used, and the thruster was operated at discharge-voltage and beam-current conditions of V_D = 36 V and J_b = 2 A, respectively. The 900-series thruster geometry and operating conditions were chosen to permit reasonable test durations at the high-pressure conditions (the use of a J-series ion-optics assembly and 32-V discharge would have required testing for up to 40 hr for pressures above 10^{-4} Pa). The results of these erosion-rate tests are presented in Table 2-5, which shows that increasing the nitrogen partial pressure from 7×10^{-5} Pa to 2×10^{-3} Pa reduced the maximum screen-grid erosion rate by a factor of five. The erosion rates of the tantalum baffle are also observed to decrease with pressure, indicating that the nitrogen chemisorption effect is not unique to molybdenum. The measured erosion rates on the cathode side of the baffle do not indicate a consistent reduction in erosion rate with partial pressure because of the anomalously high erosion rate measured at a partial pressure of 6.1×10^{-4} Pa. This inconsistency is thought to be a result of the interpretation difficulties that are sometimes encountered with the baffle erosion monitors.

Table 2-4. Maximum Partial Pressures Required to Simulate Space-Erosion Conditions (SN 301-J Thruster Operated at V_D = 32 V, J_b = 2 A, and ε_i = 192 eV/ion)

Contaminant Gas	Maximum Partial Pressure	
	Pa	Torr
Nitrogen	6.2×10^{-5}	4.7×10^{-7}
Oxygen	1.5×10^{-4}	1.1×10^{-6}
Cyanogen	1.2×10^{-5}	9.0×10^{-8}
Methane	2.0×10^{-5}	1.5×10^{-7}

6758

5. Magnetic Baffle Current Effects

The effect of magnetic baffle current on the screen-grid erosion rate was investigated using the optical-spectroscopy technique to monitor the molybdenum and mercury line intensities over a wide range of magnetic baffle current. This approach was selected because the effects of this operating parameter on the erosion rate of the screen grid were judged a priori to be small and probably of the order of the uncertainty in the thin-film measurement technique. Figure 2-24 presents measurements of the normalized molybdenum line intensities for magnetic baffle currents in the range $1.6 \leq J_{MB} \leq 3.6$ A. Two sets of data are presented in the figure, corresponding to the optical-system masks which permit light from the entire chamber or centerline regions to reach the monochromator. The mid-radius mask was not used in these tests because the signal-to-noise ratio at the 32-V discharge-voltage condition is too small to permit accurate detection of small signal

Table 2-5. Erosion-Rate Measurements Obtained with the SN 301-900 Thruster Operated at Various Nitrogen Partial-Pressure Levels (V_D = 36 V, J_b = 2 A, and ε_i = 200 eV/ion)

No.	Nitrogen Partial Pressure		Erosion Rate, nm/hr				U, nm/hr
			Screen Grid		Baffle		
	Pa	Torr	r = 0	r = $R_T/2$	Discharge Side	Cathode Side	
1	7.0×10^{-5}	5.3×10^{-7}	52.9	24.5	41.9	25.5	5.0
2	1.5×10^{-4}	1.1×10^{-6}	53.0	26.0	—	—	5.0
3	6.1×10^{-4}	4.6×10^{-6}	40.4	13.4	25.5	35.8	5.0
4	2.0×10^{-3}	1.5×10^{-5}	10.9	3.0	5.1	9.2	3.0

6785

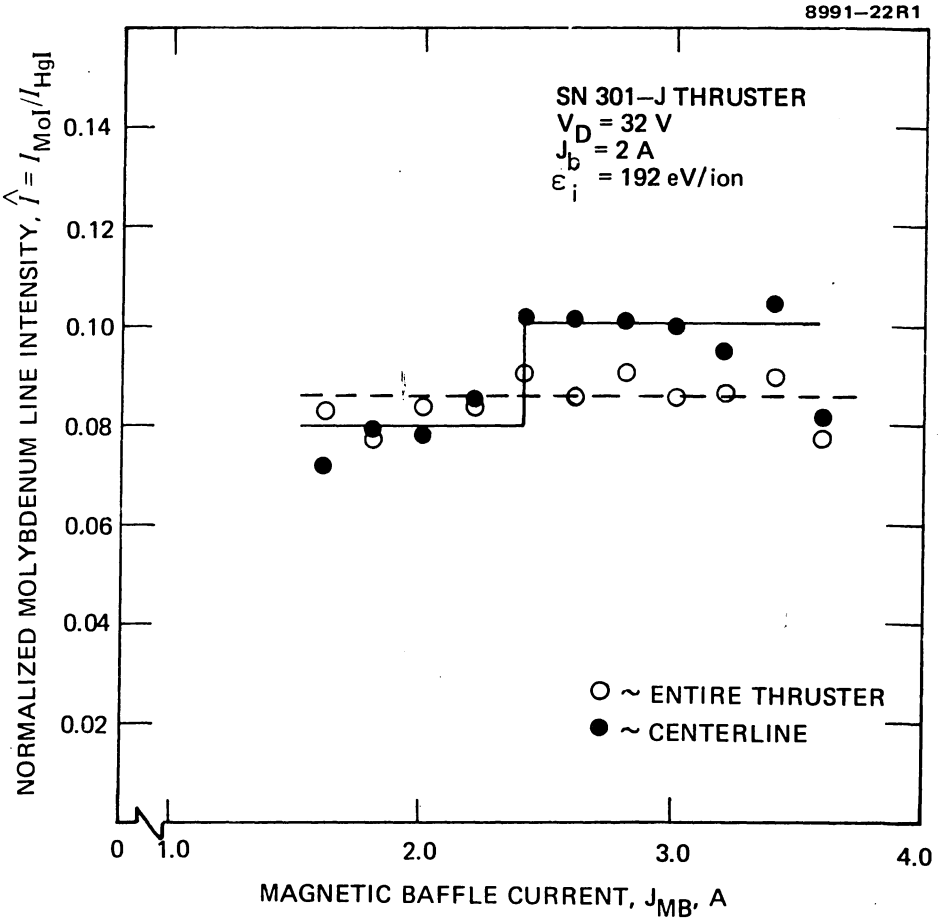

Figure 2-24. Variation of normalized molybdenum line intensity with magnetic baffle current. (λ_{MoI} = 3798.3 Å, λ_{HgI} = 3801.7 Å).

changes. The relatively weak intensity of the molybdenum line is manifest in the scatter of the results given in Figure 2-24. In spite of the scatter, however, some trends are evident. First, the data from the entire thruster suggest little, if any, effect of magnetic baffle current on the overall wear rate of the screen electrode. This result is consistent with the expectation that magnetic baffle current or cathode flow rate should have a negligible effect on the overall erosion of the screen grid. Second, the centerline results of Figure 2-24 indicate that the magnetic baffle may produce a localized effect on screen-grid erosion. The line intensities measured on centerline appear to fall into one of two regions characterized by a nearly constant value of normalized molybdenum line intensity. The transition between these regions occurs at a magnetic baffle current of approximately $J_{MB} = 2.4$ A. Below this value, the normalized intensity is approximately $\hat{I} = 0.08$; above $J_{MB} = 2.4$ A, the normalized intensity is approximately $\hat{I} = 0.10$. The correlation of line-intensity and erosion-rate measurements presented in Figure 2-17 can be used to calculate erosion rates corresponding to these two intensity values. From Figure 2-17, the centerline erosion-rate and line-intensity data are related by the expression

$$W = 182\ \hat{I} + 7 \quad , \tag{2.8}$$

resulting in calculated erosion rates of 21.6 and 25.2 nm/hr for the two regions of Figure 2-24. Because the difference in these rates is about the same as the uncertainty of the thin-film erosion rate measurement technique, direct verification of the effects of magnetic baffle current on the erosion rate of the screen grid on centerline was not considered to be feasible.

6. Ion-Flux Measurements

Measurements of the screen-electrode ion-saturation current were conducted over a wide range of beam-current and beam-voltage operating conditions by biasing the electrically isolated screen electrode of the

SN 301-J thruster up to 30 V negative of cathode potential. Typical current-voltage curves obtained in this manner are presented in Figure 2-25. The linear range of the measured current-voltage curves was extrapolated to zero (cathode) potential to provide an estimate of the ion-arrival rate at the screen grid. The ion current determined in this manner was used to calculate the effective screen-electrode transparency, ϕ_s, using the expression

$$\phi_s = \frac{J_b}{J_b + J_{screen}} \quad , \tag{2.9}$$

where J_b is the beam current, and J_{screen} is the extrapolated screen-electrode current. The results of these measurements, presented in Figure 2-26, show the variation of screen-grid transparency with beam current and voltage. The trends evident in Figure 2-26 can be explained by considering the location of the plasma sheath necessary to satisfy the conditions of space-charge-limited ion flow through the accelerator system apertures: (1) At constant beam current, an increase in beam (total) voltage causes the plasma sheath to move upstream, which reduces the surface area available for ion recombination and, as a consequence, an increase in the effective transparency of the screen electrode. (2) At a constant beam (total) voltage, an increase in beam current causes the plasma sheath to move downstream, resulting in an increase in the surface area available for recombination, and, consequently, a reduction in the effective transparency. The experimental results of Figure 2-26 can be approximated by the indicated curve fits, which have the form

$$\phi_s = 0.781 + 0.084\ V_T - 0.062\ J_b \quad , \tag{2.10}$$

where V_T is the total accelerating voltage. The optical or geometric transparency of the J-series screen electrode is $\phi = 0.674$.

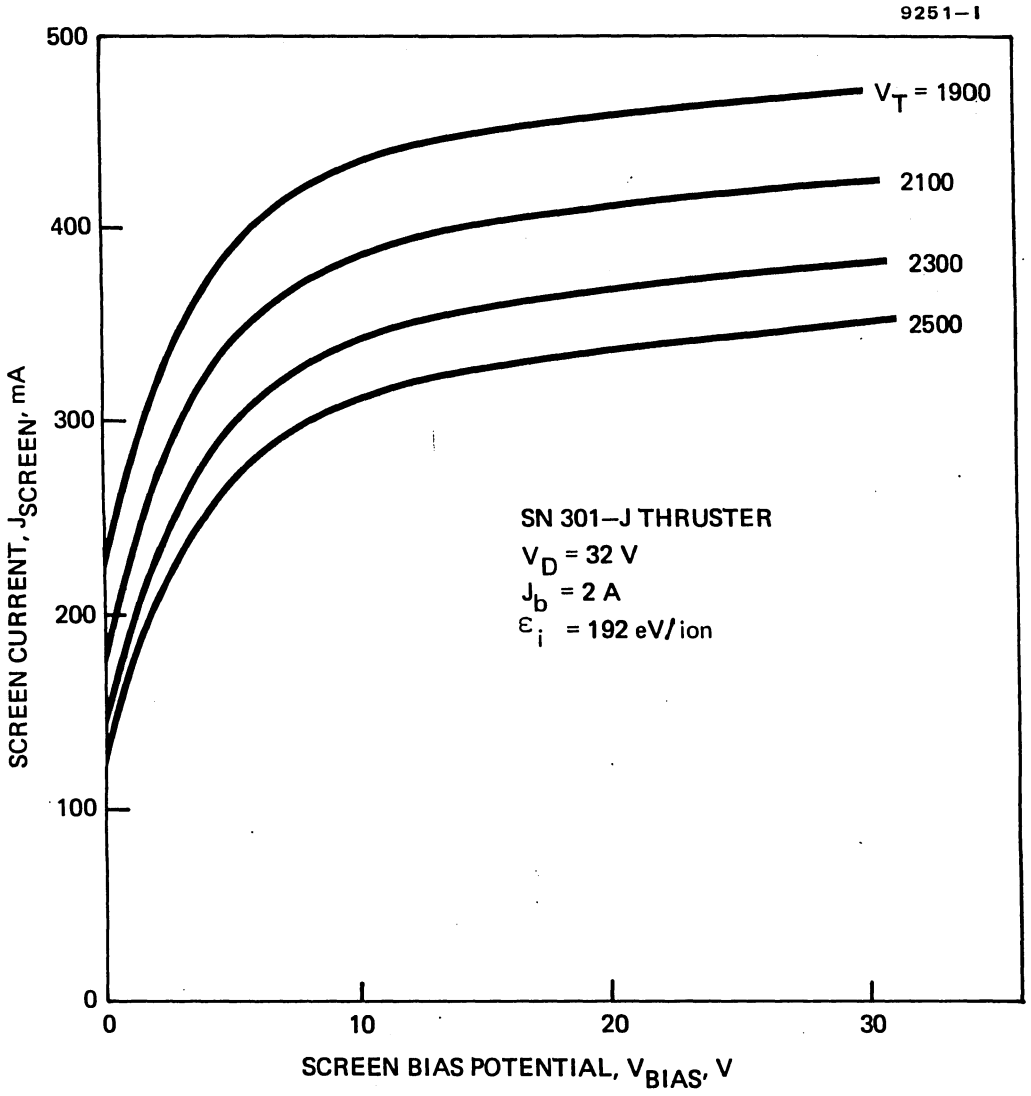

Figure 2-25. Variation of screen-electrode current with bias potential (relative to cathode).

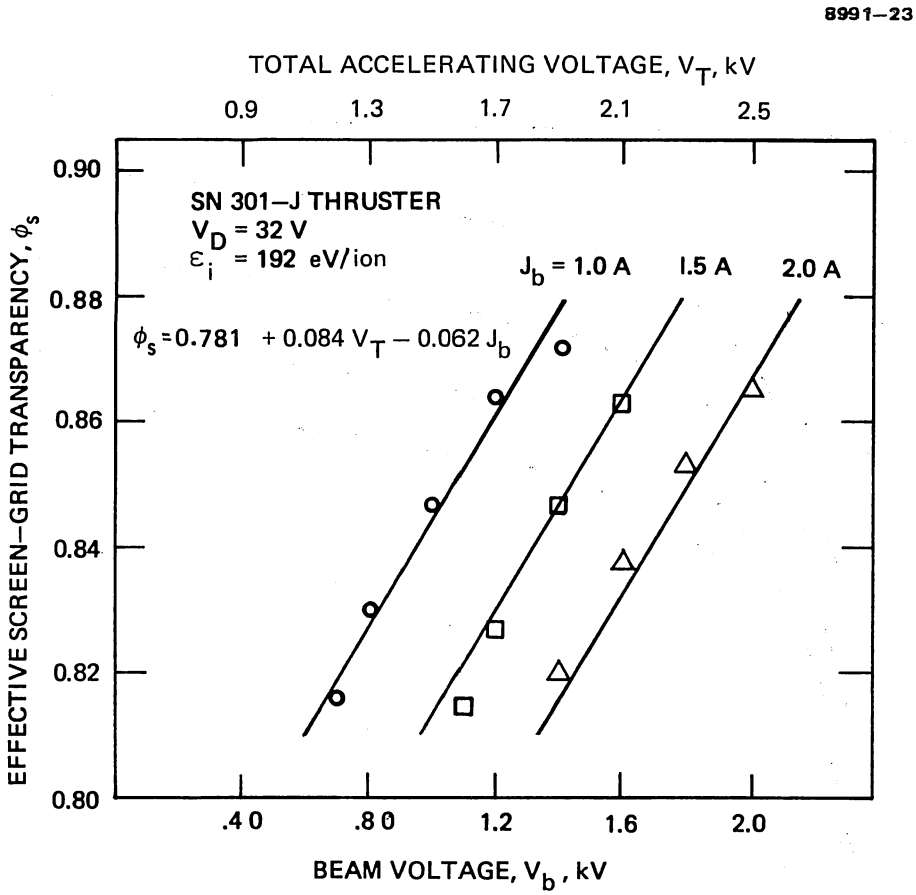

Figure 2-26. Variation of screen-grid transparency with beam current and beam voltage. (The optical or geometric transparency of the screen electrode is ϕ = 0.674.)

7. Plasma-Potential Measurements

Because of the relatively slow ion velocity within the thruster discharge chamber, the energy of the ions striking the chamber surfaces is determined primarily by the difference in potential between the plasma and the adjacent surface. Therefore, an understanding of the physical sputtering phenomena occurring in the 30-cm thruster requires knowledge of the plasma-potential variation within the chamber, particularly near the surfaces of critical chamber components. The spatial variation of the plasma potential within the SN 301-J thruster discharge chamber was obtained by conducting Langmuir-probe measurements at the locations indicated in Figure 2-27. The measurements were performed using an automated data-acquisition system[2-3] to digitize and record the probe I-V signals. In addition to the digital data, analog signals proportional to probe voltage and the logarithm of the probe current were recorded on an x-y plotter. Figure 2-28 presents current versus voltage curves typical of those obtained during the Langmuir-probe measurements. The extremely linear variation in the logarithm of probe current in the retarding-field region of the characteristic indicates that the plasma-electron distribution is essentially Maxwellian. Although this observation is contrary to the generally accepted theory of a two-group plasma, all the recorded probe characteristics were observed to be linear over nearly two decades of probe current. The absence of a monoenergetic or primary-electron contribution to the probe-collector current suggests that the electrons drawn out of the cathode-discharge plasma region are rapidly randomized through collisions with neutrals. The electron mean free path is shorter in thrusters operated with low-transparency accelerator grids, such as the J-series SHAG optics, due to the inherent increase in neutral density.

The dependence of the electron distribution function on mean free path has been observed in similar plasma devices operated on argon,[2-17] where it was found that the plasma contained a monoenergetic and Maxwellian electron group only below a certain value of neutral

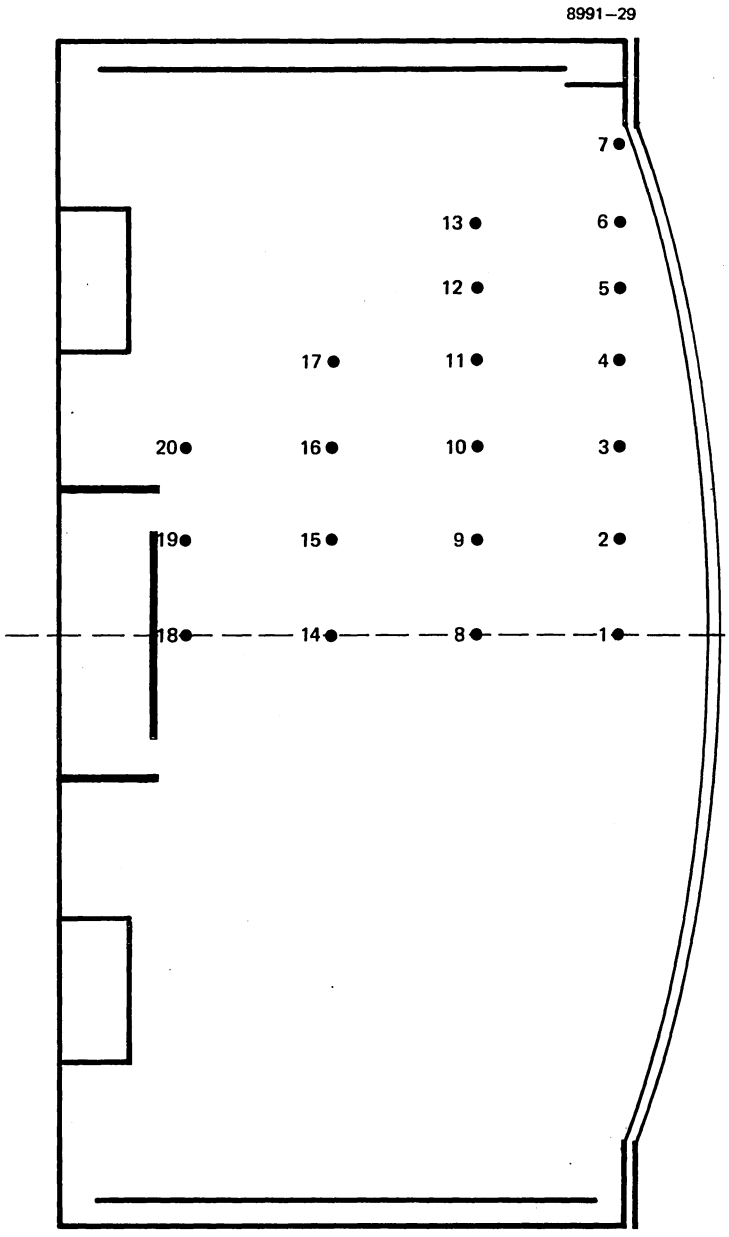

Figure 2-27. Locations of Langmuir-probe measurements performed in the SN 301-J thruster.

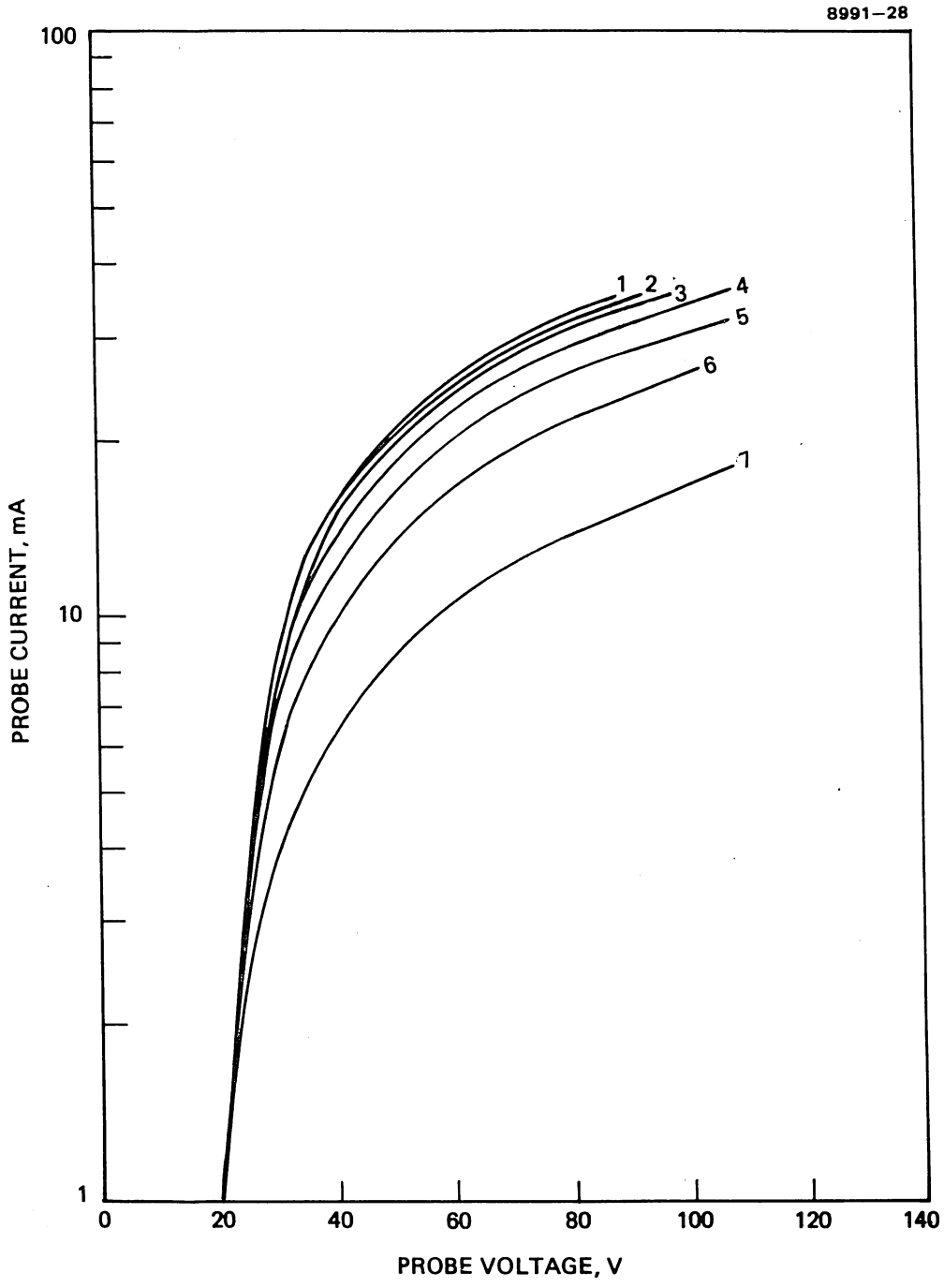

Figure 2-28. Typical Langmuir-probe measurements. Identification numbers on curves correspond to the probe positions indicated in Figure 2-27.

density. Above this critical density, the electron energy-distribution function was observed to be essentially Maxwellian, as deduced from the shape of the Langmuir probe characteristic in the retarding-field region. In these studies,[2-17] the chamber was operated at a 60-V discharge on argon, and a critical chamber pressure of about 10^{-2} Pa (10^{-4} Torr) was observed. At a pressure of 10^{-3} Pa (10^{-5} Torr), the probe characteristic contained a well-defined linear region due to the collection of monoenergetic electrons. At 10^{-2} Pa (10^{-4} Torr) and above, there was no linear region of the probe characteristic, indicating that the plasma electron distribution was essentially Maxwellian. If the phenomenon observed in the argon plasma device[2-17] is the result of the existence of a critical mean free path, then similar results might be expected in the 30-cm thruster, but at a lower pressure due to the larger ionization cross section of mercury. Based on the critical-path-length concept, the critical pressure P_{Hg} in a mercury discharge can be estimated using the expression

$$P_{Hg} = P_{Ar} \frac{\sigma_{Ar}}{\sigma_{Hg}} , \qquad (2.11)$$

where σ is the ionization cross section. Using the argon critical pressure of 10^{-2} Pa (10^{-4} Torr) and the ratio of the ionization cross sections of argon and mercury evaluated at 60 V and 30 V, respectively, results in a calculated critical mercury pressure of 6.5×10^{-3} Pa (5×10^{-5} Torr). The calculated partial pressure of mercury within the discharge chamber of the 30-cm thruster operated with SHAG optics is $\sim 10^{-2}$ Pa ($\sim 8 \times 10^{-5}$ Torr), which is somewhat higher than the estimated critical pressure. At the same chamber propellant utilization, the estimated pressure in the 30-cm thruster operated with 900-series and earlier optics (43% accelerator electrode open area) is $\sim 5 \times 10^{-3}$ Pa (4×10^{-5} Torr), which is slightly lower than the estimated critical pressure. Although the possibility of an effect of accelerator-electrode design on the electron energy distribution within the 30-cm thruster is of prime interest to an understanding of discharge-chamber operation, further study of this phenomenon was not pursued under the present investigation.

The linear variation in the log-current/voltage characteristics renders them amenable to the simple graphical analysis technique of classical Langmuir probe theory. Using this technique, the plasma potential was found from the intersection of two lines: one drawn tangent to the curve in the retarding-field region of the characteristic and the other drawn tangent to the curve in the accelerating-field region slightly beyond the plasma potential. The local values of plasma potential ϕ_p found in this manner are presented in Table 2.6. As expected, the plasma potential is nearly equal to the discharge (anode) potential and essentially independent of beam current. From the results in Table 2.6, the plasma potential near the screen grid is given by the following expression:

$$\phi_p = 1.28\ V_D - 9.38 \quad , \tag{2.12}$$

where V_D is the discharge voltage in V.

8. Erosion Rates of Alternate Fabrication Materials

The use of a lower-sputter-yield material for fabricating the screen electrode of the 30-cm thruster is one possible way of increasing the thruster lifetime beyond that achieved with molybdenum electrodes. A previous study[2-2] conducted under NASA Contract NAS 3-19703 identified several low-sputter-yield metals that might be suitable as an alternate choice of screen-electrode material. Of the possible candidate materials identified during that study, tantalum, titanium, and niobium were recommended as alternate choices to molybdenum based on considerations of fabrication (chemical etching), availability, and thermal properties. During the present study, we investigated the relative sputtering rates of these alternate materials when they are subjected to the discharge environment of the 30-cm thruster.

Measured sputter yields[2-18] of various materials bombarded by normally incident mercury ions are presented in Figure 2-29. If one considers the combined effects of sputtering by singly and doubly charged ions, a clear-cut choice of the optimum low-sputter-yield

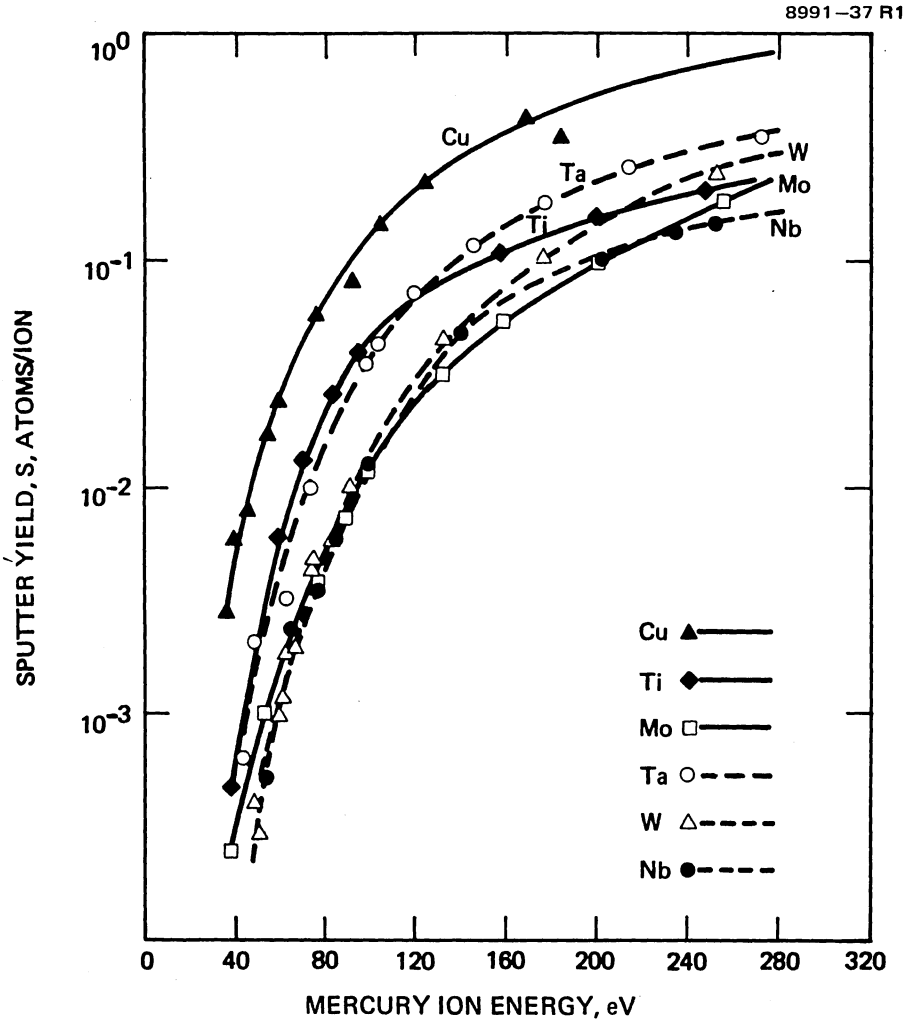

Figure 2-29. Sputter yields of various metals when bombarded by mercury ions (Ref. 2-18).

Table 2-6. Summary of Discharge-Chamber plasma-Potential Measurements Obtained in the SN 301-J Thruster

Probe Position	Plasma Potential (ϕ_p), V					
	Discharge Voltage[a] (V_D), V			Beam Current[b] (J_b), A		
	29	32	36	1.0	1.5	2.0
1	27.8	31.8	36.8	33.4	32.6	31.8
2	27.8	31.8	36.6	33.4	32.6	31.8
3	27.6	31.6	36.2	33.4	32.4	31.6
4	27.0	31.0	36.0	32.4	32.0	31.0
5	26.6	31.8	36.0	33.6	32.0	31.8
6	27.0	31.0	35.6	33.4	32.0	31.0
7	25.0	30.0	34.2	35.4	32.0	30.0
8	29.2	32.8	38.0	33.8	33.0	32.8
9	29.0	32.8	37.8	33.8	33.0	32.8
10	28.8	34.4	37.6	33.6	32.6	34.4
11	28.6	33.0	38.0	34.0	36.0	33.0
12	29.4	33.0	37.4	34.2	33.6	33.0
13	30.6	33.6	38.6	38.0	35.0	33.6
14	29.6	33.2	39.0	34.0	33.6	33.2
15	29.0	33.0	39.0	34.0	33.4	33.0
16	39.8	32.0	39.5	34.4	34.0	32.0
17	31.0	34.4	39.5	37.4	35.4	34.4
18	28.0	32.0	37.0	32.6	32.4	32.0
19	27.8	32.6	36.5	32.6	33.6	32.6
20	35.0	36.0	41.0	—	38.6	36.0

[a] J_b = 2 A, ε_i = 192 eV/ion.

[b] V_D = 32 V, ε_i = 192 eV/ion.

6758

material is not immediately obvious because of the crossover of the curves in Figure 2-29. However, using an expression for erosion rate developed in Section 2.D and the data from Figure 2-29, the combined effects of sputtering by both singly and doubly charged ions can be accounted for, enabling relative sputtering rates to be estimated. The erosion rate W of the screen electrode can be written in the form

$$W \propto \frac{2S(E) + JS(2E)}{n} , \tag{2.13}$$

where S is the sputter yield at energy E, n is the density of the material, and J is the ratio of doubly to singly charged ion currents. The experimental data of Figure 2-29 are observed to be nearly linear in the low-energy range, allowing the sputter yields to be approximated by the expression

$$S(E) = Ae^{BE} , \tag{2.14}$$

where A and B are constants that can be determined from curve-fitting the low-energy region of the curves in Figure 2-29. Combining Eqs. 2.13 and 2.14 yields a simplified expression for a quantity f that is directly proportional to erosion rate:

$$f = \frac{Ae^{BE}}{n} (2 + Je^{BE}) . \tag{2.15}$$

The quantity f, normalized by the value calculated for molybdenum, can be thought of as a figure of merit (relative to molybdenum) for sputtering of a given material subjected to plasma conditions specified by the choice of ion energy E and the ratio of doubly to singly charged ion currents J. Table 2-7 presents calculated values of the relative wear rates of several materials subjected to plasma conditions defined by

Table 2.7. Normalized Wear Rates of Various Materials

Material	A x 10^5 Atoms/Ion	B, $(eV)^{-1}$	n x 10^{-22}, cm^3	f x 10^{27}, cm^3	f/f_{Mo}
Nb	0.90	0.082	5.44	3.54	0.76
W	0.04	0.138	6.32	3.60	0.77
Mo	1.93	0.077	6.40	4.67	1.00
Ta	1.26	0.102	5.52	14.7	3.14
Ti	0.75	0.113	5.66	16.2	3.47
Cu	3.15	0.127	8.48	105.0	22.5

A and B are constants obtained from curve-fitting the data of Figure 2-29, n is density of the electrode material, and f was calculated using Eq. 2.15 with E = 32 V and J = 0.3.

E = 32 V and J = 0.3 (representative of the J-series thruster operating at its nominal discharge voltage V_D = 32 V). The values of the constants A and B were obtained from digitizing and curve-fitting the low-energy region of the curves of Figure 2-29. The normalized wear rates presented in the last column of Table 2-7 indicate that niobium and tungsten sputter at a rate that is about three-fourths that of molybdenum, while copper erodes nearly 25 times faster.

The relative erosion rates of various metals subjected to the plasma environment of the 30-cm thruster were measured using thin-film erosion monitors fabricated from molybdenum, niobium, tantalum, titanium, gold, and silver. Gold and silver were of interest because they will amalgamate with mercury. A preliminary test was conducted with erosion monitors located on the screen electrode $\sim$1 cm from the center. The SN 301-J thruster was operated at 32-V discharge voltage and 2-A beam current for a period of 3.5 hr, with the screen electrode biased 15 V negative of cathode potential to accelerate the wear rate. An examination of the monitors after the test revealed no visible copper lines on either the silver, gold, tantalum, or titanium monitors, and only a single copper line was visible on the molybdenum monitor; five copper lines were visible on the niobium monitor. The calculated

erosion rates based on these results are 41 nm/hr for niobium, 110 nm/hr for molybdenum, and ≥135 nm/hr for gold, silver, titanium, and tantalum. Because the sputtering rate of the niobium monitor was substantially less than the rate observed for molybdenum, a second test was run at nominal chamber operating conditions of V_D = 32 V and J_b = 2 A, but without electrical bias of the screen electrode.

A niobium monitor was placed at the center of the grids, and thin-film monitors fabricated from niobium, molybdenum, tantalum, and titanium were placed near (∿1 cm) the center of the screen electrode, equidistant from the center. The duration of this test was 11 hr, resulting in an uncertainty in the erosion-rate measurements of ±2.7 nm/hr. The niobium erosion monitor mounted at the center of the screen grid indicated an erosion rate of 14.2 nm/hr, which is about two-thirds the value shown in Table 2-3 for molybdenum monitors operated at the same beam conditions. The relative erosion rate of the niobium monitor is in good agreement with the calculated values given in Table 2-7 (f/f_{Mo} = 0.76). Post-test examination of the tantalum and titanium monitors, located ∿1 cm from the center of the electrode, revealed that there were no visible lines remaning after the test, indicating an erosion rate ≥42.8 nm/hr. This value is consistent with the results of Tables 2-3 and 2-7, which indicate an anticipated erosion rate near the center of the screen electrode of about 75 nm/hr for both tantalum and titanium. The niobium monitor located approximately 1 cm from the center of the electrode indicated an erosion rate of 14.2 nm/hr, in agreement with the center monitor. The molybdenum monitor located 1 cm from the center also indicated an erosion rate of 14.2 nm/hr. This result is anomalous since the results given in Table 2-3 indicate that the erosion at the center is substantially higher.

The results of the investigation of low-sputter-yield materials indicate that the niobium erosion rate is only 40 to 70% of the corresponding values for molybdenum. These preliminary results, which were anticipated based on the relative sputter-yield calculations presented in Table 2-7, suggest that the use of niobium in fabricating the screen electrode of the 30-cm thruster may signficantly extend its lifetime.

The feasibility of using niobium to fabricate electrodes is contingent on finding a commercial vendor that can perform the chemical milling process.

9. Alternate Discharge-Chamber Designs

Maximum wear rates of 30-cm thruster discharge-chamber surfaces occur near the axis of the chamber where the plasma density is highest. Therefore, a discharge-chamber design that results in a more uniform plasma-density distribution is desirable in order to increase the chamber lifetime (at constant beam current), or increase the maximum beam current capability (for a fixed lifetime). The local ionization rate is proportional to the product of the electron and neutral densities, suggesting that an increase in ion production is possible by increasing the local density of either species. The feasibility of increasing the electron and neutral densities in the region near the cylindrical boundary of the 30-cm thruster discharge chamber was investigated using two alternate chamber configurations. The first design employed a single-cusp-magnetic-field geometry to confine the ionizing electrons, resulting in an increase in electron density near the chamber wall. The second design used the conventional divergent-magnetic-field configuration, but employed an anode geometry that was designed to increase the residence time of neutrals in the vicinity of the chamber wall.

a. Magnetic Field Geometry

The use of a single-cusp boundary-type magnetic field to achieve a uniform plasma-density distribution in bombardment-type discharge chambers has been investigated in past studies involving both 15- and 30-cm-diameter thrusters.[2-8,2-19] The objective of the present investigation was to evaluate the effects of plasma uniformity on screen-grid erosion, providing additional data for use in formulating a model of wearout lifetime. The Hughes 30-cm-diameter experimental thruster (EXP) has the capability of operating with either a divergent or a

boundary-type magnetic field configuration by simply reversing the polarity of the radial magnets located on the chamber backplate. This arrangement results in a highly versatile discharge chamber for use in ion-thruster research. However, it must be emphasized that no attempt has been made to optimize the chamber design, and, therefore, the performance of this thruster can be expected to fall short of the current J-series-thruster design goals, particularly in the single-cusp-magnetic-field configuration.

Beam-current-density profiles were obtained for the EXP thruster operated with divergent and single-cusp magnetic-field geometries. These results, presented in Figure 2-30, show the dramatic improvement in plasma-density uniformity achievable with the single-cusp magnetic field geometry. The reduction in maximum plasma density in the central region of the chamber suggests that the erosion rate in this region should be considerably lower than the corresponding wear rates of divergent-field geometries. This hypothesis was verified by conducting erosion-rate measurements using thin-film monitors mounted at the centerline and mid-radius of the screen grid. The experimental thruster was operated with a single-cusp magnetic-field geometry using a 900-series optics design for a total accumulated test time of 20.7 hr at a 36-V discharge voltage and a 1.6-A beam current. The measured screen-grid erosion was 4.5 ± 1.5 nm/hr at both the center and mid-radius locations. An extrapolation of these results to provide an estimate of the erosion rate expected at a 2-A beam current can be made by multiplying the measured erosion rate by the ratio of beam currents. This results in a predicted value of 6 nm/hr. The actual value can be expected to be somewhat higher than this estimate because the increased erosion rate caused by an increase in doubly charged ion density has not been accounted for in the extrapolation. There are two contributing factors to this effect: (1) a linear increase in plasma density with beam current, and (2) a second-order increase in doubly charged ion concentration with plasma density. These uncertainties are expected to have little, if any, impact on the observation that the erosion rates are the same at the centerline and mid-radius locations. Based on this finding and the results in

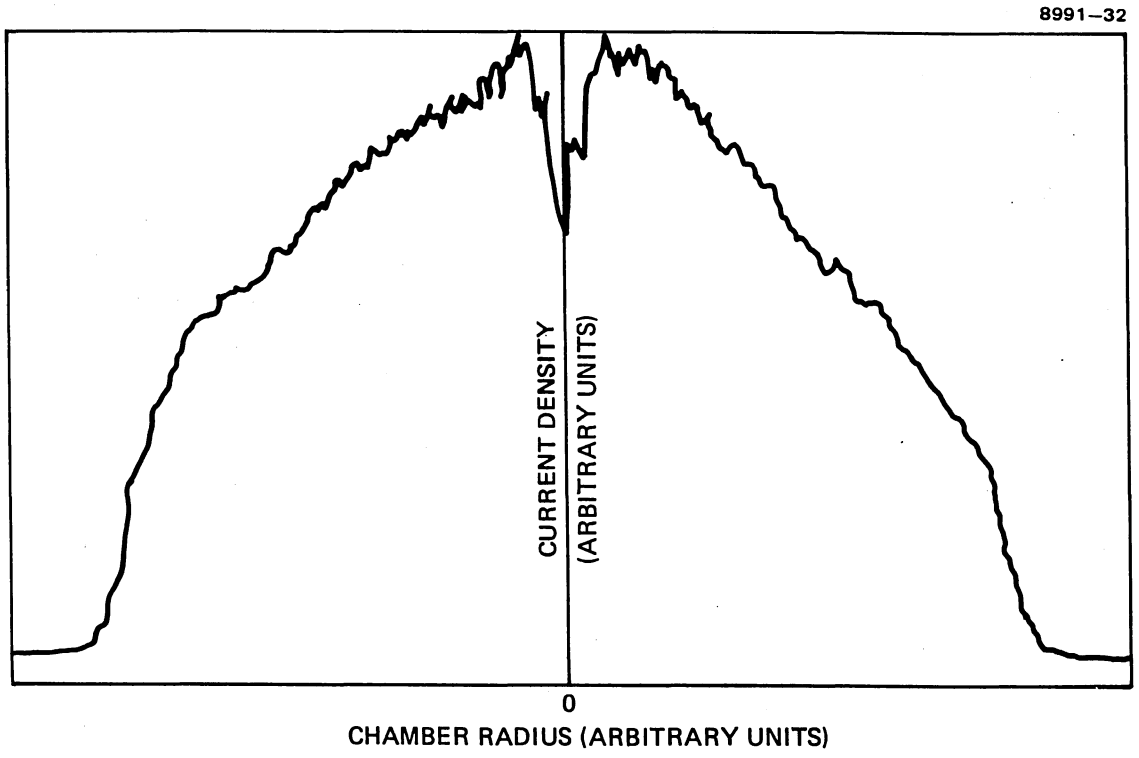

(a) Divergent magnetic-field configuration

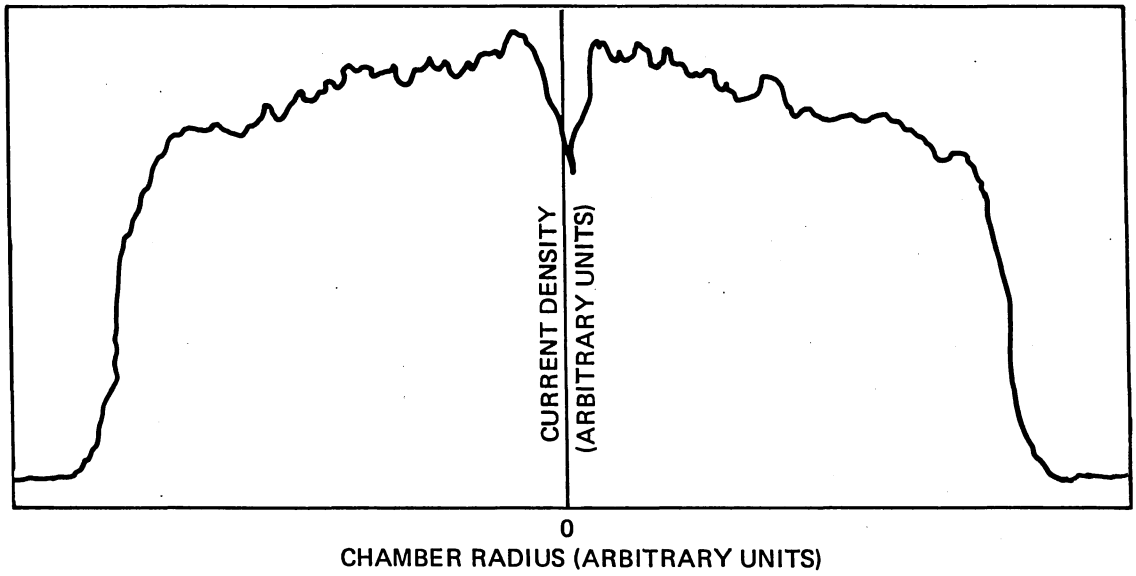

(b) Single-cusp magnetic-field configuration

Figure 2-30. Comparison of the beam current profile of the Hughes 30-cm experimental thruster operated with divergent and single-cusp magnetic-field geometries.

Table 2-3, it appears that the screen-grid erosion on the centerline of the 30-cm thruster can be reduced by approximately a factor of two through the use of the single-cusp-magnetic-field discharge-chamber design.

b. Anode Geometry

The feasibility of increasing the residence time of neutrals in the vicinity of the chamber wall was investigated using an anode geometry that was designed to minimize the probability that atoms liberated from this surface would be directed toward the chamber axis. In arriving at the anode gometry, we assumed that the neutral flux from the surface of this electrode was diffuse due to surface irregularities and that the anode curvature could be neglected. Under these assumptions, the distribution of particle flux $\Gamma(\theta)$ from a small area of the conventional anode design is primarily normal to the surface, as indicated in Figure 2-31(a). As a result, most atoms travel directly toward the axis of the chamber on being liberated. However, by suitable arrangement of the anode surface it should be possible to direct the particle flux toward the boundary, rather than the axis, resulting in an increase in the residence time of neutrals in the region close to the chamber wall. This idea is illustrated in Figure 2-31(b). The analogy between the neutral particle flux and heat transfer from diffusely radiating surfaces permits design criteria for the wavy-surface geometry to be established using geometric-shape-factor analysis. The geometry of Figure 2-31(b) is equivalent to a configuration commonly encountered in radiant-heat-transfer calculations, consisting of two rectangles with one common edge and an included angle between the planes, as illustrated in Figure 2-32. Using this analogy, the design problem becomes one of choosing the quantities a and ϕ shown in Figure 2-32 such that the shape factor F_{12} describing the fraction of the flux leaving surface 1 and arriving at surface 2 is a maximum. The shape factor is found to be a maximum for small values of the angle ϕ and the nondimensional height a/ℓ. The shape factor lies in the range $0.70 \leq F_{12} \leq 0.74$ for an included

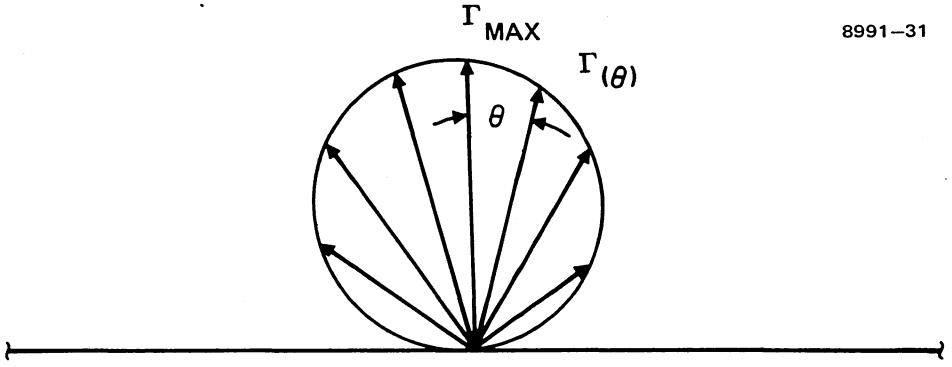

(a) Plane-surface geometry

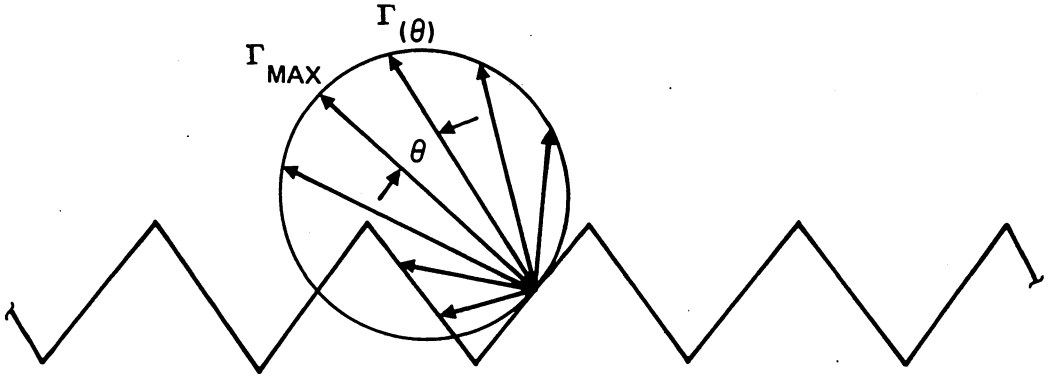

(b) Wavy-surface geometry

Figure 2-31. Geometry used in shape-factor analysis of wavy-surface geometries.

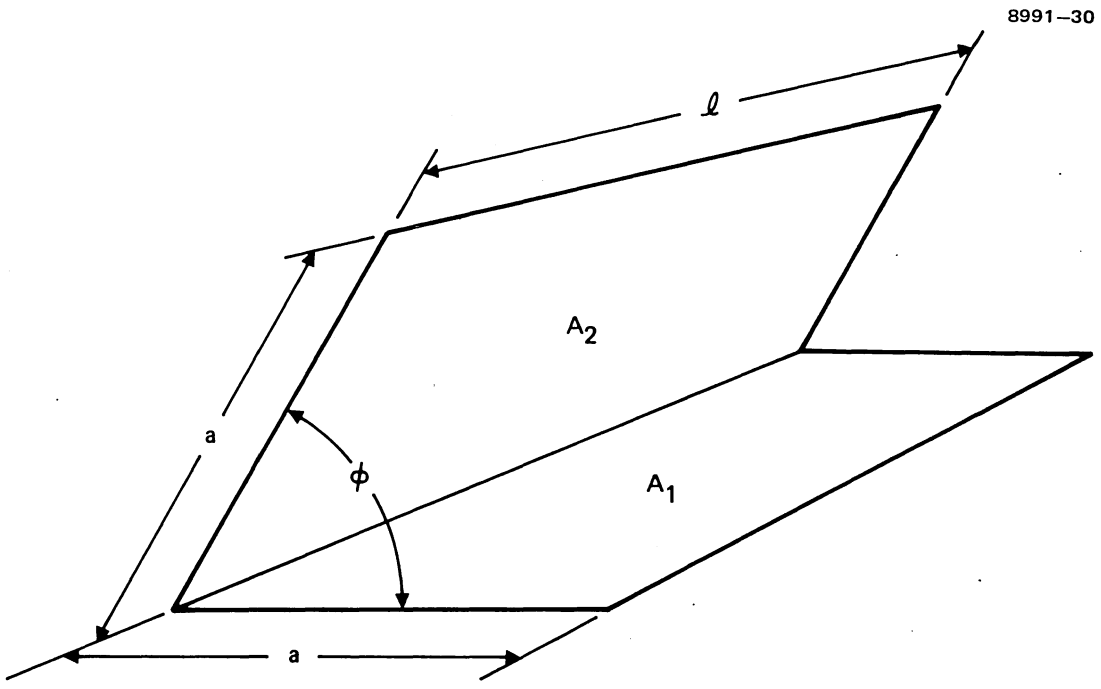

Figure 2-32. Geometry used in shape-factor analysis of wavy-surface anode design.

angle of $\phi = 30°$ and a nondimensional height in the range $0.4 \geq a/\ell \geq 0.1$. Based on these results and practical fabrication considerations, design values of $\phi = 30°$ and $a/\ell = 0.1$ were chosen. An anode liner having these dimensions was fabricated from thin stainless-steel shim stock and installed in the Hughes experimental (divergent field) thruster. The photograph of the discharge chamber given in Figure 2-33 illustrates the anode-liner installation.

The beam-current-density distributions for this thruster are compared in Figure 2-34 for operation with and without the anode liner. This comparison indicates that the attempt to modify the neutral-density profile did not improve the plasma-density distribution. Although somewhat disappointing, these results are consistent with and support the concept of a critical magnetic-field line and the theory that changes made external to the plasma region defined by this boundary have essentially no effect on plasma-density distribution or chamber performance.

D. MODEL OF EROSION PROCESSES

The potential mission applications of the 30-cm thruster would require a lifetime in excess of 10,000 hr. The lifetime design goal of the J-series thruster is 15,000 hr, and the projected lifetime (based on a 937-hr endurance test) is over 25,000 hr, assuming that useful lifetime is determined by the maximum sputter-erosion rate of the screen electrode. A model for predicting the wearout lifetime of the LeRC/Hughes 30-cm thruster would complement the existing thruster performance model (given in Ref. 2-1) and the cathode and propellant-electrical-isolator models (presented in Sections 3 and 5). A model of wearout lifetime would also be useful in the design of extended-performance thrusters capable of high-thrust, long-life operation. Based on the principles of physical sputtering, we know a priori that the chamber wear rates are determined by the type of material; the energy, arrival rate, angle of incidence, and identity of the plasma ions; and the degree of surface contamination. Thus, we can at the outset identify the critical thruster operating parameters as discharge voltage, beam current, and propellant utilization, since these variables specify the ion

8991—35

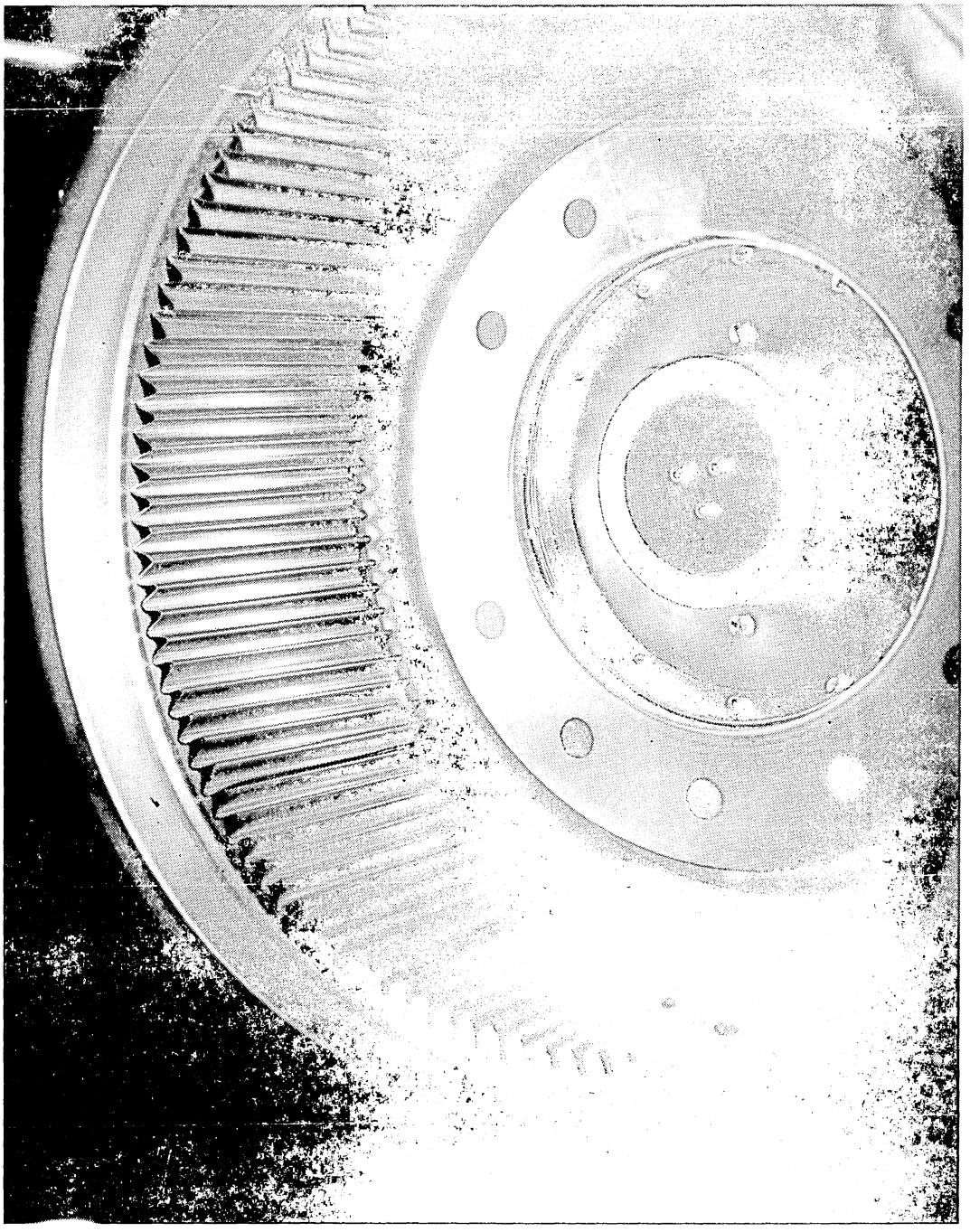

Figure 2-33. Photograph of anode-liner installation in the Hughes experimental divergent-field thruster.

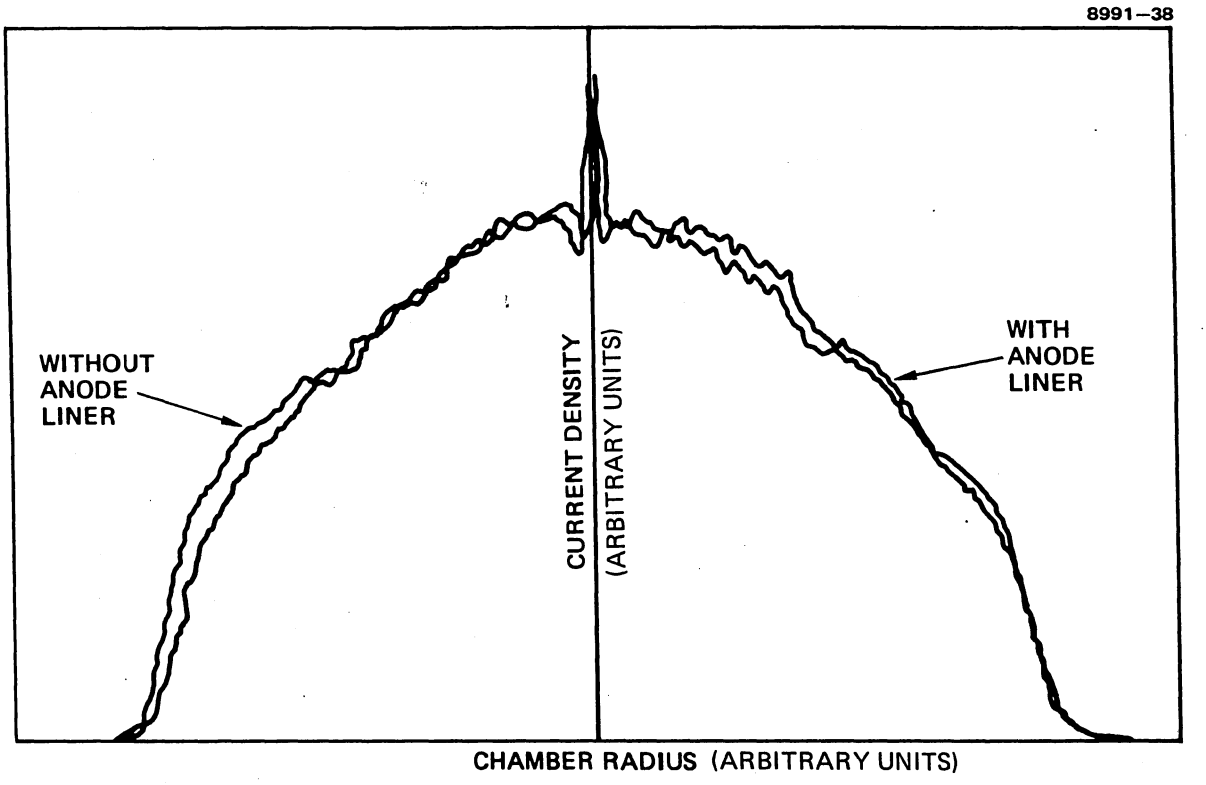

Figure 2-34. Beam current profiles obtained with and without the anode liner shown in Figure 2-33.

energies and arrival rates and the relative concentration of multiply charged plasma ions. Likewise, the most important chamber-desigh parameters can be identified as (1) the magnetic-field geometry (which determines the plasma-density distribution), (2) the choice of materials (which determines the sputter yields), and (3) the open area of the screen and accelerator electrodes (which determines the ion and neutral densities required to satisfy the beam current and propellant-utilization requirements). Finally, to simulate the surface wear rates that will be encountered in space, the pressures in ground-based vacuum test chambers must be maintained at sufficiently low levels to prevent the formation of surface compounds that sputter at rates different from those of the pure metals.

By associating the fundamental factors that control physical sputtering with thruster design and operating parameters and with test-facility requirements, a qualitative model of thruster lifetime has been formulated that identifies all the variables involved. Although this model is useful in an academic sense, it does not provide the analytic description necessary to assess the relative importance of these variables in determining wearout lifetime. Such an analytic description is formulated below.

1. Physical Sputtering

The following assumptions were made in formulating a model of surface sputtering applicable to the discharge environment of the 30-cm thruster:

- Sputtering occurs as a result of momentum transfer between the incoming ions and the surface atoms of the material
- The ion pre-sheath velocities are negligible. Therefore, (1) the ion energies are determined by the product of their charge and the potential drop across the plasma sheath and (2) their angle of incidence is normal to the surface

- The sputter yield of a given material is a function of ion energy only and is independent of the flux and charge of the incident ions
- The gas pressure is sufficiently low to result in collisionless flow of the sputtered material away from the target
- Impurity or residual-gas effects are negligible, and clean-metal sputter yields are valid (this assumption is modified in Section 2.D.4).

Based on these assumptions, the sputtering rate W can be expressed in terms of the incident ion current density j and the surface sputtering yield S by the expression

$$W = \frac{1}{qn} \sum_i \frac{j_i S(i\phi_p)}{i} , \qquad (2.16)$$

where n is the density of the target material, q is the electronic charge, ϕ_p is the plasma potential, and the summation is over all ionization levels. Measurements of the fraction of multiply charged ions in the extracted beam of the 30-cm thruster have shown that the primary constituents are singly and doubly charged ions. Therefore, Eq. 2.16 can be simplified and written as

$$W = \frac{j}{2qn} \left[\frac{2S(\phi_p) + JS(2\phi_p)}{1 + J} \right] , \qquad (2.17)$$

where J is the ratio of the doubly to singly charged ion current densities, and j is their sum. Eq. 2.17 relates the sputter erosion rate of surfaces within the discharge chamber to the local values of the plasma properties ϕ_p, j, and J under the assumptions stated earlier.

2. Qualitative Model of Chamber Erosion

A qualitative model of wearout lifetime can be formulated by identifying the dependence of each term in Eq. 2.17 on the thruster design and operating parameters and on the materials used in fabricating critical discharge-chamber components. The model formulated in this manner

is summarized in Table 2-8, which lists the variables appearing in the sputtering equation and identifies the dependence of each parameter on the thruster design, operational, and material characteristics. For example, Table 2-8 shows that the total current density j is determined by the thruster operating parameters of beam current and total accelerating voltage (effective screen-grid transparency), and by the designs of the magnetic-field geometry and screen electrode. The sputter yield S, on the other hand, is specified by the discharge voltage (plasma potential) and choice of material.

Table 2-8. Parameters Appearing in the Sputter-Yield Equation and Their Dependence on Thruster Operating, Design, and Material Characteristics

Parameter	Thruster Characteristic		
	Operation	Design	Material
j	Beam current Total accelerating voltage	Screen open area Magnetic-field geometry	——
J	Beam current Propellant utilization Discharge voltage	Magnetic-field geometry Accel open area Chamber volume-to-area ratio	——
S	Discharge voltage	———	Material property
n	———	———	Material property

3. Lifetime Model

The erosion of the screen electrode is of primary interest, since this component is thought to determine the lifetime of the 30-cm thruster. The erosion of other chamber surfaces (such as the baffle) may be comparable, but these surfaces are amenable to surface treatments (such as cladding with low-sputter-yield materials). But the screen grid must be thin to achieve good chamber performance and to satisfy specific-impulse requirements. An expression for screen-grid wear rate W_s can be obtained from Eq. 2.17 by introducing the ion-beam current density j_b and the effective transparency of the screen electrode, ϕ_s:

$$W_s = \frac{j_b}{2qn\phi_s} \left[\frac{2S(\phi_p) + JS(2\phi_p)}{1 + J} \right] . \tag{2.18}$$

Maximum screen-grid erosion occurs at the center of the electrode, since the ion current densities are at a maximum there. For screen-grid wear on centerline, Eq. 2.18 becomes

$$W_o = \frac{J_b}{2qnF\phi_s A_b} \left[\frac{2S(\phi_p) + J_o S(2\phi_p)}{1 + J_o} \right] , \tag{2.19}$$

where F is the beam flatness parameter, J_b is the beam current, A_b is the beam area, and the subscript o denotes values on centerline. Analytic expressions derived from measurements obtained with the 30-cm thruster of ϕ_s and ϕ_p were presented earlier, but are repeated here for convenience:

$$\phi_p = 1.28\ V_D - 9.38 \tag{2.20}$$

$$\phi_s = 0.781 + 0.084\ V_T - 0.062\ J_b . \tag{2.21}$$

Also, the sputter yield of many materials was shown to be given by the expression

$$S(\phi_p) = Ae^{B\phi_p} , \tag{2.22}$$

where the constants A and B and the density n are presented in Table 2-7. For a given chamber design (which specifies the parameters A, B, F, and A_b of Eqs. 2.19 and 2.22), the wear rate can be written as a function of the variables V_D, J_b, $\mathcal{J}_o$, and V_T, by using the parametric relationships given by Eqs. 2.20, 2.21, and 2.22. The number of variables can be reduced to three* by introducing the perveance relationship:

$$V_T = \left(\frac{J_b}{P}\right)^{2/3} , \tag{2.23}$$

where the measured perveance of the 30-cm thruster is

$$P = 4.8 \times 10^{-5} AV^{-3/2} . \tag{2.24}$$

Substituting the 30-cm thruster values of $A_b = 573\ cm^2$ and F = 0.5 into Eq. 2.19 results in the following equation for maximum wear rate in units of nm/hr:

$$W_o = \frac{3.92 \times 10^{26} J_b}{n\phi_s} \left[\frac{2S(\phi_p) + \mathcal{J}_o S(2\phi_p)}{1 + \mathcal{J}_o}\right] . \tag{2.25}$$

Defining the screen-grid lifetime L as the time required to erode 90% of the electrode thickness t_s results in the following relationship for lifetime:

$$L = \frac{342{,}900}{W_o} , \tag{2.26}$$

where the 30-cm-thruster screen-electrode thickness of t_s = 0.38 mm (0.015 in.) has been used.

---

*The variable $\mathcal{J}_o$ could be eliminated if sufficient parameter-variation data were available to express $\mathcal{J}_o$ in terms of V_D and J_b. However, since $\mathcal{J}_o$ also depends on the propellant utilization efficiency η_u, the number of independent vatiables is still three

The validity of the lifetime model can be demonstrated by comparing calculated erosion rates with experimental results obtained from endurance tests[2-4] of the 900- and J-series-equivalent thrusters. This comparison, presented in Table 2-9, shows that the calculated and measured values are in good agreement.

The model of thruster lifetime formulated earlier can be used with confidence to calculate erosion rates as a function of the variables J_b, V_D, and J_o. Results of these calculations are presented for molybdenum in Figures 2-35 and 2-36, which illustrate the sensitivity of screen-grid lifetime to the indicated parameters. For example, Figure 2-35 shows that for a lifetime goal of 15,000 hr the maximum beam current can be increased from 1.5 A to 5 A by reducing the discharge voltage from 36 V to 28 V. The combined results of Figures 2-35 and 2-36 show that for a given beam current the lifetime can be increased by reducing either the discharge voltage or the doubly charged ion concentration, with discharge voltage being the most sensitive parameter. Figure 2-37 presents the results of lifetime calculations for molybdenum, niobium, and tantalum, and shows that substantial gains in lifetime may be possible if the screen electrode can be fabricated from niobium rather than molybdenum. The results given in Figure 2-37 show, for example, that, at a 2-A beam current, a niobium screen electrode should last nearly 10,000 hr longer than the presently used molybdenum electrode.

Because of the inverse relationship between lifetime and beam current (which is evident in Eqs. 2.19 and 2.26), to achieve the goals for the extended-performance thruster of 15,000-hr lifetime at 6-A beam current will require reducing the discharge voltage and the ratio of doubly charged to singly charged ion densities; it may also require using materials that have sputter yields less than those of molybdenum. The screen-grid erosion model predicts a linear relationship between lifetime and the beam flatness parameter, suggesting that advanced discharge chamber designs that employ single-cusp or multipole magnetic-field geometries will be necessary to achieve these lifetime and beam-current goals.

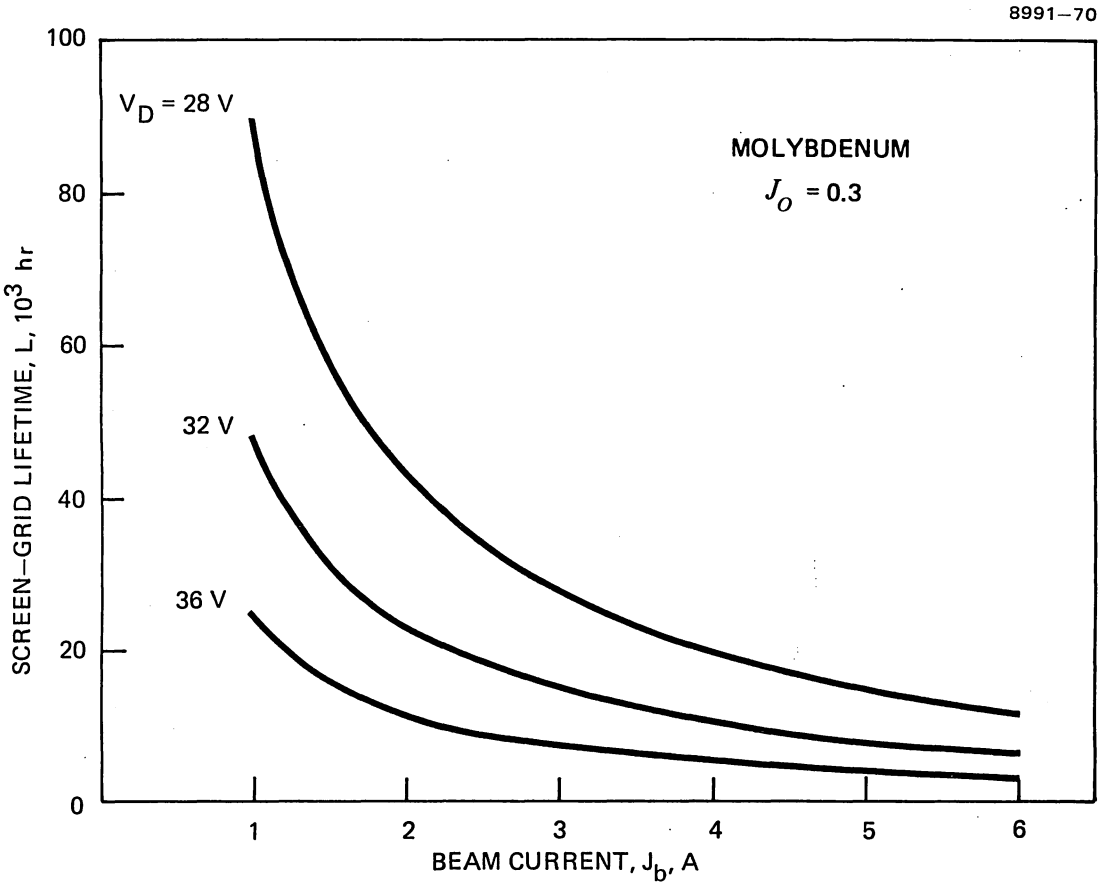

Figure 2-35. Sensitivity of screen-grid lifetime to discharge voltage, V_D.

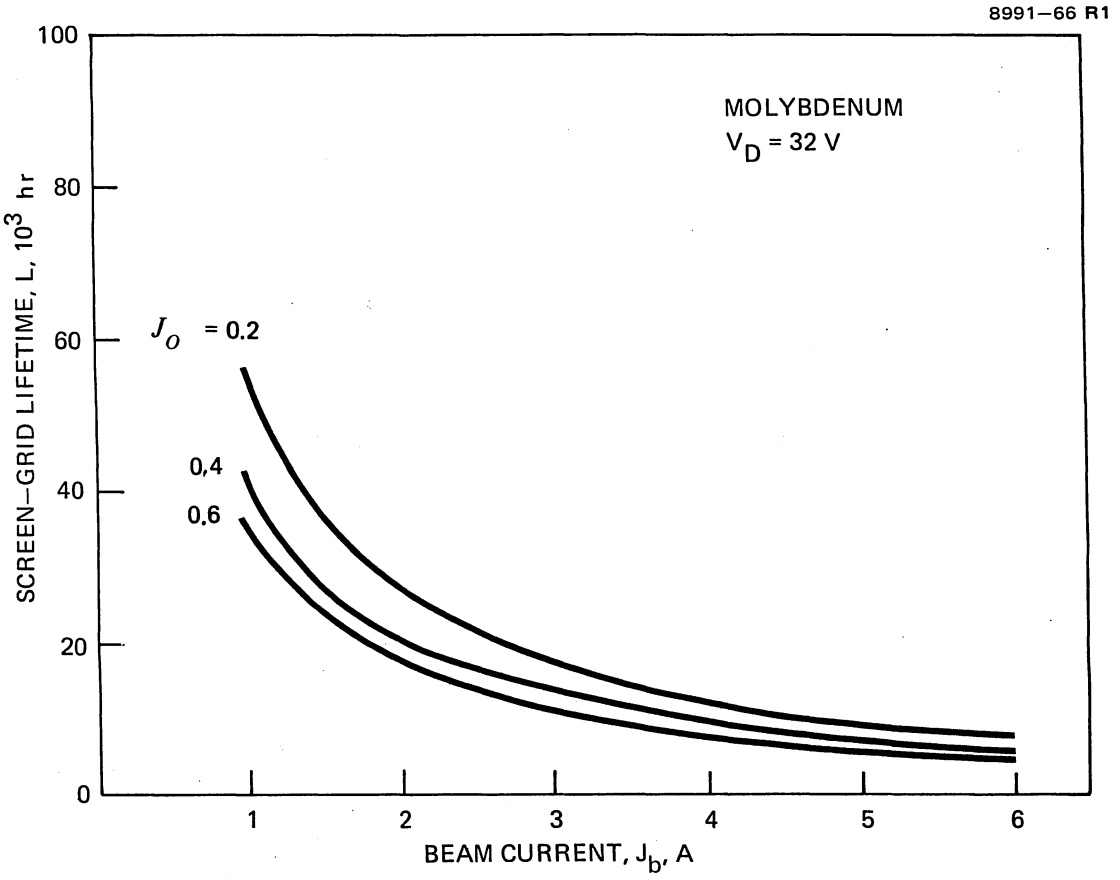

Figure 2-36. Sensitivity of screen-grid lifetime to the ratio of doubly to singly charged ion current densities, J_o.

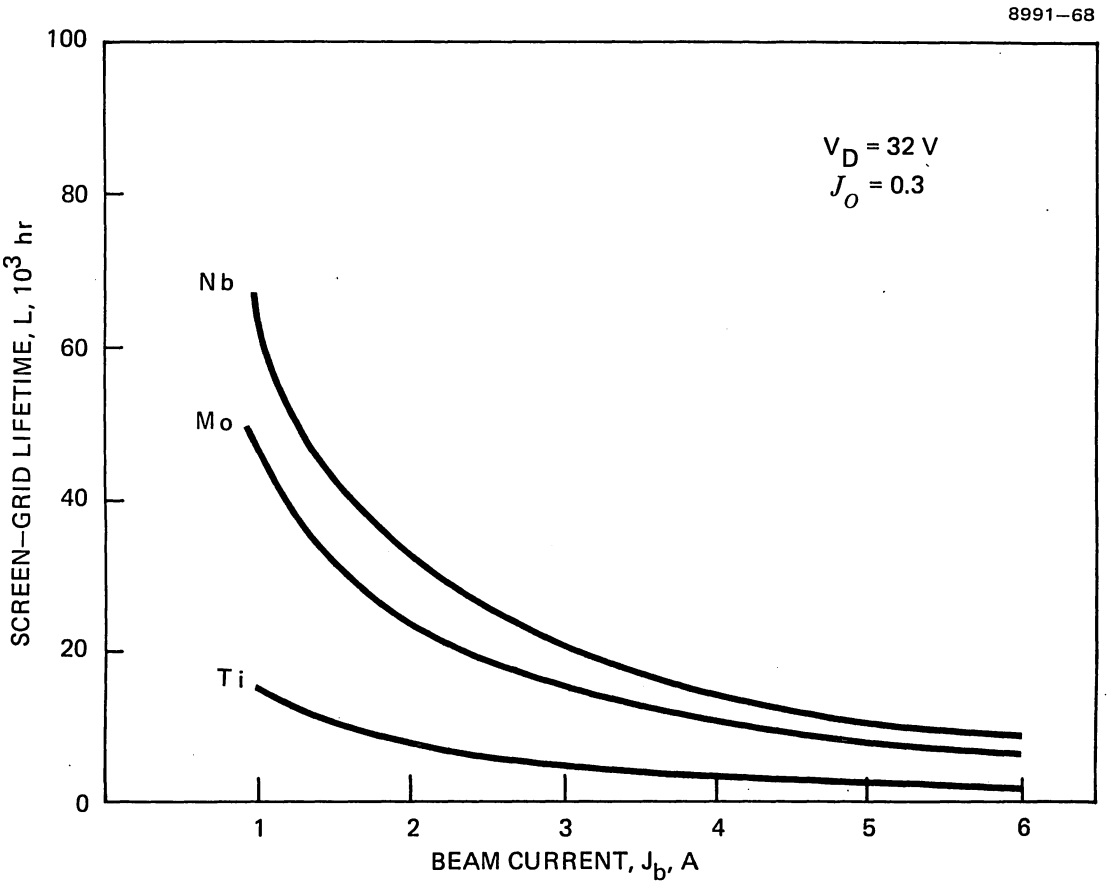

Figure 2-37. Sensitivity of screen-grid lifetime to choice of material.

Table 2-9. Comparison of Calculated and Measured Screen-Grid Erosion Rates

Thruster Series	V_D, V	V_T, kV	J_o [a]	Screen-Grid Erosion Rate, nm/hr	
				Calculated	Measured
900	36	1.6	0.45	33.4	33.0
J(equivalent)	32	1.4	0.26	13.6	12.9

[a] From Table 2-3.

6758

4. Residual Gas Effects

The presence of reactive residual gases can reduce the sputtering yield of metals (such as molybdenum) by forming a surface compound that has a lower sputter yield than the base metal. This phenomenon, which results from the chemisorption of chemically active atoms and ions (such as N and N^+) onto the surfaces of certain metals, has been observed by several investigators.[2-9 through 2-16] The model presented below was formulated to describe similar effects of reactive residual gases on the erosion rate of the screen electrode of the 30-cm thruster.

At very low residual-gas partial pressures, the arrival rate of impurity gas at a surface is small, and the sputtering rate is essentially that of the base metal. As the residual gas pressure is increased, the arrival rate of the impurity gas increases, and the surface coverage becomes significant. The flux of impurity gas contains chemically active atoms, ions, and molecules such as N, N^+, and N_2^+ that are produced as a result of bombardment by energetic plasma electrons. Under these conditions, a surface compound of the base metal (such as Mo_2N) can be formed by chemisorption. In the presence of the reactive residual gases, the sputtering rate W at a partial pressure p of reactive gas is related to the sputtering rates of the base metal W_{base} and the compound W_{comp} by the expression:[2-9]

$$f(p) = \frac{W(p) - W_{comp}}{W_{base} - W_{comp}} = \frac{1}{1 + (\alpha/\beta)(p/p_o)^n \Gamma(p)} , \quad (2.27)$$

where f(p) is the normalized erosion rate, $\alpha(p/p_o)^n$ is related to the sticking probability, p_o is the saturation pressure[2-20] at which the sputtering rate begins to rapidly decrease, n is the order of the reaction, $\Gamma(p)$ is the incdent flux of reactive gas atoms, and β is the rate of evaporation of residual-gas atoms from a completely covered surface.

The model of the effects of residual gas on surface erosion rates has been verified by other investigators,[2-9,2-16] who have shown a pressure-dependent sputtering rate that is described by the function f of Eq. 2.27 for nitrogen and oxygen gas in the presence of various metals such as molybdenum and titanium. The validity of the model in describing the effects of facility residual gases on the erosion rate of the screen electrode of the 30-cm thruster was demonstrated by using Eq. 2.27 to normalize the centerline erosion-rate measurements of Table 2-5 and then curve fitting these data to a function of the form:

$$f(p) = (1 + ap^b)^{-1} , \quad (2.28)$$

where a and b are constants determined by the curve fit. These results are presented in Figure 2-38, which shows the normalized erosion rates and the function derived by fitting these data to Eq. 2-28. The agreement evident in Figure 2-38 and the similarity of the curve defined by the normalized sputtering-rate function and the line-intensity measurements of Figures 2-19 to 2-23 indicate that the model of residual gas effects presented earlier adequately describes the pressure-dependent sputtering observed in the 30-cm thruster.

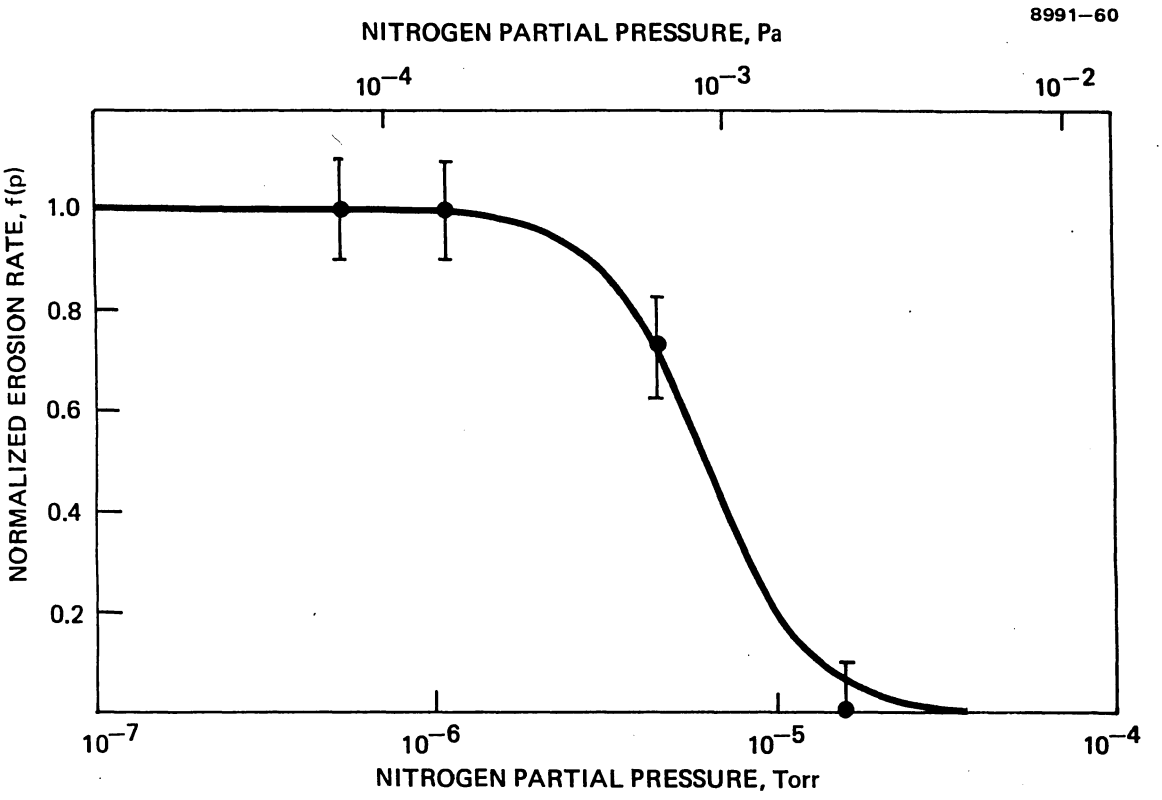

Figure 2-38. Variation of the normalized sputtering-rate function with the partial pressure of nitrogen; comparison of experimental values and curve-fit based on the model. The curve-fit is described by $f(p) = (1 + 3.6 \times 10^{14}\ p^{2.8})^{-1}$ for the pressure p in Torr.

Page intentionally left blank

REFERENCES FOR SECTION 2

2-1. R.L. Poeschel and E.I. Hawthorne et al., "Extended Performance Solar Electric Propulsion Thrust System Study," NASA CR-135281, Hughes Aircraft Company, September 1977.

2-2. R.L. Poeschel, et al., "High-Power and 2.5 kW Advanced-Technology Ion Thruster," NASA CR-135163, Hughes Research Laboratories, Feburary 1977.

2-3. W.S. Williamson and J. Hyman, Jr., "Discharge-Chamber Sputtering Investigation," AIAA Paper No. 76-1019, Key Biscayne, Florida, November 1976.

2-4. V.K. Rawlin and M.A. Mantenieks, "Effect of Facility Background Gases on Internal Erosion of the 30-cm Hg Ion Thruster," AIAA Paper No1 78-665, San Diego, California, April 1978.

2-5. G.R. Harrison, "M.I.T. Wavelength Tables," The M.I.T. Press, Cambridge, Massachusetts, 1969.

2-6. H. Kayser and R. Ritschl, "Tabelle der Hauptlinien der Linienspektren aller Elemente," Springer-Verlag, New York, 1968.

2-7. R.L. Summers, "Empirical Observations on the Sensitivity of Hot Cathode Ionization Type Vacuum Gages," NASA TN D-5285, June 1969.

2-8. R.L. Poeschel et al., "2.5 kW Advanced Technology Ion Thruster," NASA CR-134687, Hughes Research Laboratories, August 1974.

2-9. T. Abe and T. Yamashina, "The Deposition Rate of Metallic Thin Films in the Reactive Sputtering Process," Thin Solid Films 30, 19, 1975.

2-10. J. Heller, "Reactive Sputtering of Metals in Oxidizing Atmospheres," Thin Solid Films 17, 1973, pp. 163-176.

2-11. K. Hayek, H.E. Farnsworth, and R.L. Park, "Interaction of Oxygen, Carbon Monoxide, and Nitrogen with (001) and (110) Faces of Molybdenum," Surface Science 10, 1968, pp. 429-445.

2-12. H.F. Winters and P. Sigmund, "Sputtering of Chemisorbed Gas (Nitrogen on Tungsten) by Low-Energy Ions," J. Appl. Phys. 45, 11, November 1974, pp. 4760-4766.

2-13. R.E. Jones, H.F. Winters, and L.I. Maissel, "Effect of Oxygen on the rf-Sputtering Rate of SiO_2," J. Vac. Source and Tech. 5, 3, 1968, pp. 84-87.

2-14. M. Cantagrel and M. Marchal, "Argon Ion Etching in a Reactive Gas," J. Mat. Sci. 8, 1973, pp. 1711-1716.

2-15. S. Nagata and F. Shoji, "Structure of Film Prepared by Low Energy Sputtering of Molybdenum," Japanese J. of Appl. Phys. 10, 1, January 1971, pp. 11-17.

2-16. R.N. Castellano, "Reactive Ion Beam Sputtering of Thin Films of Lead, Zierconium, and Titanium," Thin Solid Films 46, 1977, pp. 213-221.

2-17. G.R. Taylor and K.N. Leung, "Microcompuber Analysis of Multidipole Plasma Langmuir Probe Characteristics," Rev. Sci. Instrm. 47, 5, May 1976, pp. 614-616.

2-18. S.L.G. Askerov and L.A. Sena, "Cathode Sputtering of Metals by Slow Mercury Ions," Soviet Physics - Solid State 11, 6, Decmeber 1919, pp. 1288-1293.

2-19. J.R. Beattie and P.J. Wilbur, "Cusped Magnetic Field Mercury Ion Thruster," J. Spacecraft and Rockets, 14, 12, December 1977, pp. 747-755.

2-20. S. Brunauer, P.H.Emmett, and E. Teller, "Adsorption of Gases in Multimolecular Layers," J. Am. Chem. Soc. 60, February 1938, pp. 309-319.

SECTION 3

CATHODE LIFETIME

The objectives of this task were to identify the factors that limit hollow-cathode lifetime and to formulate a model for predicting cathode lifetime in terms of the principal life-limiting factors. The work described here builds on the results obtained under the preceding NASA contract (NAS 3-19703) and has succeeded in describing cathode lifetime limits within the postulated model for cathode emission processes. The hollow-cathode emission process itself was not a subject of investigation under this study; however, a brief description of a conceptual model of the physical process has been included here to support the discussion of the life-limiting factors.

A. CONCEPTUAL MODEL OF HOLLOW-CATHODE PROCESSES

The hollow-cathode configuration that was investigated is shown in Figure 3-1. This hollow-cathode is used as the electron source for the plasma-bridge neutralizer and the discharge chamber of the 30-cm mercury electron-bombardment ion thrusters under development at HRL and NASA LeRC. Hollow-cathode discharges have been a popular subject for investigation at several research centers and universities[3-1 through 3-5] for a number of years because of their unique operating characteristics, which defy precise analytic description. The two features that characterize this discharge and that are also essential to its application in ion-thruster technology are

- Emission current is comparable to but slightly in excess of temperature-limited thermionic emission.
- Very low discharge voltage, in some instances lower than the ionization potential of the gas used in the discharge.

These two properties are considered to be closely coupled and critical to operation of the cathode for long lifetime and high current. In the configuration shown in Figure 3-1, mercury vapor flows through the cathode tube, limited by the cathode orifice. With the impregnated

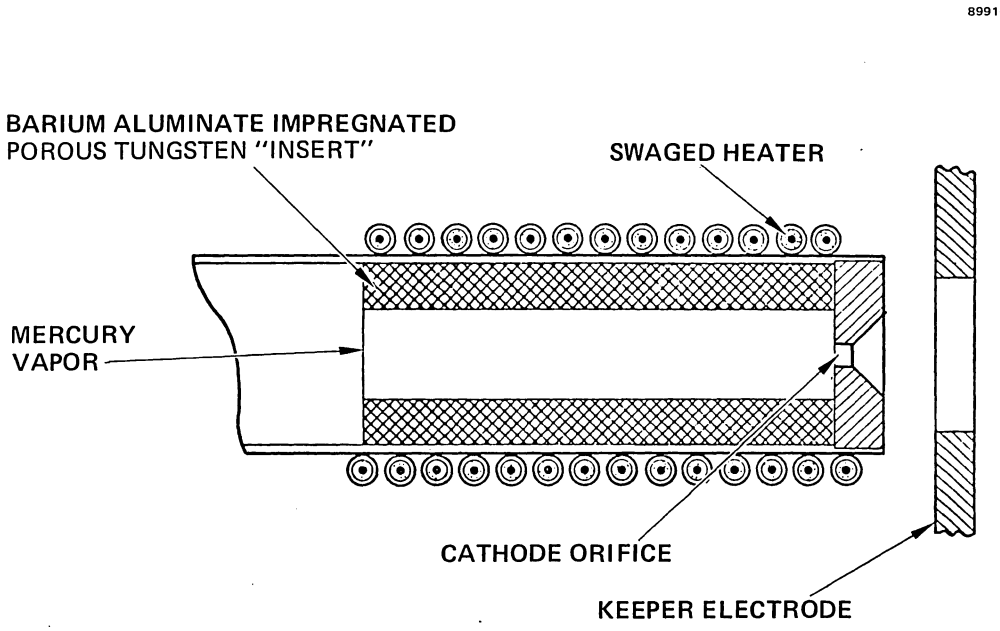

Figure 3-1. Hollow-cathode configuration representative of 30-cm-thruster technology.

porous-tungsten insert heated to about 1300°K, electrons are emitted from the insert surface into the plasma region of the hollow-cathode discharge and then collected at the keeper electrode (which is biased positive with respect to the cathode tube and orifice). After ignition, and under special mercury-vapor and cathode-emission conditions, discharge operation has been maintained with an applied keeper voltage of only 2 V (in mercury vapor). This suggests that the ionization process is comparable to the one studied by Martin and Rowe[3-6] and Salinger and Rowe[3-7] at the University of Michigan. They have shown quantitative support for the theory that ionization takes place predominantly as a result of the collision of excited atoms in the discharges of gas-filled, thermionic-emitter diodes that operate at low voltage. They also show support for the theory that excitation of gas atoms occurs by collision with electrons from the high-energy tail of the Maxwellian electron distribution. Consequently, the applied voltage can be less than the ionization potential and, in fact, even less than the lowest excitation potential. For operation using xenon and argon, Martin and Rowe also verified that there are no elevated potentials within the plasma region in discharges of this type and suggested that the same mode of operation would also be expected in mercury and alkali-plasma discharges.

After examining the conditions required to sustain such a low-voltage discharge, we conclude that the prime requirements are for (1) a high density of thermionic electrons to furnish the high-energy Maxwellian tail and (2) an adequate gas density to ensure frequent excitation collisions. In the hollow-cathode configuration under consideration, the gas density is satisfied by the gas flow and constricting orifice. The thermionic emission must be provided by an adequate low-work-function surface area obtained from barium/barium-oxide coverage of the porous-tungsten insert (also the cathode orifice and the cathode orifice plate). The basic assumptions in this investigation are that the cathode configuration has been developed to an extent that the conditions for achieving the low-voltage discharge mode described above have been met and that:

(i) Ions that are accelerated through the internal plasma potentials to strike insert and orifice surfaces gain insufficient energy to erode these surfaces by ion sputtering

(ii) Barium is supplied to the insert surface from the pores of the porous tungsten and is lost only through evaporation

(iii) The presence of propellant gas in the cathode interior does not influence the rate of barium evaporation

(iv) The effect of the presence of barium vapor above the porous-tungsten-insert surface on the evaporation rate is already accounted for in the measurement of barium loss-rate versus insert temperature performed under Contract NAS 3-19703

(v) Barium lost from the porous-tungsten insert is no longer available to participate in the emission processes.

The cathode operating conditions assumed above are only intended for examining macroscopic variations. For example, variations in plasma potentials, electron temperatures, neutral densities, etc. that do not violate condition (i) above are considered to be inconsequential unless barium depletion is grossly affected.

B. LIFE-LIMITING FACTORS

The one major requirement identified in the preceding discussion of hollow-cathode operation is that thermionic emission be maintained. This requirement has been assumed to be directly correlated with the barium coverage of the porous-tungsten, barium-aluminate-impregnated insert (reservoir for storing barium). The barium coverage is in turn a function of the insert temperature. Having determined the barium depletion rate during the preceding study (Contract NAS 3-19703), the task here was to determine those factors that affect the insert temperature under the anticipated operating conditions. The cathode operating parameters considered were

- Total emission current
- Cathode keeper current
- Cathode propellant flow rate
- Magnetic baffle current
- Discharge voltage.

In addition to operating parameters, the procedures used in the care and handling of thrusters were considered as factors that could possibly impair the lifetime of the cathode. Some of the factors examined were

- Cathode conditioning procedures
- Intentional operation at excessive temperatures
- Exposure to chemical vapors.

Other factors recognized as contributing to life limitation caused by barium depletion are

- The quantity of barium available within the insert
- Contamination that could clog the pores of the porous-tungsten material.

These factors were not investigated, primarily because they are not readily related to a single variable or set of parameters that can be quantified and controlled. Since the ultimate use of the information obtained was to formulate an analytic model for cathode lifetime, only the factors that could be measured quantitatively were explored in any depth.

C. MEASUREMENT TECHNIQUE

The major challenge under this task was to measure the temperature of the insert in an operating thruster in a way that did not appreciably change the cathode configuration or its thermal characteristics. Attaching thermocouples directly to the porous-tungsten insert was considered the most promising way of making the measurement, and specially fabricated encapsulated thermocouples were obtained. Figure 3-2(a) shows the normal porous-tungsten insert with its two electrical leads; Figure 3-2(b) shows the thermocouple-attachment configuration. The encapsulated thermocouples have a tantalum sheath, which was used as the electrical lead for the insert. The thermocouples were attached to the porous-tungsten insert by brazing, using a minimal amount of molybdenum-nickel braze material to bond the thermocouple sheath to the insert only in the vicinity of the sensor. The braze was made by locally heating the

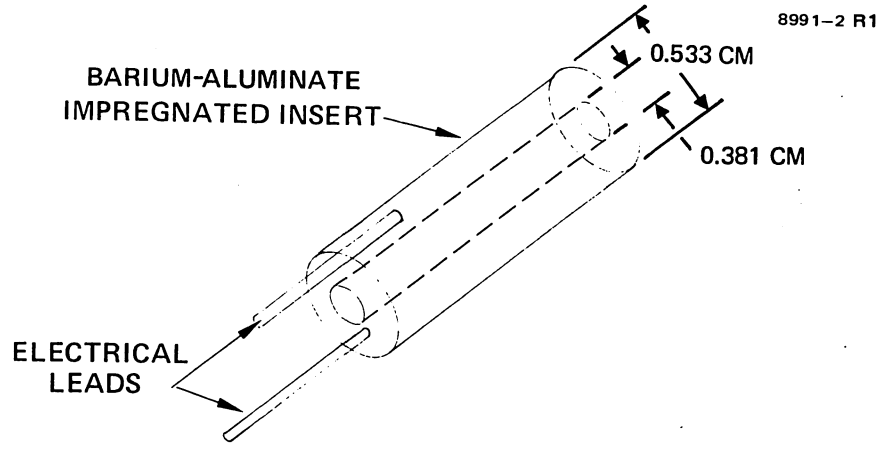

a) "STANDARD" POROUS-TUNGSTEN CATHODE INSERT

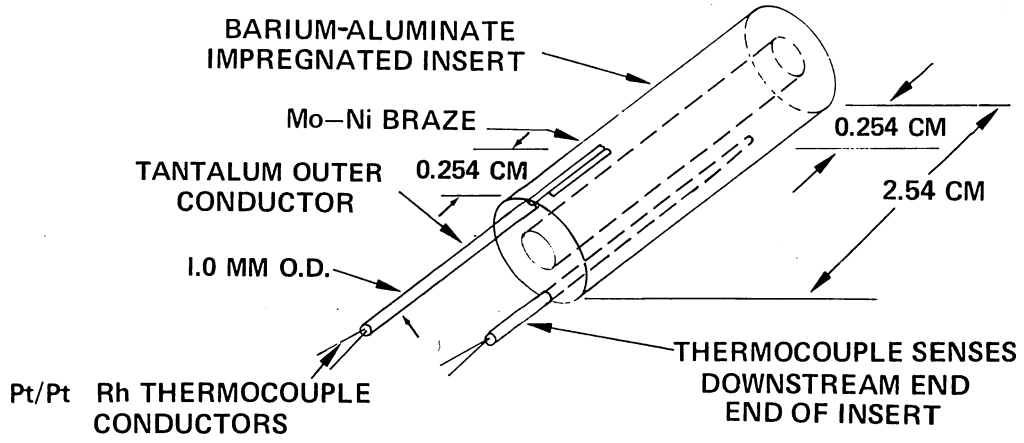

b) THERMOCOUPLE INSTRUMENTED INSERT

Figure 3-2. Comparison of standard and instrumented insert configurations.

thermocouple sheath and the barium-aluminate impregnated insert using an electron-beam welder. This technique was selected after first consulting with the manufacturers of the porous-tungsten insert and the thermocouple for maintaining both the thermocouple and the insert in good working condition.

The thermocouple itself was platinum/platinum-rhodium material with the sensor insulated from the sheath. The sensor has a 0.1-sec response time, which was more than adequate for the bridge circuit used to read temperatures. The thermocouples were installed on opposite sides of the insert cylinder as shown in Figure 3-2(b), and the sensors were located 0.254 cm from each end of the cylinder. The manner in which the thermocouple-instrumented insert assembly was installed in the thruster cathode is shown in Figure 3-3. Except for the flange that serves as the propellant inlet for the cathode, all of the cathode/cathode-pole-piece parts are "standard." Figure 3-4 shows a photograph of the assembly in place.

D. EXPERIMENTAL RESULTS

The experimental results are discussed here in decreasing order of significance (most significant first). Figure 3-5 shows that the insert temperature measured at both thermocouple locations (shown in the sketch included in Figure 3-5) increases linearly with cathode emission. Figure 3-6 shows that increasing the discharge voltage at a constant emission current also increases both insert temperatures; however, the increase is not really appreciable with respect to the absolute accuracy of the temperature measurement (as indicated by the error bars shown in the figure). In fact, the variation shown is really a consequence of increasing the discharge power, and insert temperature is inversely proportional to discharge voltage when discharge power is held constant (by decreasing emission current), as illustrated by Figure 3-7.

We had initially thought that cathode-keeper-discharge parameters would be very sensitive to insert temperature; however, as Figures 3-8 and 3-9 show, the variation is not very significant (with respect to the absolute accuracy of the measurement). Cathode keeper voltage shows the

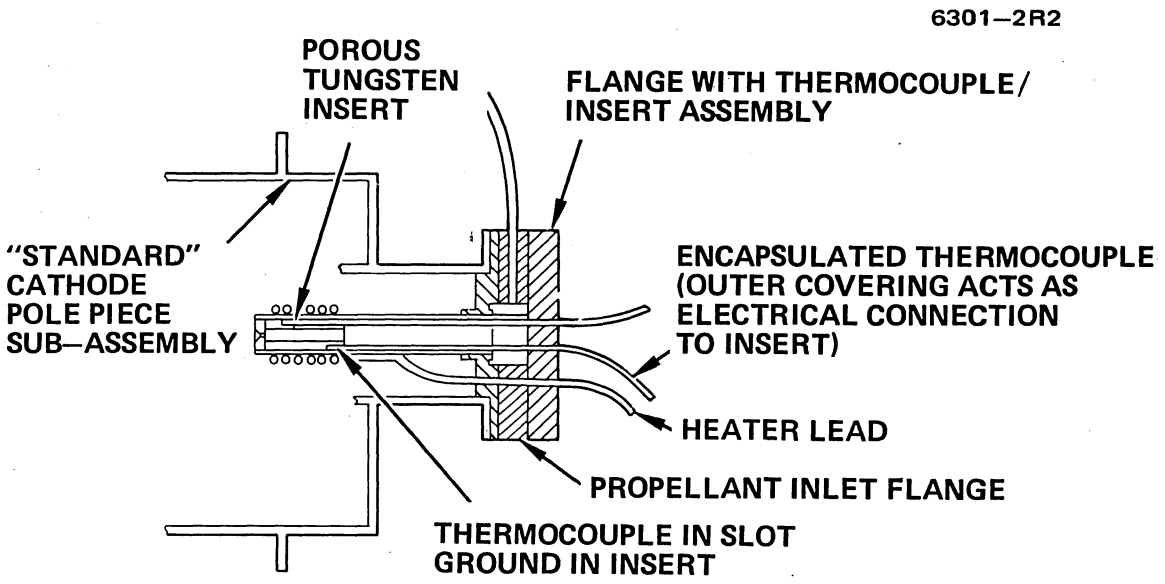

Figure 3-3. Cathode configuration of 800/900-series engineering-model thruster showing thermocopules for monitoring insert temperature.

M12568-1

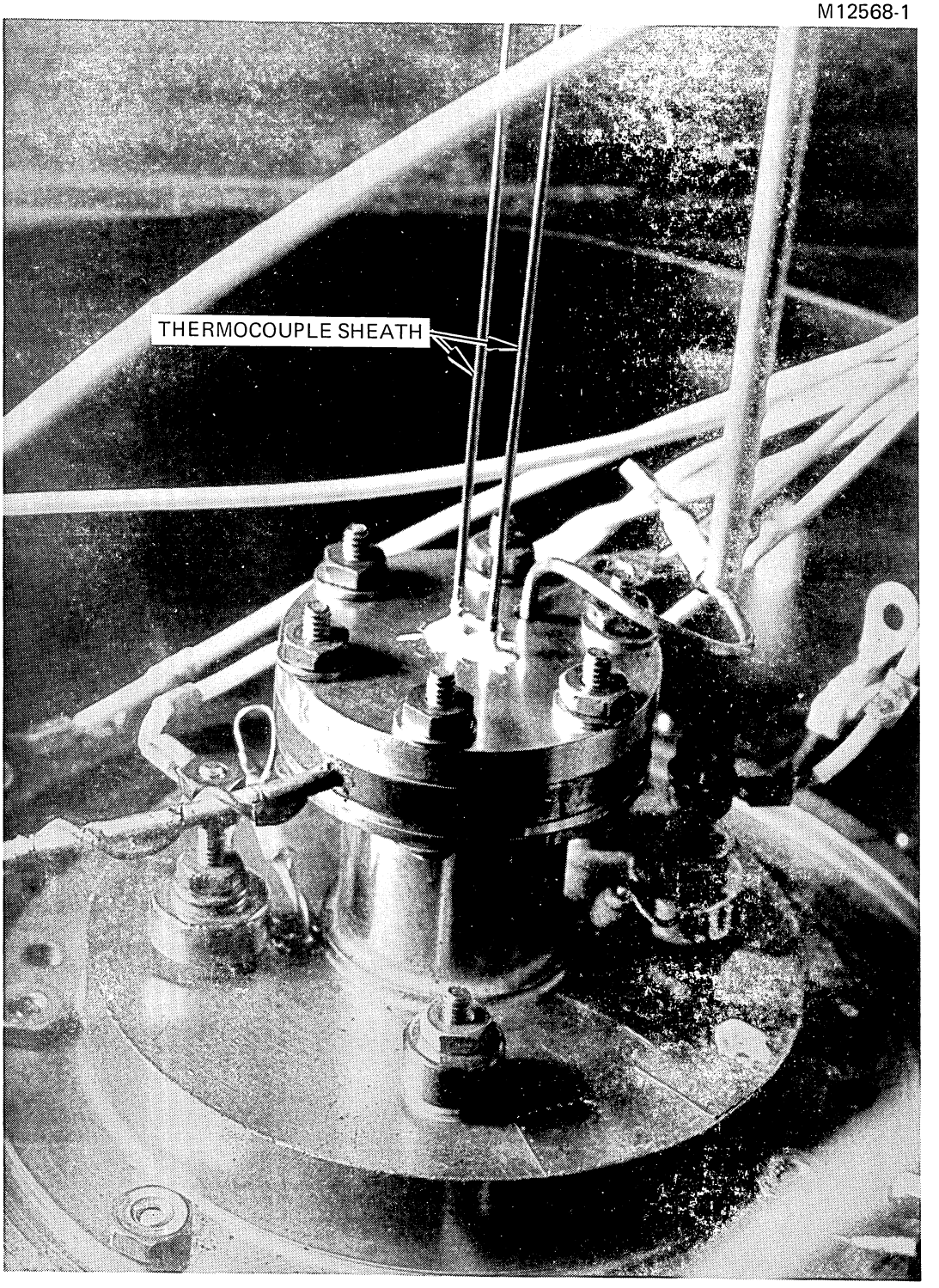

Figure 3-4. Photograph of cathode pole piece with instrumented cathode insert installed.

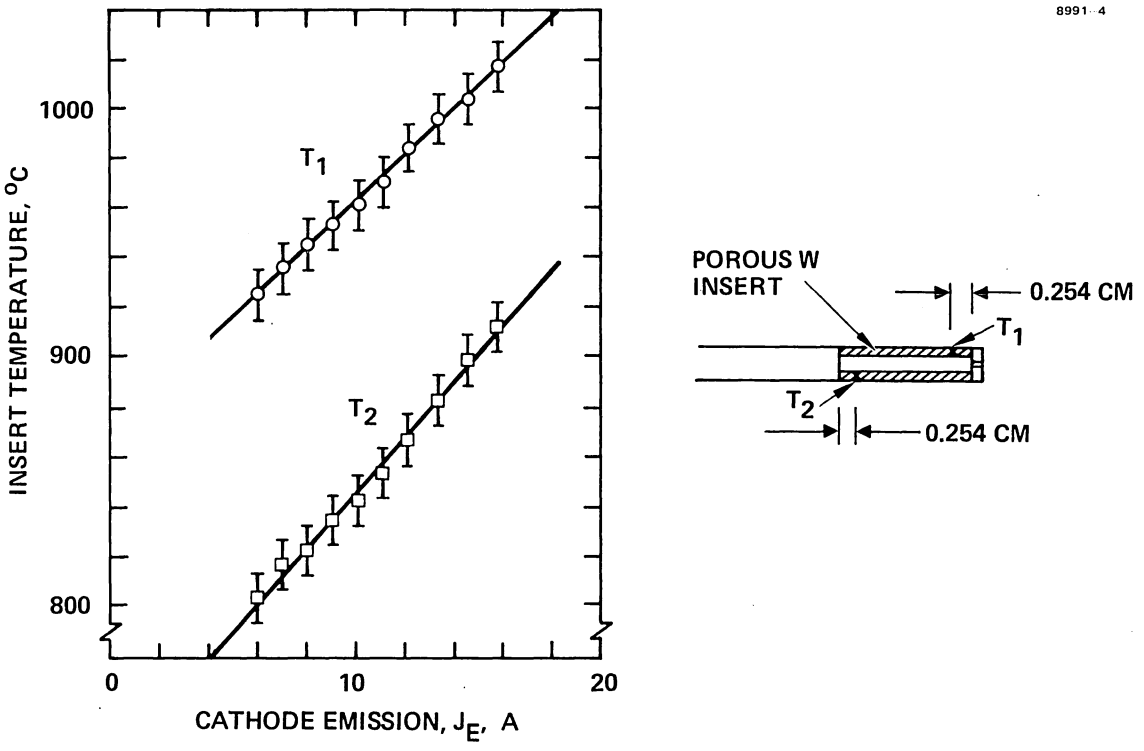

Figure 3-5. Variation of porous-tungsten insert temperature with cathode emission current J_E. (V_D = 32 V, J_b = 0.2 J_E - 0.4 A).

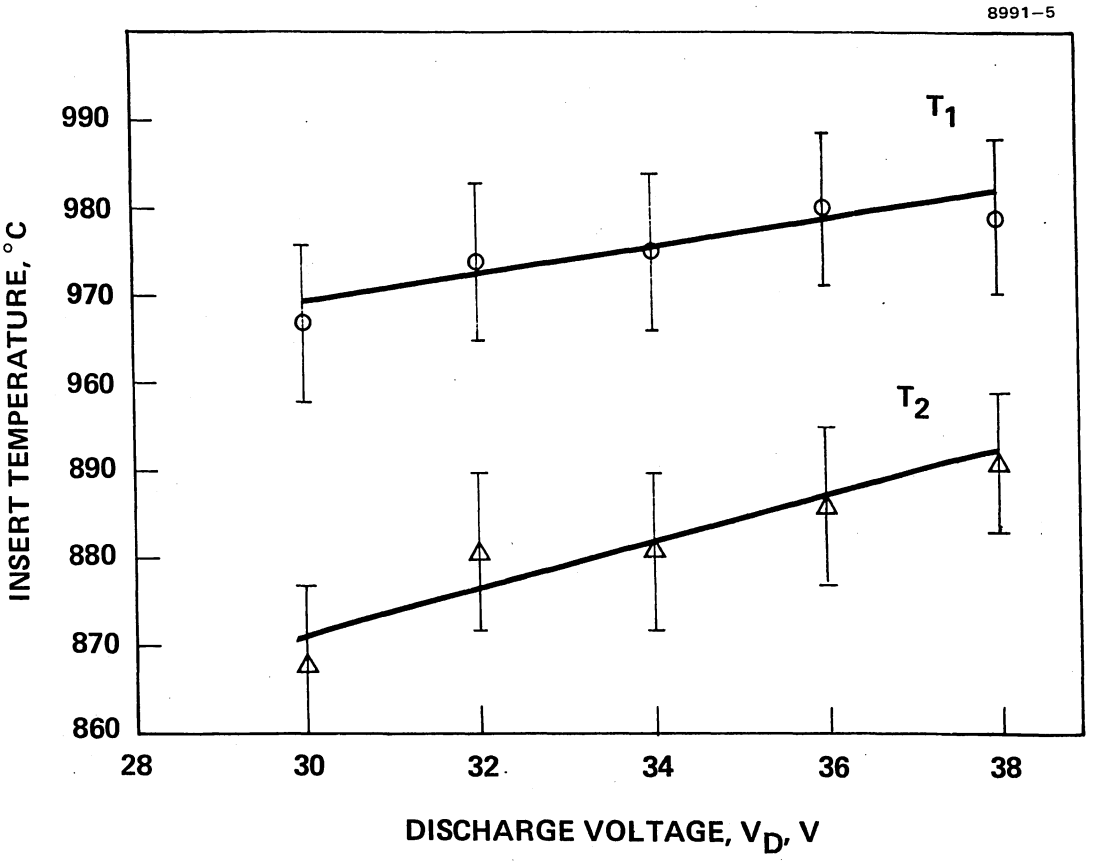

Figure 3-6. Variation of insert temperature with discharge voltage for constant emission current, J_E = 12 A.

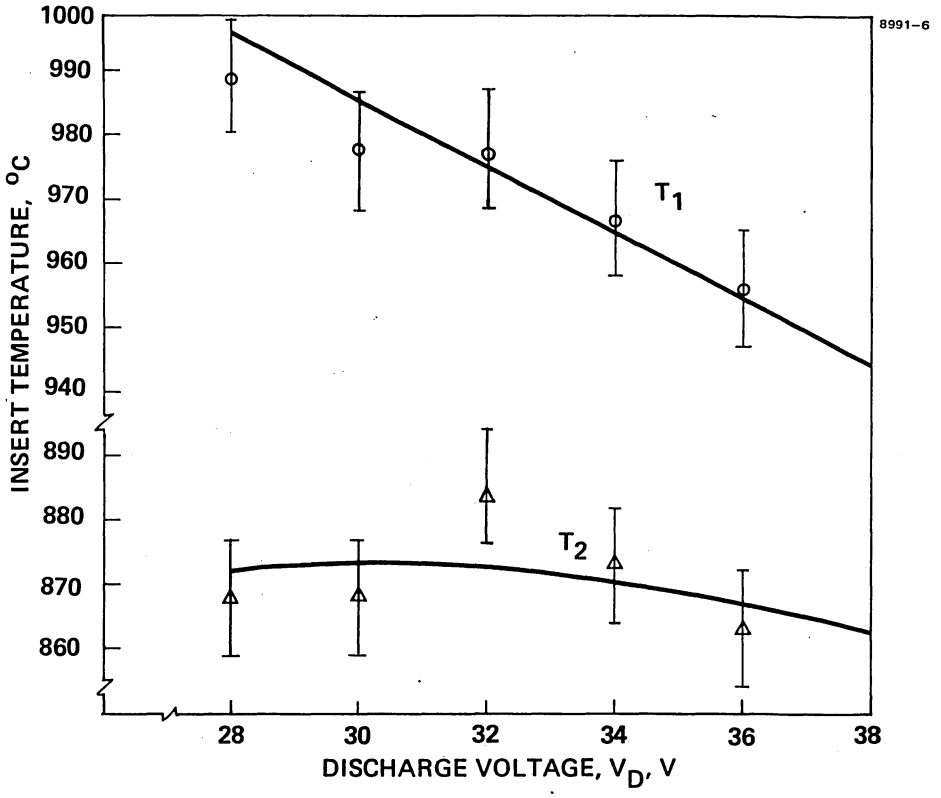

Figure 3-7. Variation of insert temperature with discharge voltage for constant discharge loss ε_i = 192 eV/ion and constant beam current J_b = 2 A.

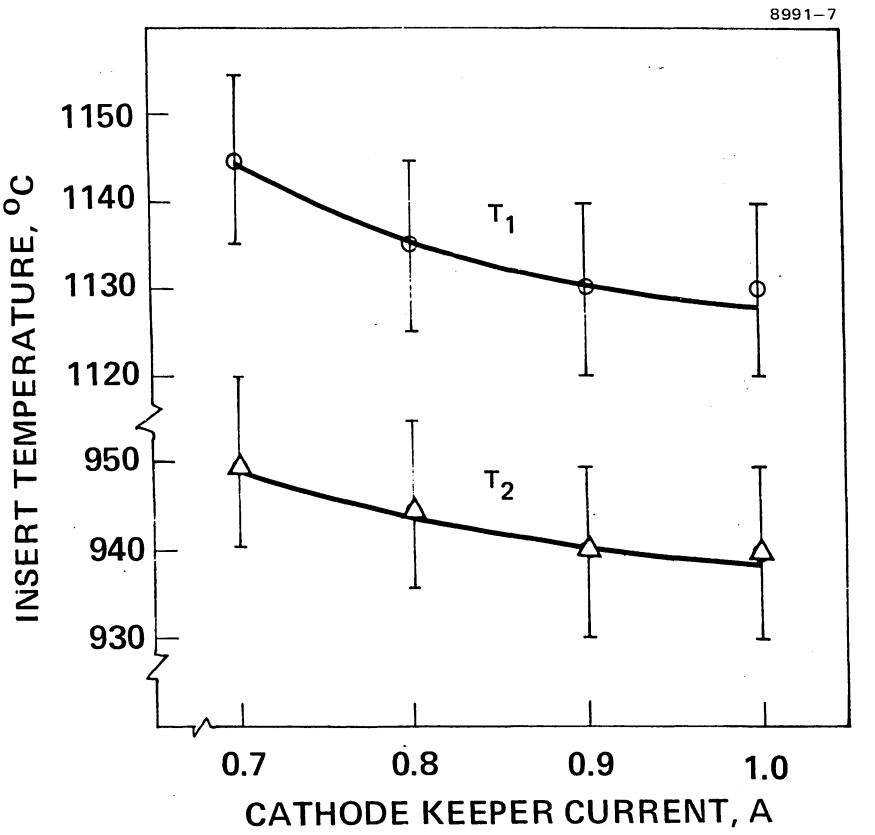

Figure 3-8. Variation of insert temperature with cathode-keeper current, keeper voltage also varied, other parameters constant. (J_E = 12 A, V_D = 32 V, J_b = 2 A).

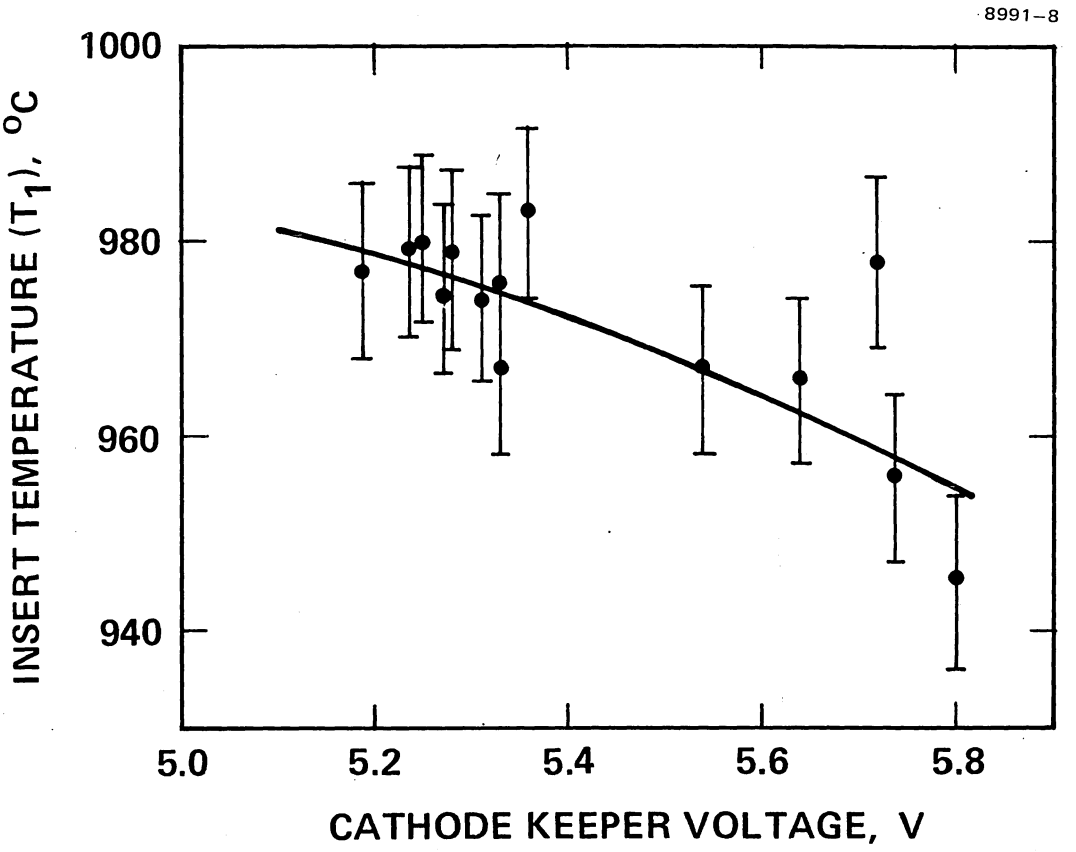

Figure 3-9. Variation of insert temperature (T_1) with cathode-keeper voltage, keeper current constant. Variation is for changes in magnetic-baffle current and discharge voltage at constant cathode emission current of J_E = 12 A.

most variation, but the effect is probably more dependent on the combination of parameters that had to be varied to produce the changes in keeper voltage (cathode-keeper voltage cannot be varied independently if cathode-keeper current is held constant).

The last set of thruster operating parameters available for variation are magnetic-baffle current and cathode propellant flow. When discharge voltage and emission current are held constant, these parameters vary together, and the results are shown in Figure 3-10. Again, the variation is not appreciable, although insert temperature does appear to increase slightly with cathode propellant flow. Experiments were also performed to observe the effect on insert temperature of operating the thruster with and without ion-beam extraction. Keeping all other parameters as constant as possible, a 10°C increase in insert temperature was observed at both locations when the ion beam was extracted. Consequently, research and development efforts conducted in bell-jar configurations (where currents and voltages are kept similar to those representative of thruster operation) should provide results that are valid for thruster operation.

Other parameters that were explored included the presence of contaminant gases in the vacuum chamber. Figure 3-11 shows that adding nitrogen and methane had little or no effect on the insert temperature. An attempt was also made to correlate thruster start-up with prior cathode treatment and/or the use of the current J-series thruster cathode conditioning cycle (shown in Figure 3-12) that was used to condition the insert initially and after subsequent exposure to air. Cathode start-up reliability could not be correlated with prior treatment of the vacuum chamber or the thruster, and the start-up sequence represented by the temperature history shown in Figure 3-13 (for the first 35 min) invariably produced cathode ignition and insert operating temperatures that were repeatable within the accuracy of the temperature measurement. Figure 3-13 also shows the effect of not turning off the cathode heater at the instant of keeper and discharge ignition. Although the insert temperatures exceed the "normal" temperature for the J_E = 6 A emission current set-point that is programmed for discharge ignition, the insert temperatures are not so excessive as to cause permanent damage. The

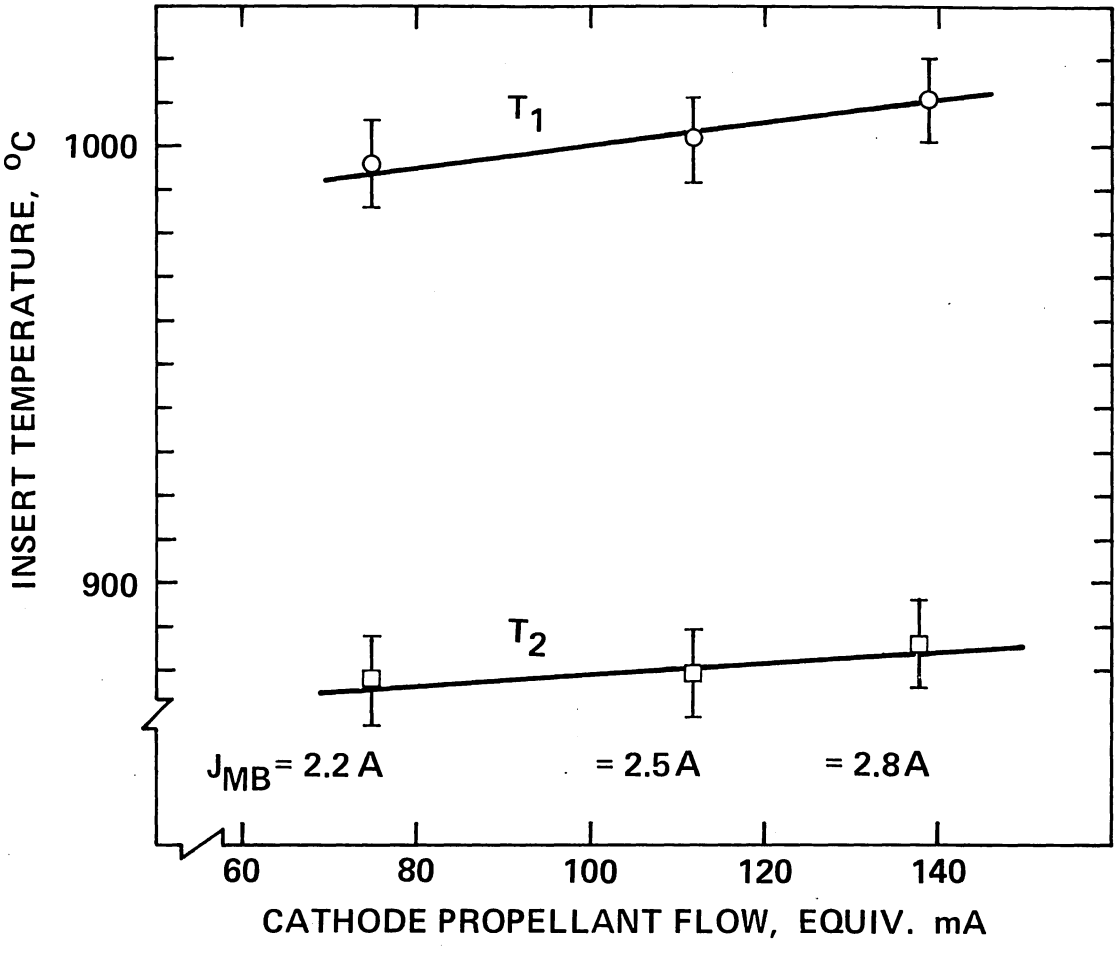

Figure 3-10. Variation of insert temperature with cathode flow rate for constant discharge voltage and current. Variation was obtained by changing magnetic-baffle current. (V_D = 32 V, J_b = 2 A, ε_i = 192 eV/ion).

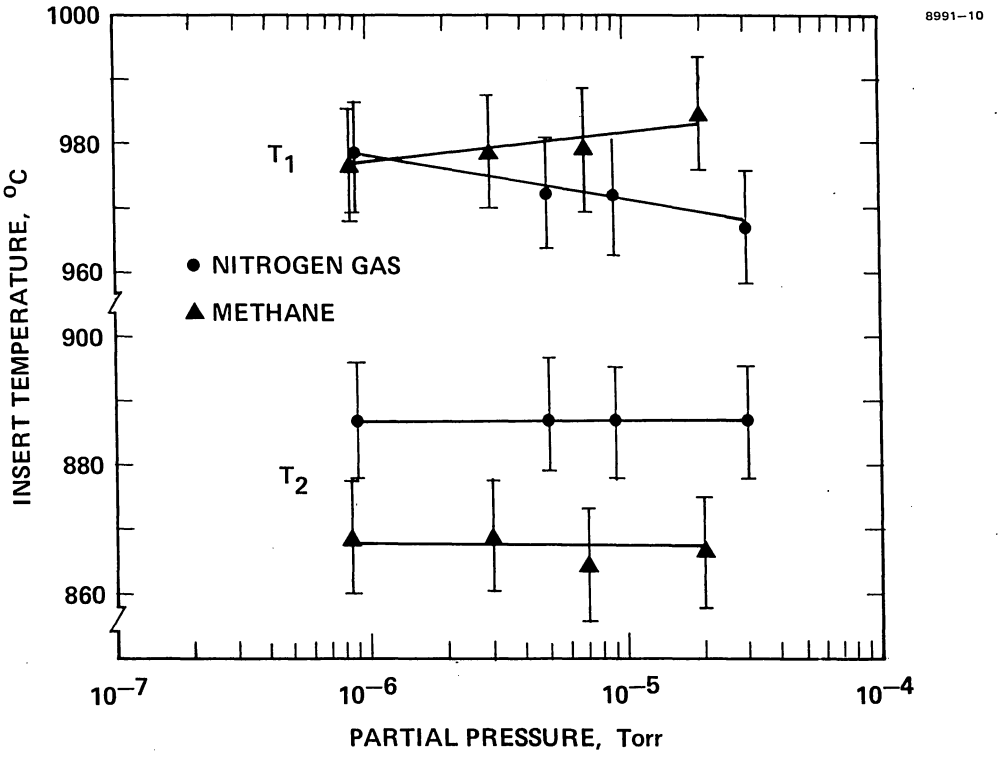

Figure 3-11. Variation of insert temperature with partial pressure of contaminant gases. (V_D = 32 V J_b = 2 A, ε_i = 192 eV/ion).

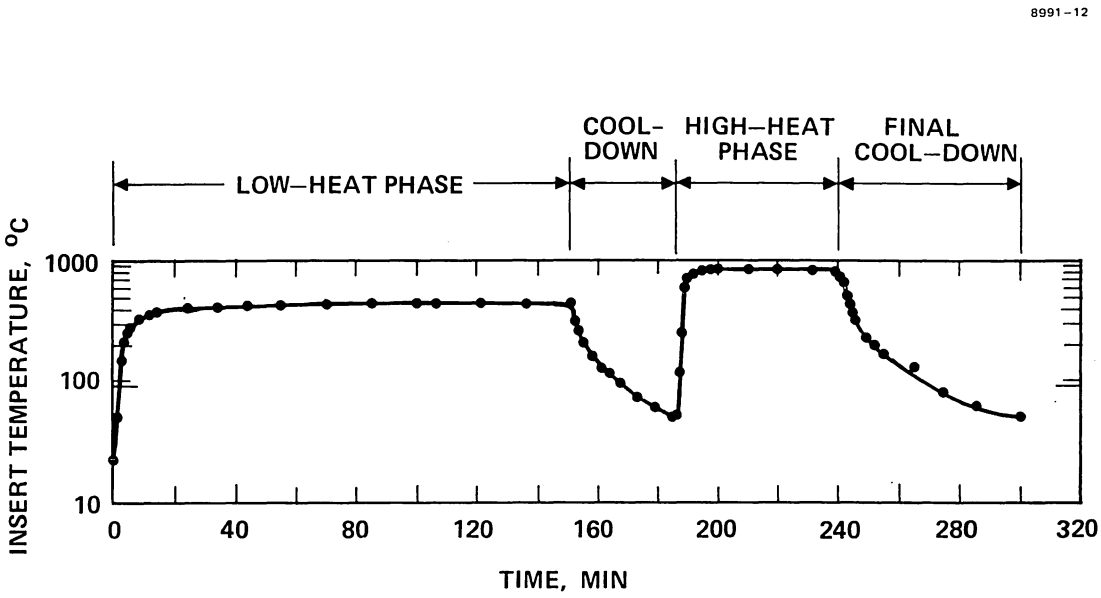

Figure 3-12. Time history of insert temperature during cathode conditioning cycle (upstream thermocouple location, T_2).

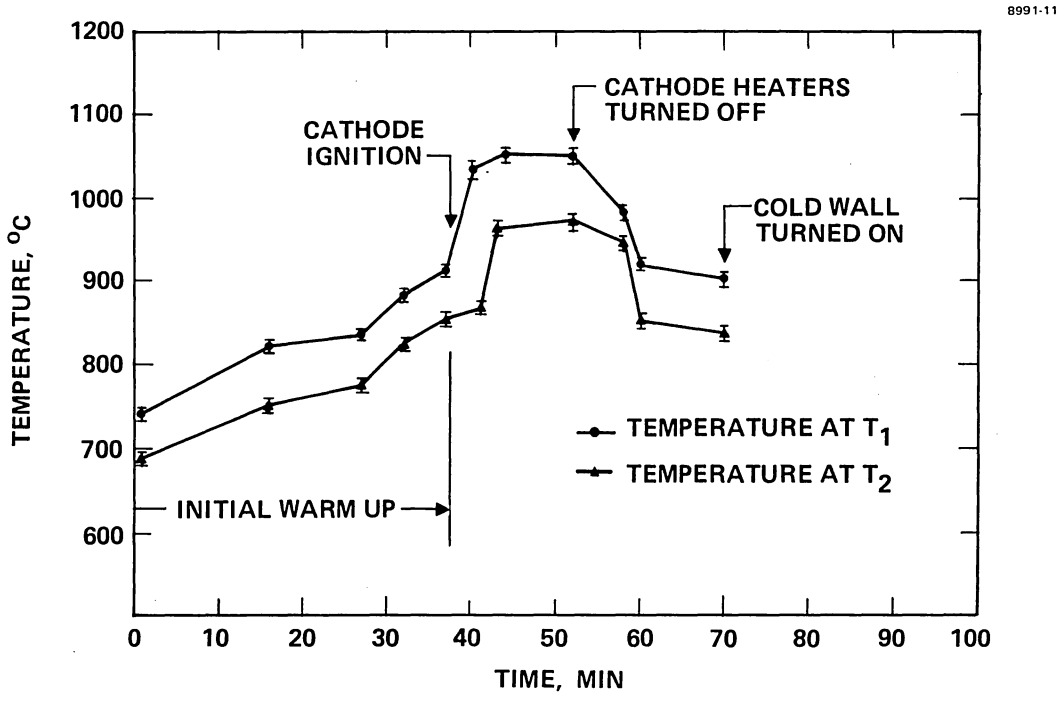

Figure 3-13. Insert temperature variation during thruster startup sequence.

relatively long warm-up period of this start-up sequence is probably sufficient to out-gas any contamination that the thruster cathode would receive in normal handling; however, this observation should not be interpreted as meaning that thruster cathodes are invulnerable to any form of contamination. The intent of our cathode environmental correlations was to establish that, with nominal care, the performance capability can be preserved (in contrast to determining what is required to destroy the cathode's emission capability).

The experimental results presented here indicate that the primary factor that determines insert operating temperature is the cathode emission current. The results presented were repeated at least once (the insert was tested for over 50-hr total) and are considered representative of the LeRC/Hughes J-series-thruster cathode design.

E. CATHODE LIFETIME MODEL

In the preceding contract (NAS 3-19703), barium loss was measured as a function of temperature by heating the porous-tungsten inserts in a typical hollow-cathode configuration, but under ultra-high vacuum conditions. This measurement technique accounts for any retardation in barium loss that could result from the barium vapor pressure within the cathode, and also for view factors that reduce the probability that barium vapor is lost from the insert surface. An analytic expression for describing barium loss from porous-tungsten matrices has been validated by Brodie, Jenkins, and Trodden,[3-8] and this form will be used here to develop a lifetime model for the cathode. Barium loss from a porous-tungsten insert varies with both time and temperature in accordance with the following relationships:

$$\ln \frac{dq}{dt} = C_1 - \frac{C_2}{T} \tag{3.1}$$

$$\frac{dq}{dt} = C_3 \, t^{-1/2} \quad , \tag{3.2}$$

where q is the quantity of barium lost, T is temperature in °K, t is time of operation, and C_1, C_2, C_3 are constants. If one assumes that q_o is the quantity of barium available in the impregnate at the beginning of life, then Eqs. 3.1 and 3.2 can be combined and integrated to obtain

$$\frac{q}{q_o} = C\, e^{-a/T}\, t^{1/2} \quad , \tag{3.3}$$

where a and C are constants. By using the data obtained under Contract NAS 3-19703, a and C were determined to be

$$a = 1.61 \times 10^4 \ °K \tag{3.4}$$

$$C = 400 \ hr^{-1/2} \quad . \tag{3.5}$$

In the preceding section, it was determined that the primary operating parameter (or variable) determining insert temperature is the cathode emission current J_E. Fitting the available data like that shown in Figure 3-5 to obtain linear dependence results in

$$T_1 = 1140 + 9.4\, J_E \tag{3.6}$$

$$T_2 = 1010 + 11.2\, J_E \tag{3.7}$$

for the range $5 \text{ A} < J_E < 35 \text{ A}$. Assuming that the higher temperature, T_1, controls end of life, Eqs. 3.3 and 3.6 can be used to relate the time t required to deplete the barium remaining in the porous-tungsten insert to the fraction q/q_o of the initial quantity as a function of the temperature. This relationship is shown graphically in Figure 3-14. At best, $q/q_o \leq 0.5$ because at least one-half of the barium reacts with the porous-tungsten substrate to form products that do not participate in lowering the work function of the surface of the porous-tungsten insert. It is reasonable to assume that at least 50% of this remaining fraction of

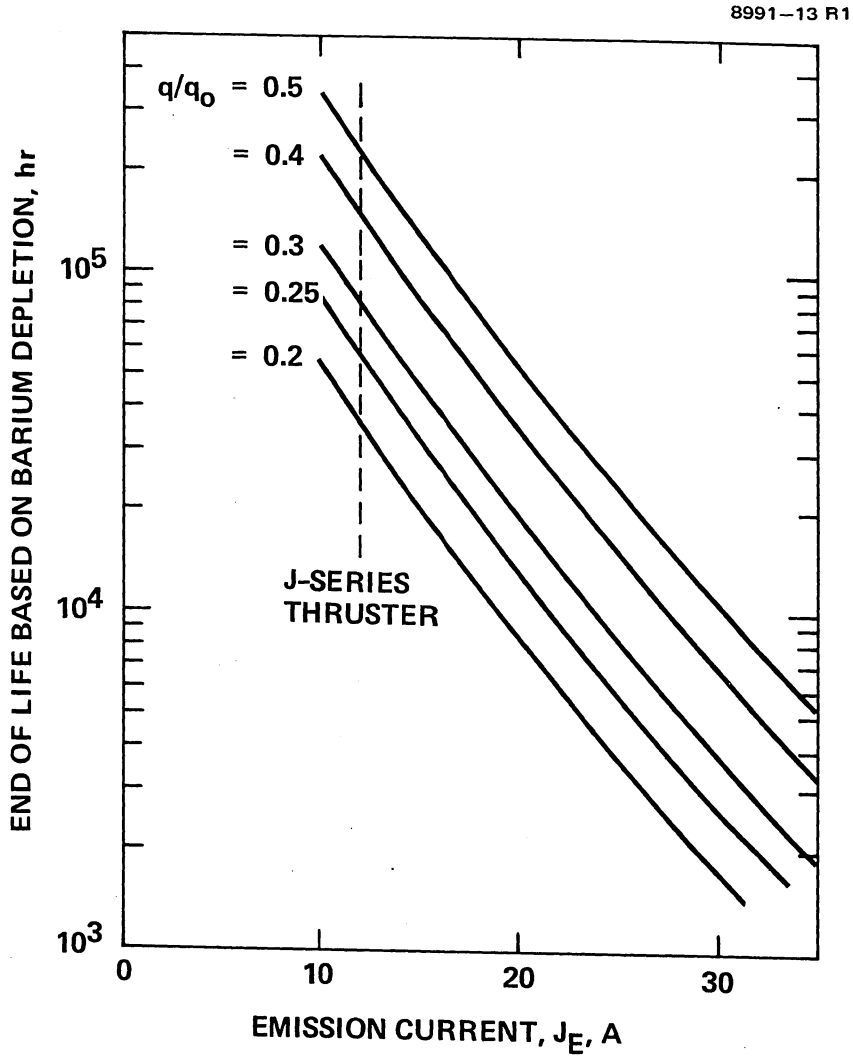

Figure 3-14. End of life based on barium depeletion of an impregnated porous-tungsten-insert hollow cathode as a function of discharge emission current and fraction of initial barium available (q/q_o).

barium is available and can reach the insert surface. Therefore, end-of-life values corresponding to $0.25 \leq q/q_o \leq 0.5$ should provide meaningful estimates of cathode lifetime as a function of cathode emission current. For J-series-thruster operating conditions, the calculated cathode lifetime would be on the order of 55,000 hr.

It would be desirable to have an empirical value for q/q_o that corresponds to diminished cathode performance and therefore the end of useful life. An initial study of ways to achieve artificial or accelerated aging led to the conclusion that any such attempt could not be made representative of normal operation and there would be a high probability of forming compounds that diffuse more slowly or not at all. Consequently, lifetime might appear to be far shorter than it would be in normal operation. The observation that insert temperature is essentially the same with or without ion-beam extraction will allow the long-duration "bell jar" tests being performed at NASA LeRC to be used for determining a value of q/q_o (from Figure 3-14) that represents the end of useful life for thruster hollow cathodes.

F. COMPARISON OF CALCULATED AND MEASURED EMISSION CURRENTS

The total current emitted from the insert can be calculated from the data collected during this study. Since there is a temperature drop along the insert, the current density must be calculated and the total current is obtained by integrating over the insert surface. The theoretical current density j_{th} is written

$$j_{th} = A_o T^2 \exp\left(-\frac{e\phi}{kT}\right) , \quad A/cm^2 , \tag{3.8}$$

where A_o is 120 $A/cm^2\ deg^2$; k is the Boltzmann constant; e is the electronic charge; T is the emitter temperature determined by

$$T = 1277 - 55\,x , \quad °K , \tag{3.9}$$

where x is the distance from the orifice plane in cm; and ϕ is determined by[3-9]

$$\phi = 1.38 + 3.9 \times 10^{-4} T \quad , \quad eV \quad . \tag{3.10}$$

Summing the current computed using Eqs. 3.8 through 3.10 yields a total emitted current J_{th} = 11.1 A. The total experimentally observed cathode emission is J_{ex} = 13 A for the temperature data used (the sum J_E = 12 A of emission current plus J_{CK} = 1 A of keeper current), and the difference is readily explainable in terms of positive-ion current or by assuming field enhancement.[3-3]

The work performed under this task provides a correlation between prior cathode investigations reported in the literature and ongoing work. The data obtained should provide confidence in the applicability of Refs. 3-1, 3-2, and 3-5 to the hollow-cathode configuration used in the LeRC/Hughes J-series 30-cm thrusters. The only remaining questions relate to changes in design for scaling to higher or lower emission currents or operation with gases other than mercury vapor.

Page intentionally left blank

REFERENCES FOR SECTION 3

3-1. H.R. Kaufman, "Technology of Electron Bombardment Thrusters," Advances in Electronics and Electron Physics 36, Academic Press, Inc., San Francisco, 1974.

3-2. L.A. Rehn, "Argon Hollow Cathode," NASA CR-135102. Thesis for Grant NSG-3011, November 1976.

3-3. L.A. Rehn and H.R. Kaufman, "Correlation of Inert Gas Hollow Cathode Performance," AIAA 78-707, Colorado State University. Presented at AIAA 13th Elec. Prop. Conf., San Diego, CA, April 1978.

3-4. H.L. Witting, "Hollow Cathodes with Thermionic Cathodes," J. Appl. Phys. 42, 5478 (1971).

3-5. M.J. Mirtich and W.R. Kerslake, "Long Lifetime Hollow Cathodes for 30 cm Mercury Ion Thrusters," AIAA Paper No. 76-985, AIAA International Electric Propulsion Conference, Key Biscayne, Florida, November 1976.

3-6. R.J. Martin, and J.E. Rowe, "Experimental Investigation of the Low Voltage Arc in Noble Gases," J. Appl. Phys. 39, 4289-98 (1968).

3-7. S.N. Salinger and J.E. Rowe, "Determination of the Predominant Ionization and Loss Mechanisms for the Low-Voltage Arc Mode in a Neon Plasma Diode," J. Appl. Phys. 39, 4299 (1968).

3-8. I. Brodie, R.O. Jenkins, and W.G. Trodden, "Evaporation of Barium from Cathodes Impregnated with Barium-Calcium-Aluminate," J. of Electronics and Control, 6, February 1959, p. 149-161.

3-9. A.V. Druzhnin, A.I. Melnikov, and V.I. Nekrasov, "The Limiting Emission Current of an Impregnated Aluminate Cathode," Radio Engineering and Electronic Physics 5, 803-6, 1967.

Page intentionally left blank

SECTION 4

ACCELERATOR GRID SYSTEM TECHNOLOGY

The basic principles that govern acceleration and focusing of ions to form a well-collimated beam are relatively well understood and have been documented both analytically and experimentally by several investigators in Refs. 4-1 through 4-16. The goal of this task was to use the data available from these analyses and experiments to formulate a descriptive model for the LeRC/Hughes 30-cm mercury ion thruster hardware that would be useful for predicting the capabilities and limitations of a "state-of-the-art" thruster. Since the state of the art changed somewhat (the thruster design was advanced from the 900-series to the J-series design) during the study, it was necessary to redesign the accelerator grid assembly to achieve the performance goals. As a consquence, a better understanding of the support structure for the accelerator grid system needs to be developed for describing the experimental observations. Hence, the work performed under this task succeeded only in completing the groundwork for analyzing ion optics assembly capabilities, and the descriptive model is only partially complete. The approach and results obtained are described in this section.

A. DESIGN VARIABLES AND DESCRIPTIVE MODELS

State-of-the-art 30-cm mercury ion thrusters employ two electrodes to extract, accelerate, and focus the ion beam. These acceleration electrodes have thousands of apertures configured as shown in Figure 4-1. In addition to aperture design specifications, the 30-cm thruster accelerator electrodes are curved so that the deformation caused by thermal stress occurs in a predictable way. The design variables used to specify electrode curvature are shown in Figure 4-2. The primary goal of this task was to use these design variables to formulate a descriptive model for predicting the following performance characteristics:

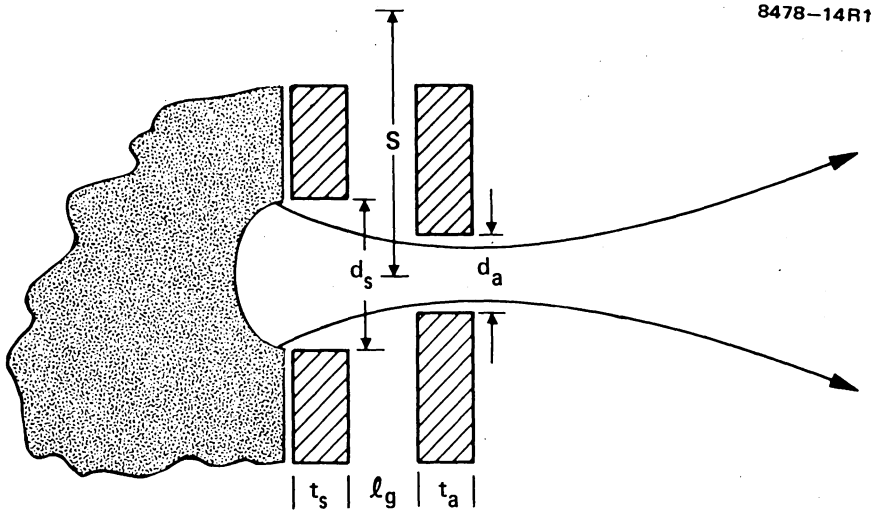

d_a - ACCEL HOLE DIAMETER
d_s - SCREEN HOLE DIAMETER
t_a - ACCEL GRID THICKNESS
t_s - SCREEN GRID THICKNESS
ℓ_g - SCREEN-TO-ACCEL INTERELECTRODE SPACING

ϕ_a - ACCEL GRID OPEN AREA FRACTION $\frac{\sqrt{3}\pi}{6}\frac{d_a^2}{S^2}$

ϕ_s - SCREEN GRID OPEN AREA FRACTION $\frac{\sqrt{3}\pi}{6}\frac{d_s^2}{S^2}$

S - APERTURE SPACING

Figure 4-1. Definition of design variables for ion-optics apertures.

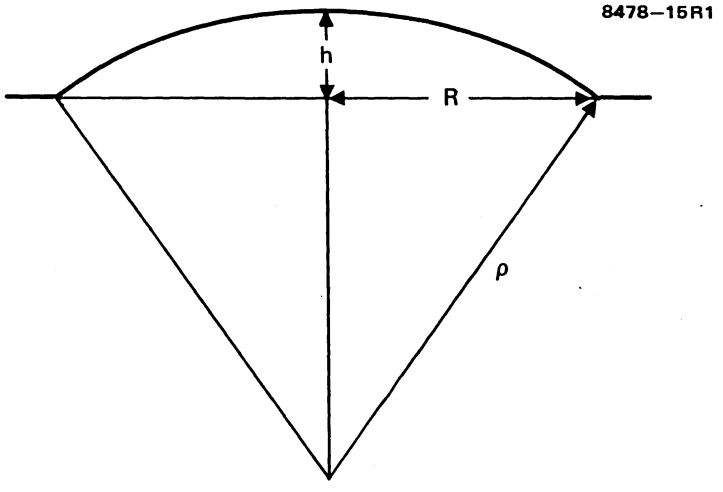

h - DISH DEPTH
R - GRID RADIUS
ρ - RADIUS OF CURVATURE

Figure 4-2. Definition of design variables for accelerator-electrode curvature.

- Perveance
- Screen grid lifetime
- Thrust loss
- Backstreaming limit
- Propellant utilization efficiency
- Discharge chamber performance
- Accel grid lifetime
- High-energy, high-angle ions
- Thermal expansion of grids
- Beamlet divergence compensation.

Once these performance characteristics are related quantitatively to design and operating variables, the limits for increasing thrust and power density can be readily assessed.

We began the study by compiling the data contained in the 16 references cited previously for the formulation of qualitative behavior. Table 4-1 summarizes the comparisons that were made for establishing trends, and the analytical expressions that can be used for determining quantitative evaluations. It should be noted that performance characteristics are both implicit and explicit functions of design and operational variables. The arrows shown in the table identify whether there is a direct (arrow pointing up) or an inverse (arrow pointing down) relationship between a given performance characteristic and a design variable. For example, an increase in accel aperture diameter d_a would be expected to (1) increase perveance, (2) decrease screen grid lifetime, (3) decrease the thrust loss factor α and increase the thrust loss factor F_t, (4) increase the magnitude of the accel voltage required to prevent backstreaming, (5) decrease propellant utilization efficiency, and (6) increase the discharge power required to produce a given beam current at a constant propellant-utilization efficiency. Although Table 4-1 is essentially self-explanatory, a few comments are appropriate with regard to each characteristic.

Table 4-1. Ion-Optics Performance Characteristics and Their Relationships to Electrode and Thruster Design Variables

Performance Characteristics	Design Variables								Analytical Expression[d]
	d_a	t_a	ϕ_a	d_s	t_s	ϕ_s	ℓ_g	F	
Perveance	↑[a]	↓[a]			↓[a]		↓[a]	↑	$P = \frac{j_{max} F \phi_s A_b}{V_t^{3/2}} \propto \frac{d_s^2}{\ell_e^2}$
Screen grid lifetime (SGL)	↓[b]		↓[b]	↑	↑	↑		↑	$SGL = \frac{\delta t_s e \rho F \phi_s A_b}{J_b} \frac{1 + J_+^{++}}{S^+ + \frac{1}{2} J_+^{++} S^{++}}$
Thrust loss									
1. α	↓[b]		↓[b]					↑	$\alpha = \frac{1 + \frac{1}{2} J_+^{++}}{1 + J_+^{++}}$
2. F_t	↑[b]		↑[b]				↑[c]		$F_t = \frac{\int_0^R 2\pi r j(r) \cos\theta(r) dr}{J_b}$
Backstreaming limit	↑[a]	↓[a]					↓[a]		$\lvert V_a \rvert = \frac{V_b}{\left[2\pi \frac{\ell_e}{d_a} \exp(t_a/d_a)\right] - 1}$
Propellant utilization	↓[a]		↓[a,b]	↑		↑[a]			$\eta_u = \frac{1}{1 + \frac{v_o \phi_a}{4 \nu \phi_s V/A}}$
Discharge losses	↑[a]		↑[a]	↓		↓[a]			$\varepsilon_i = \frac{C_i A}{\phi_s A_b}$
Accelerator grid lifetime (AGL)		↑					↓	↑	$AGL = \frac{3\sqrt{3}}{64} \frac{F e^2 v_o p}{S^+ \sigma_{ce} J_b^2} \frac{r_a^2 \pi d_a^2 (s - d_a)^2 t_a}{(2\ell_e + t_a)} \frac{\eta_u}{1 - \eta_u}$

[a] Results of Rawlin[4-9]

[b] Results of Vahrenkamp[4-7]

[c] Results of Aston[4-3]

[d] Definitions of symbols not previously used:

- j = current density
- J_b = beam current
- δ = fractional thickness of screen grid
- r = radial coordinate
- R = thruster radius
- θ = beamlet divergence angle
- η_u = propellant utilization (discharge only)
- A = area of primary electron region
- A_b = area of ion beam envelope
- S^+ = sputtering coefficient for singly charged ions
- S^{++} = sputtering coefficient for doubly charged ions
- V_b = beam voltage
- V_a = accelerator voltage
- v_o = neutral speed
- ν = collision frequency
- V/A = volume-to-area ratio of primary electron region
- C_i = plasma ion production cost
- e = electronic charge
- ρ = atom density of electrode
- F = beam flatness parameter
- J_+^{++} = ratio of J^{++}/J^+ on axis
- $\ell_e^2 = \ell_g^2 + \frac{d_s^2}{4}$
- σ_{ce} = charge exchange cross section

6758

Perveance — The analytic expression given for perveance in Table 4-1 was formulated for analyzing existing data with the goal of developing an expression that relates ℓ_g and t_s to observed perveance. In principle, it should be possible to formulate an expression for the accelerator system perveance P in terms of the single aperture design parameters as follows:

$$P = nP_hF \quad , \tag{4.1}$$

where n is the number of apertures, P_h is the perveance per hole, and F is the beam flatness parameter (F is really a discharge plasma property). Aston[4-3] expresses P_h as

$$P_h = \frac{\pi\varepsilon_o}{9}\sqrt{\frac{2e}{m}}\left(\frac{d_s}{\ell_e}\right)^2 \quad , \tag{4.2}$$

where ε_o is the permittivity of free space, e is the electronic charge, m is the mass of the ion beam accelerated, and ℓ_e is the effective acceleration length. Kaufman[4-10] defined ℓ_e in terms of ℓ_g and d_s as

$$\ell_e^2 = \ell_g^2 + d_s^2/4 \quad , \tag{4.3}$$

and relatively good agreement between theory and experiment was obtained in the experimental ion optics investigations described in Refs. 4-1, 4-2, and 4-3. Recent perveance measurements performed on the LeRC/Hughes J-series 30-cm thruster under NASA contracts NAS 3-21052 and NAS 3-21357 produced data that cannot be correlated using Eqs. 4.1 and 4.2 unless ℓ_e is made dependent on thruster operating parameters. The interelectrode spacing ℓ_g was identified as varying with the thruster temperature, and no further attempts were made to refine the perveance model.

Screen-Grid Lifetime — The expression formulated for assessing screen-grid lifetime was generalized to define the ion sputtering erosion in terms of the electrode-assembly design variables. Since the screen grid is also a boundary of the discharge chamber, modeling of screen-grid wear rate and the factors that affect wear rate were discussed in Section 2.

Thrust Loss — Actual thrust produced by an ion thruster is less than the value that is computed on the basis of measured ion beam current and net accelerating voltage because the ion beam contains doubly charged ions and also because ion trajectories have radial velocity components. The thrust loss factor α provides the correction for calculated thrust to account for doubly charged ions, and F_t provides the correction for non-axial ion-velocity components. The design of the ion accelerator assembly can only influence α through its effects on the percentage of charged and neutral propellant, which causes changes in the relative rate of doubly charged ion production. The thrust factor F_t is a direct measure of the focusing capability of the aperture design. Like perveance, ℓ_g has a first-order effect on F_t.

Backstreaming Limit — The electrons that are emitted into the extracted ion beam to establish space-charge neutrality will "backstream" through the accelerator system electrodes unless the negative voltage applied to the accelerator grid is adequate to establish a barrier. The voltage required to prevent backstreaming is called the backstreaming limit, and the mathematical expression shown in Table 4-1 effectively predicts the limit. Figure 4-3 shows the correlation with experimental measurements. Note that by calculating ℓ_e to include the effect of a change in ℓ_g that accounts for thermal deformation, the corrrelation is significantly improved.

Propellant Utilization Efficiency — The expression for propellant utilization efficiency has been relatively well verified and the only uncertainty is in specifying the volume-to-area ratio V/A for the primary electron region.

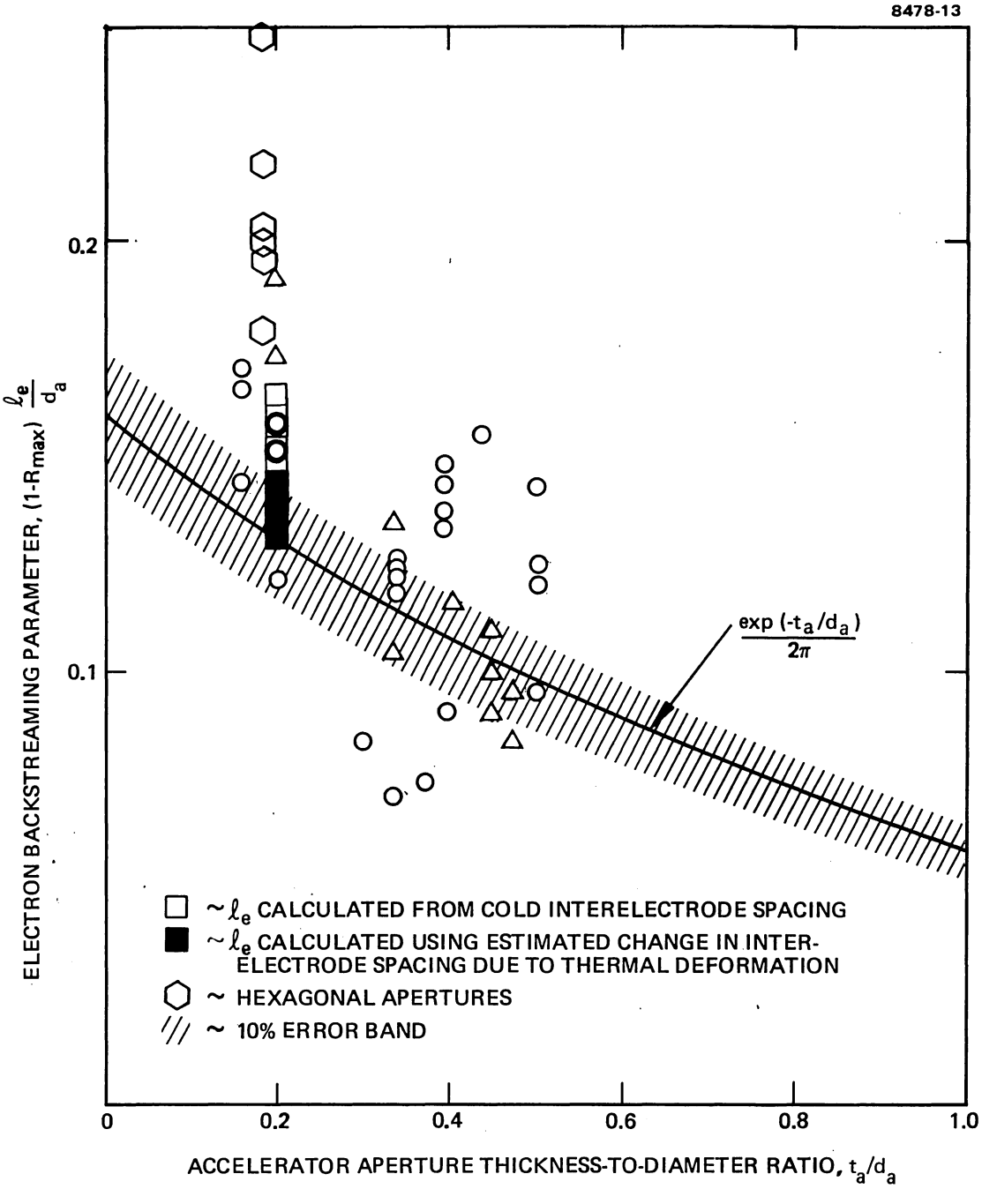

Figure 4-3. Correlation of experimental electron backstreaming parameter with accelerator-electrode thickness-to-diameter ratio. The calculated variation shown is based on the analytical expression in Table 4-1.

Discharge Losses — The energy required to ionize the neutral propellant in the discharge chamber has been termed the discharge loss, ε_I. The only way in which the ion accelerator grid assembly can affect these losses is through the effective screen-grid transmission ϕ_s. Since every ion that is neutralized on the screen grid and returned to the discharge chamber increases the discharge loss, ϕ_s should be as high as possible consistent with structural integrity.

Accelerator Grid Lifetime — The expression shown for accelerator grid lifetime was derived on the basis that the total production of charge-exchange ions sputter-erodes the web area of the accelerator grid. End of life was defined, somewhat arbitrarily, as the time required to erode away a volume that has a base of triangular cross section as shown in Figure 4-4 and a height equal to the thickness of the grid. Although the integrity of the accelerator grid would not be threatened by the loss of this amount of material, the increase in neutral propellant loss would probably change thruster performance significantly.

We did not study the performance characteristics associated with the high-energy ions ejected from the thruster at large angles with respect to the thrust axis and with beamlet divergence compensation. Thermal expansion of the accelerator grids and their supporting assembly became the primary subject of the investigation because a meaningful description of the accelerator-grid performance characteristics could not be formulated without accounting for thermally driven dimensional changes, particularly in ℓ_g.

B. THERMAL/STRUCTURAL ANALYSIS

Initial test results obtained with the LeRC/Hughes J-series thruster under NASA Contract NAS 3-21357 indicated that a dimensional stability problem existed in the ion-accelerator grid system subassembly. The effects of differential expansion of the titanium grid mounting and the molybdenum grids were analyzed at NASA LeRC using a structural analysis computer code known as FEATAG. This analysis showed that the grids were indeed deformed by the thermal expansion of

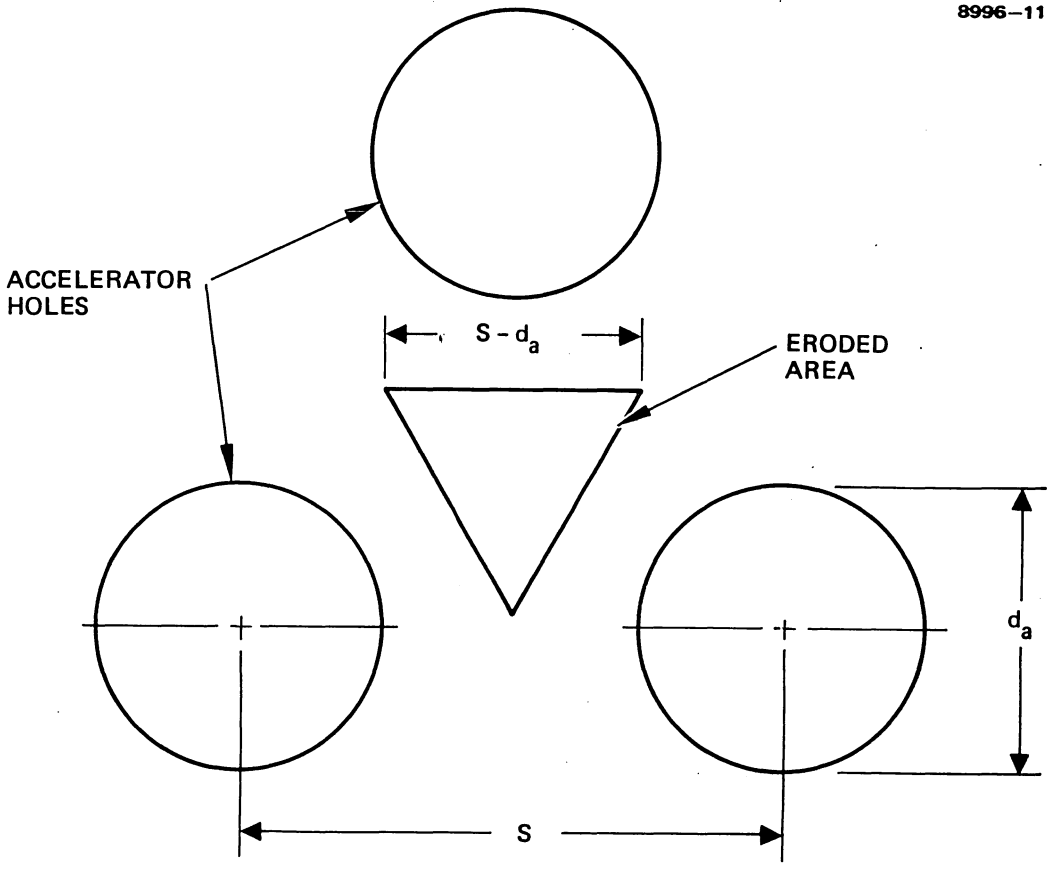

Figure 4-4. Definition of the area used in determining the volume of accelerator-grid material that is eroded away when end of accelerator-grid life has been reached.

the titanium mount and that the displacement could explain the observed performance (at least qualitatively). Consequently, the two prerequisites to further refinement of the ion accelerator grid performance model were (1) measurement of the temperature dependence of the grids and supporting structure as a function of operating conditions and (2) the computation of the deformation based on the temperature dependence. Because of the urgency of accurately assessing the stability of the ion accelerator grid assembly, parallel, semi-independent investigations were conducted at HRL and NASA LeRC so that results could be compared.

1. Temperature Measurements

Thermocouples were installed on the grids of a 30-cm thruster (representative of the J-series design), and temperatures were measured as a function of discharge current (without extracting an ion beam). Figure 4-5 shows the temperatures measured at the screen and accel grid locations as designated in the included sketch. The temperature measurements made at NASA LeRC and HRL are in good agreement at location 3; however, the screen grid temperature T_1 is lower in the center for the NASA LeRC center data, and the accel grid temperatures are higher. The only possible explanation is that the thruster used for the HRL experiments does not have exactly the same cathode pole-piece geometry as the J-series and may therefore have a somewhat different discharge plasma distribution.

The HRL thruster was reconfigured in a single-cusp magnetic field geometry to explore the effect of plasma uniformity. Temperature was measured and the results are presented in Figure 4-6. The beam flatness parameter F was measured to be about 0.8 for the single-cusp magnetic field configuration, as compared to about 0.4 for the divergent field configuration. Consequently, to analyze accelerator grid system limitations, the single-cusp discharge chamber was operated to a maximum discharge current of J_D = 32 A (corresponding to a 6-A beam current) to obtain

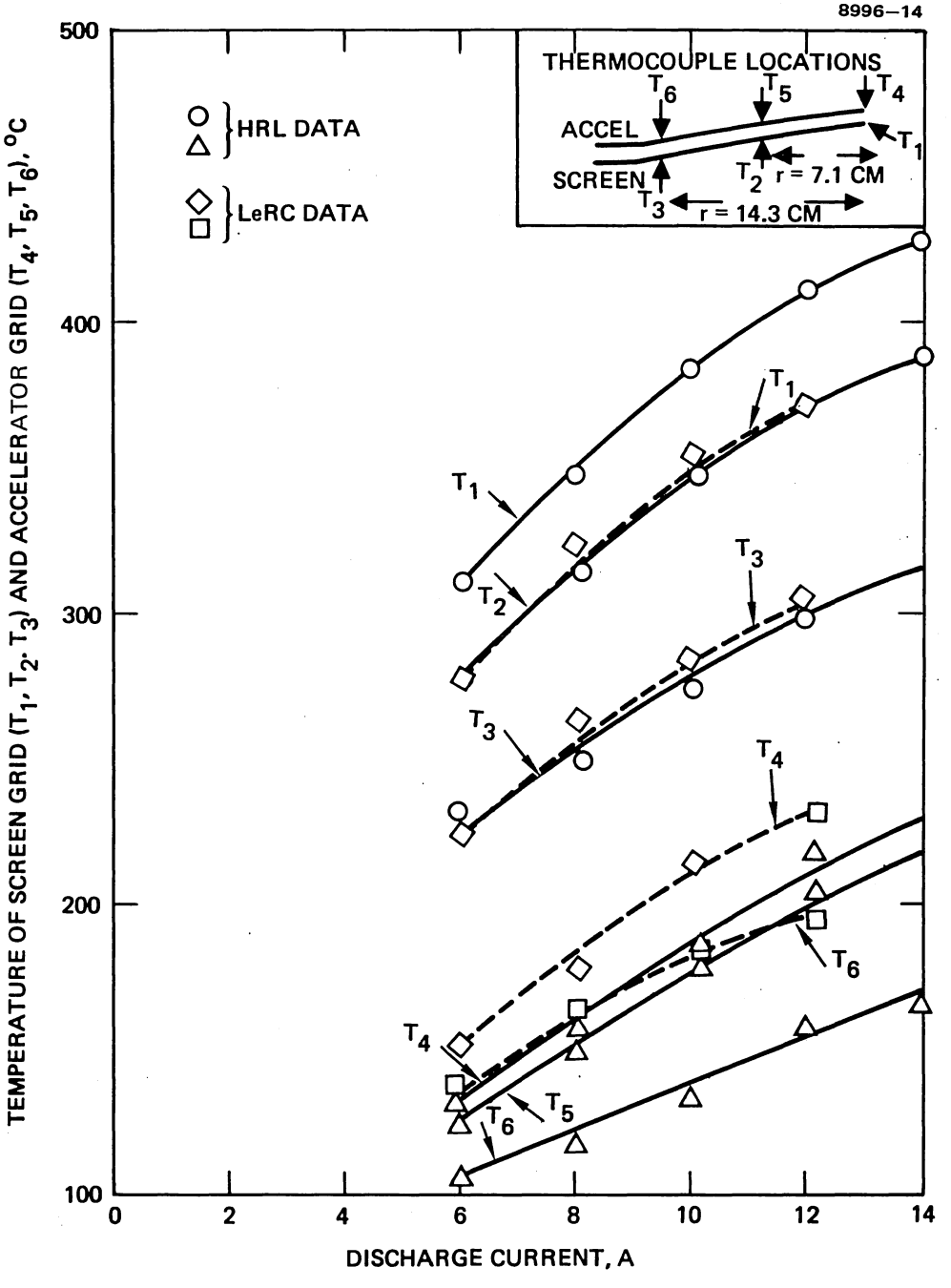

Figure 4-5. Screen and accel-grid temperatures as functions of discharge current.

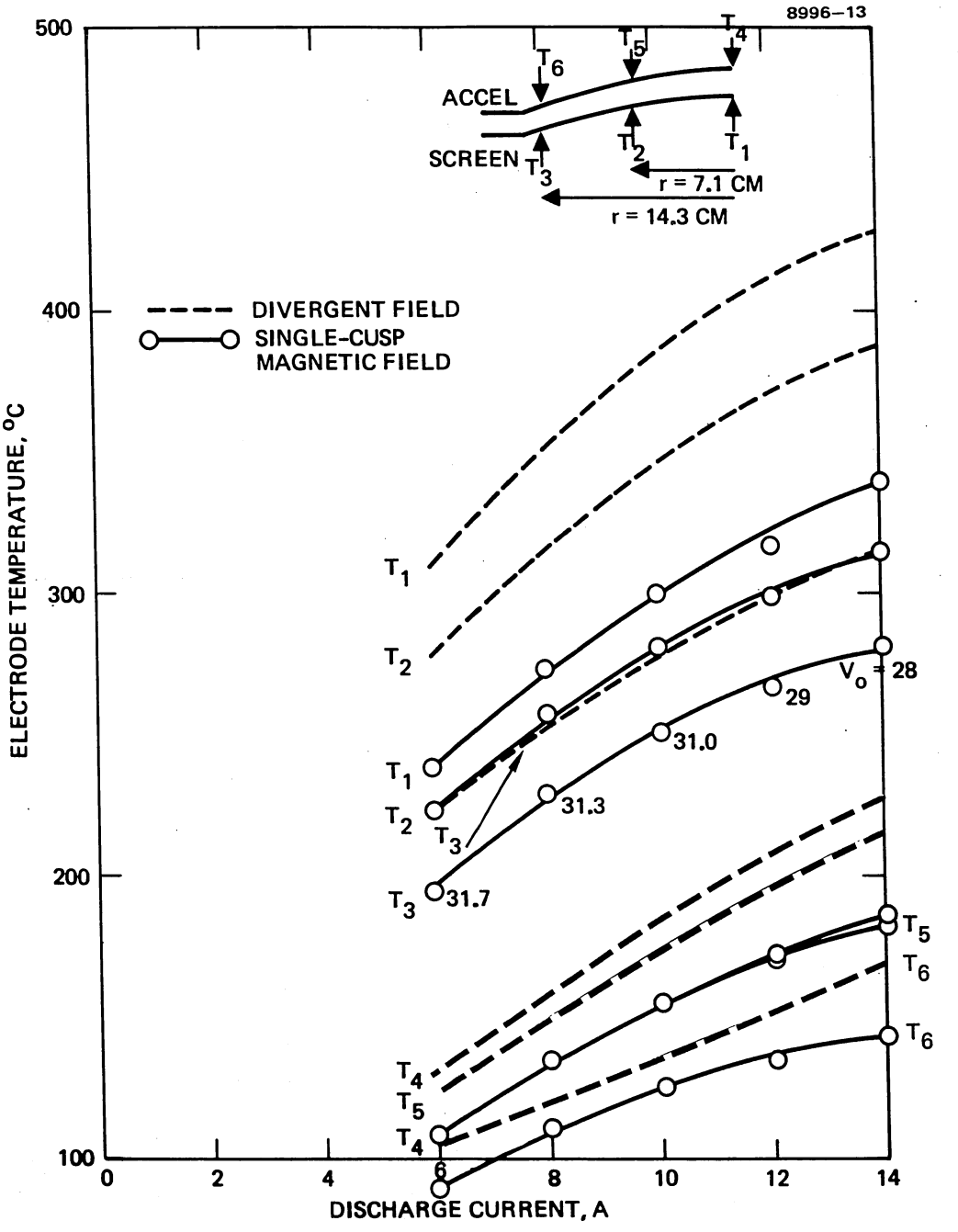

Figure 4-6. Screen and accel-grid temperature as functions of discharge current for divergent and single-cusp magnetic-field geometries.

temperature dependence. To illustrate that the grids are essentially radiatively cooled, the grid temperatures are shown in Figure 4-7 as a function of the fourth-root of the discharge power. It is apparent that using a single-cusp discharge-chamber geometry should permit operating the accelerator-grid system at significantly higher beam current (discharge power) levels before thermal deformations limit performance.

2. Finite Element Stress Analysis of the Ion Accelerator Grid System

The initial results obtained at NASA LeRC with the FEATAG computer modeling of the accelerator grid system showed significant variation of the interelectrode spacing when differences in the temperatures of the screen and accel grids were assumed. To explore this effect, the FEATAG computer code was obtained and checked out on the HRL computer. Initial attempts at reproducing a test case resulted in substantially different values for displacements between results computed at HRL and at NASA LeRC. Errors were eventually traced to differences in the round-off error in library subroutines between the NASA LeRC UNIVAC and the HRL DEC-10 computers. Since the intrinsic precision of the two computers is identical, the computational techniques used in FEATAG were suspected of being unsuited for the analysis of the accelerator grid system as required here.

To explore this possibility, we sought help from several structural analysts at other Hughes facilities; they recommended a vendor, who was employed to independently check out the FEATAG code and compare it with other stress-analysis codes. The end result was that a comparison of results obtained with computer codes known as EASE 2 (Elastic Analysis for Structural Engineering) and ANSYS 2 produced nearly identical grid displacements for the test case. Comparing these results with those obtained using FEATAG disclosed that grid displacements were not in good agreement and were even in the opposite direction for some of the analysis-model nodes. The inaccuracy of the FEATAG code for analyzing this particular structural problem is thought to be associated with the

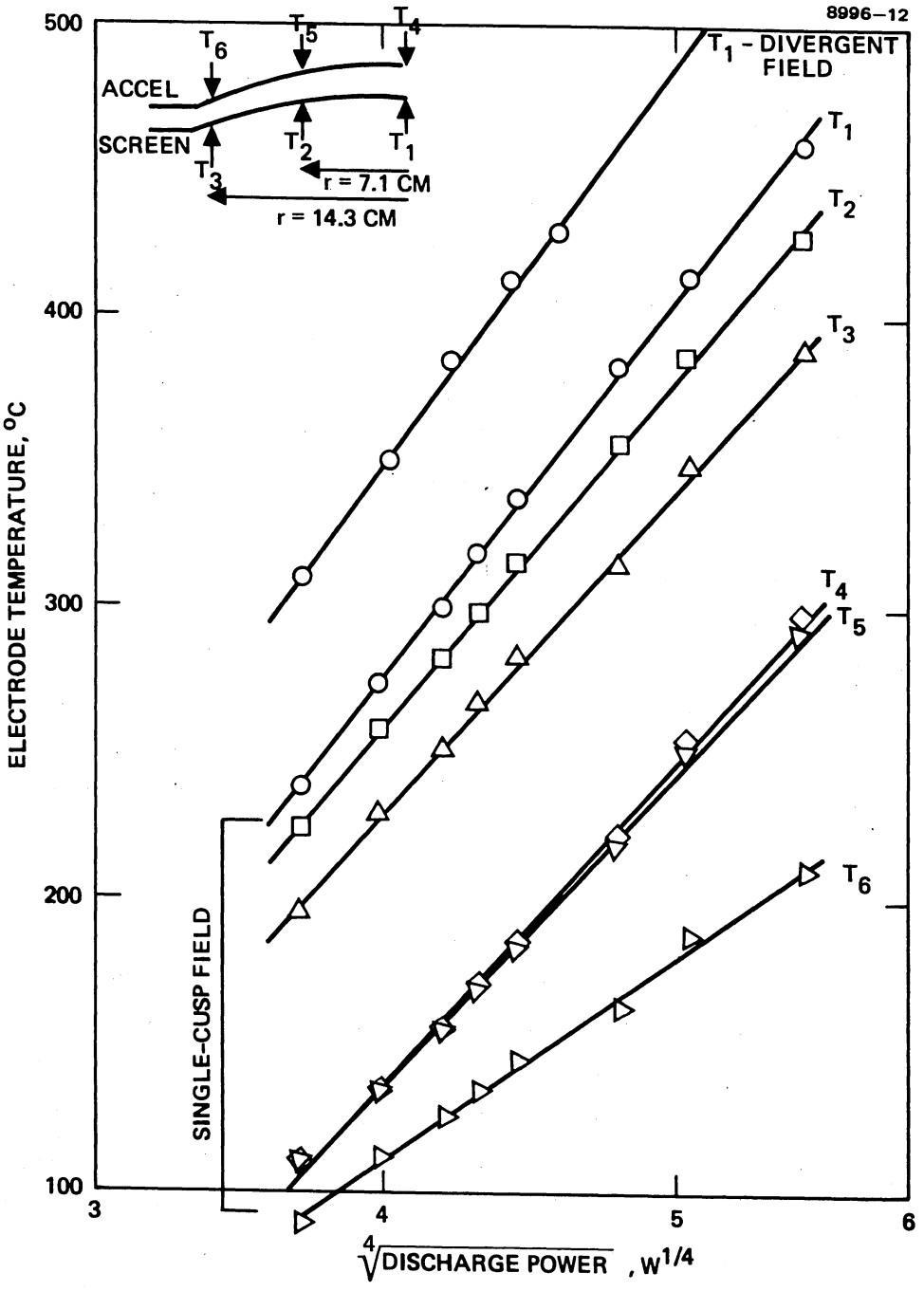

Figure 4-7. Comparison of screen and accel-grid temperatures for divergent-field and single-cusp magnetic-field geometry as a function of the fourth root of the discharge power (radiation cooling).

technique employed for matrix reduction. Software was purchased for performing the computations using EASE 2.

A cross section of the J-series 30-cm thruster ion accelerator grid assembly is shown in Figure 4-8. Both the screen and accel grids (molybdenum) are riveted to molybdenum stiffening rings. The grids are mounted to the titanium support ring at 12 places (note that the support ring is slotted at the point where the screen-grid stiffening ring is attached). The structure was modeled for the EASE 2 stress analysis by a 30° section, as shown in Figures 4-9, 4-10, and 4-11. The grids were modeled with shell elements, and the stiffening rings and mounting ring were modeled with solid elements. The insulator and spacer were modeled with pipe elements. The grids were attached to the stiffening rings with rigid beams; however, the screen-grid stiffening ring was attached to the mounting ring with rigid beams only at the shoulder (2.4° section of the area). The radial cuts in the mounting ring next to the shoulder were also accounted for in the model.

Symmetry boundary conditions were defined at the cut planes of the 30° section. The center nodes of the accel and screen grid were allowed to move only in the axial direction, and the bottom of the mounting ring was placed on rollers.

Temperatures were specified at 10 grid locations, as shown in Figure 4-12, using temperature data measured at NASA LeRC with thruster hardware representative of the J-series design. The computational model interpolates temperature for locations between the points specified.

The initial objective of the computational analysis was to determine the sensitivity of the structural deformation to the elastic constants that were used to represent the perforated grid material. Table 4-2 lists the values of Young's modulus and Poisson's ratio that were used in computing the cases considered. Case 1 modifies the solid material constants in accordance with a technique derived by O'Donnel and Longer.[4-17] For Case 2, the constants were adjusted for ligament area ratios. Case 3 made use of the constants for solid sheets (without perforation). The centerline displacements of the grids for all the

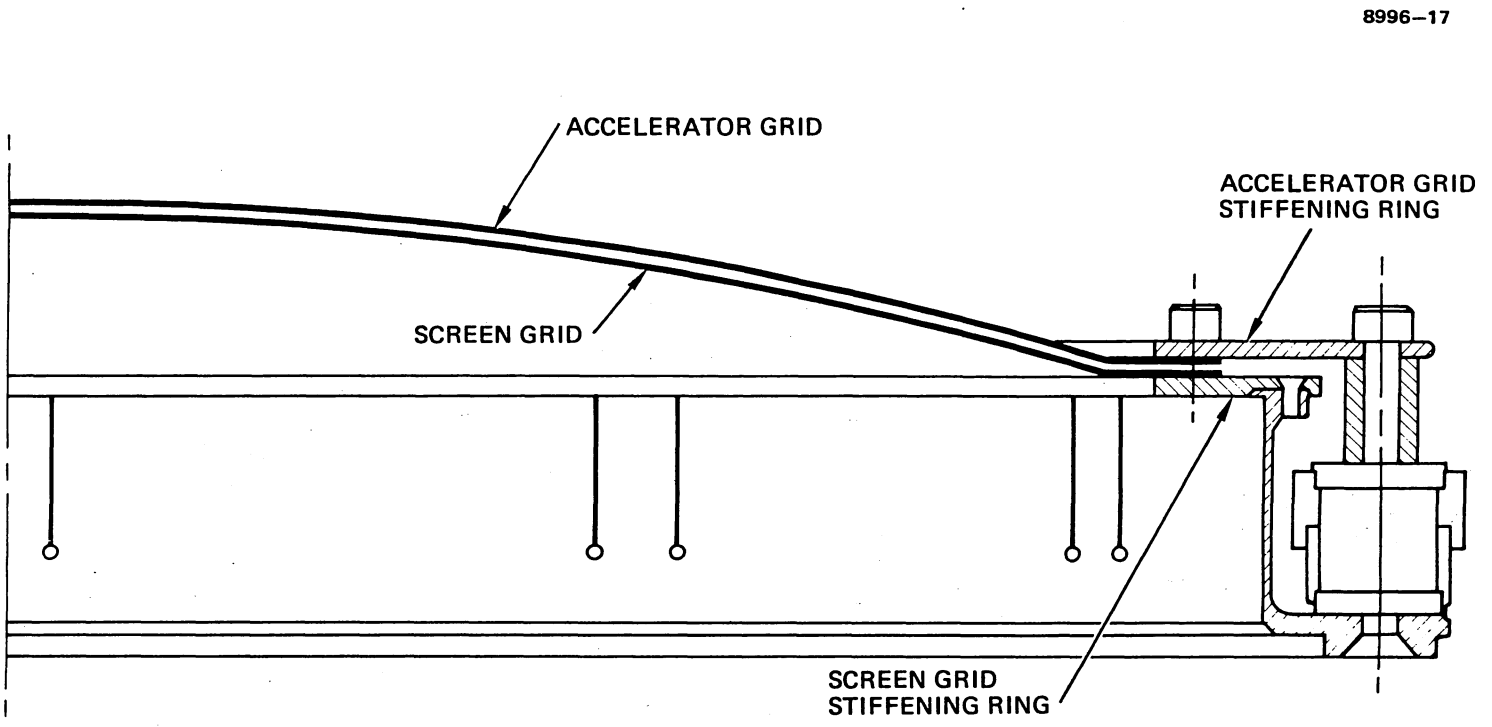

Figure 4-8. Cross section of the ion-accelerator grid assembly for the J-series 30-cm thruster.

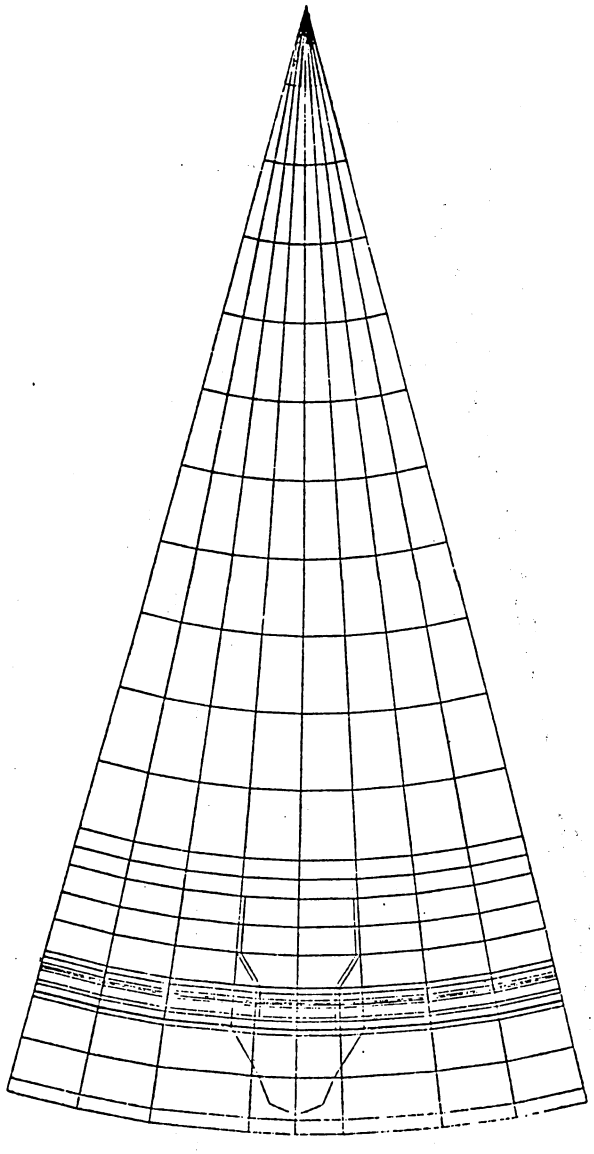

Figure 4-9.
30° sectional model of ion-accelerator grid assembly for EASE 2 analysis (top view).

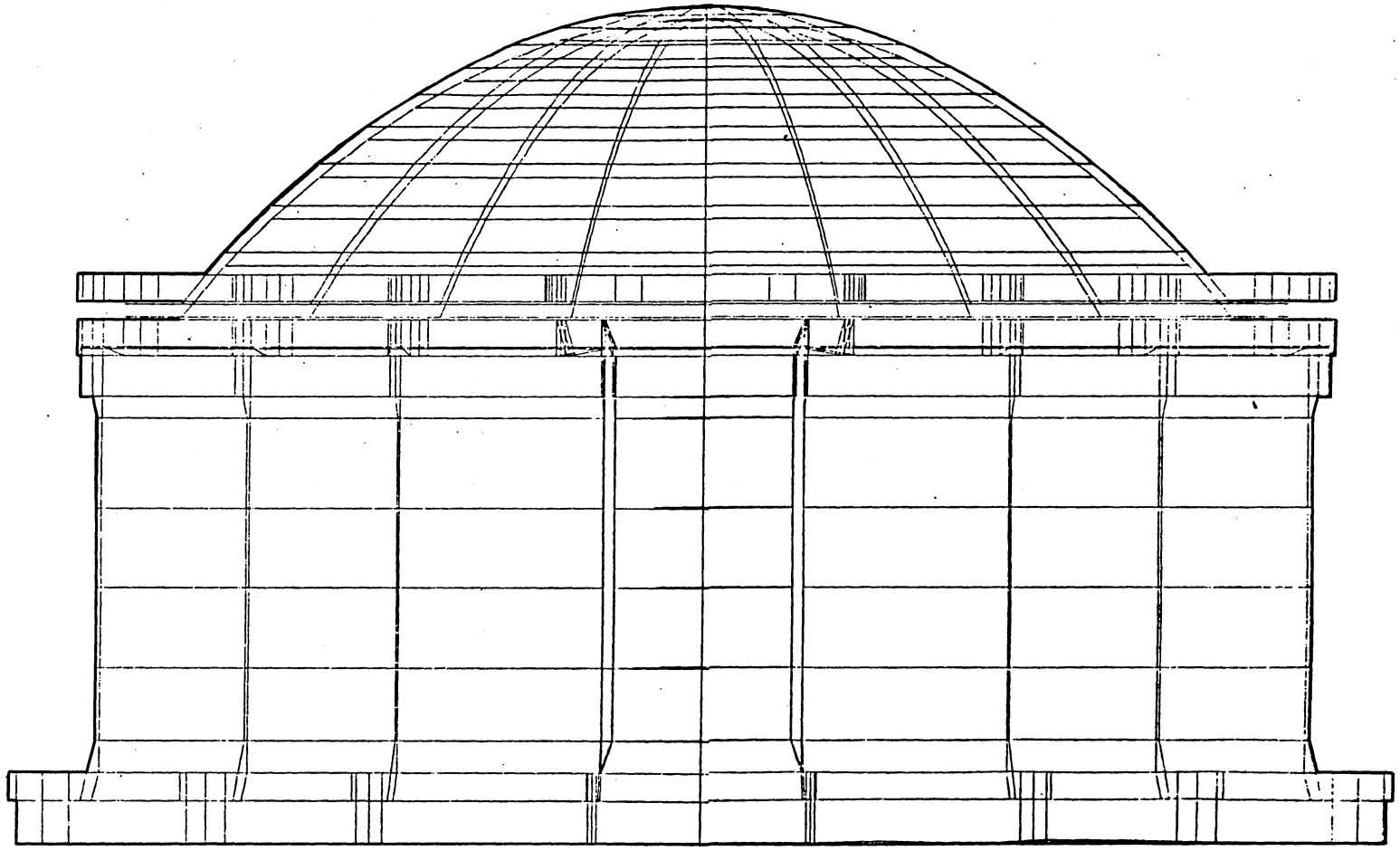

Figure 4-10. 30° sectional model of ion-accelerator grid assembly for EASE 2 analysis (side view).

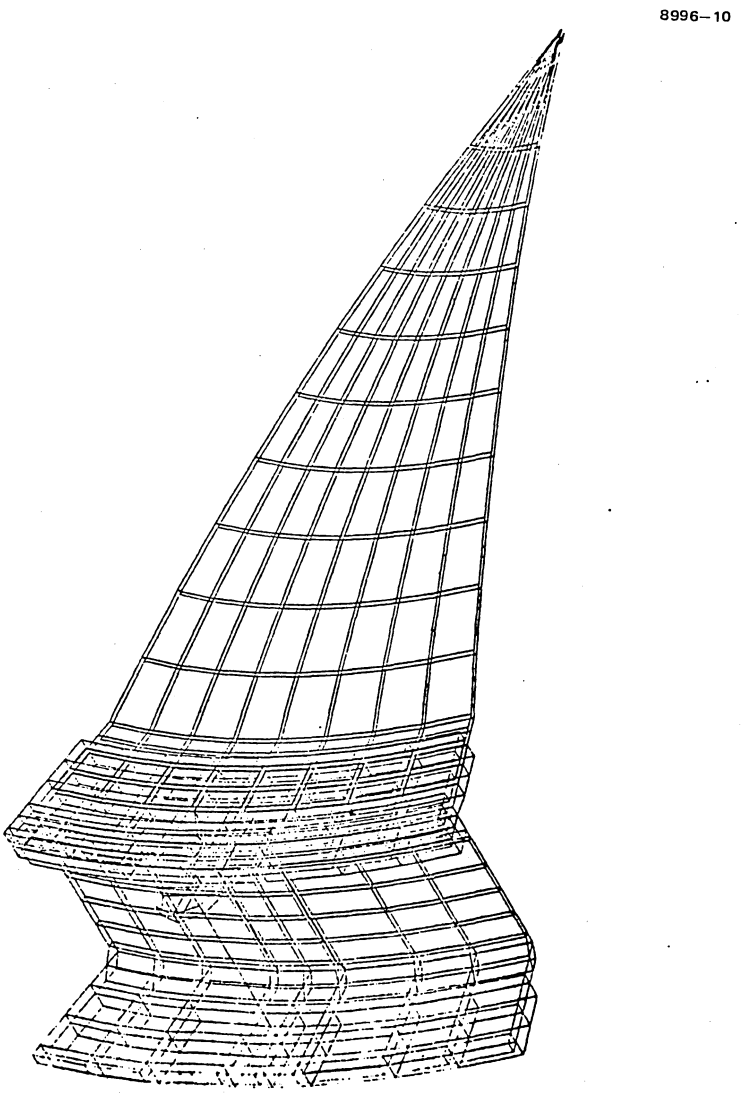

Figure 4-11. 30° sectional model of ion-accelerator grid assembly for EASE 2 analysis (isometric view).

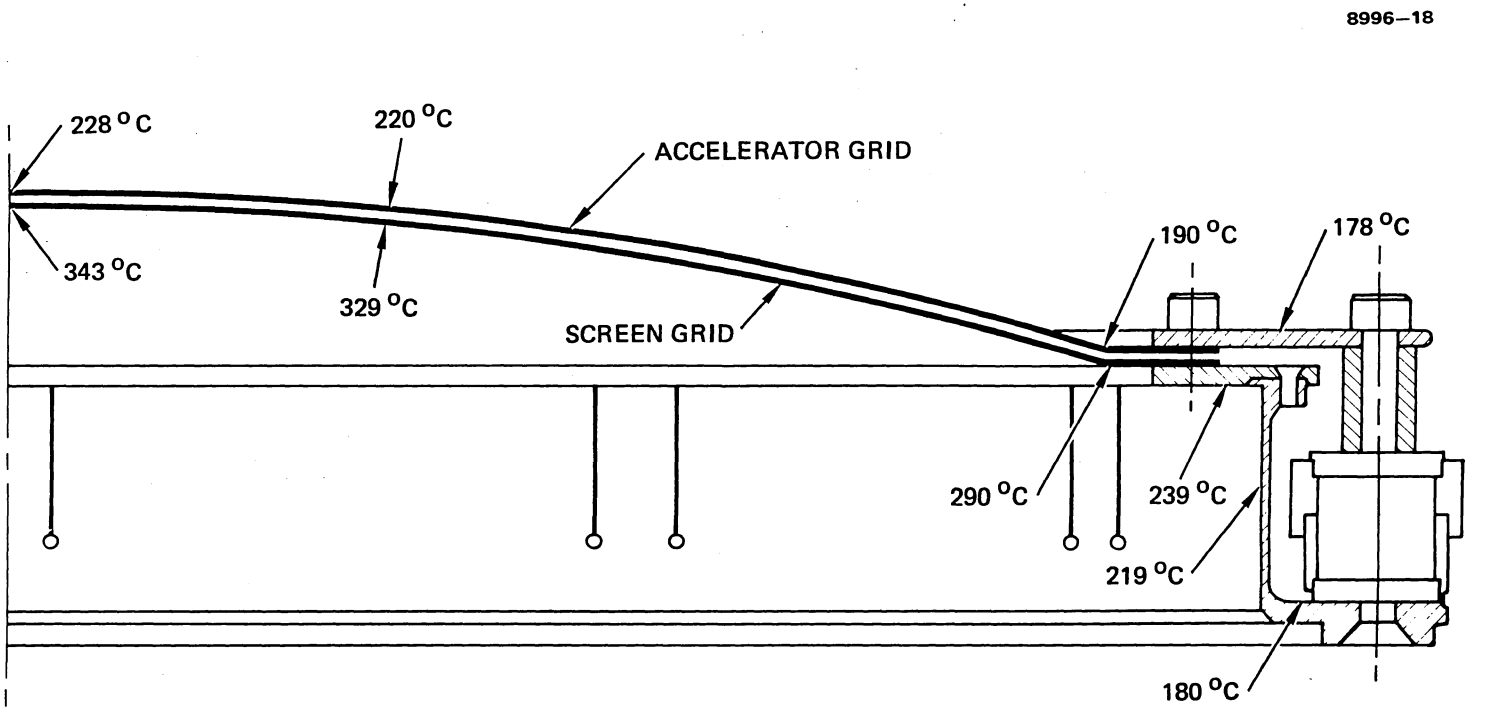

Figure 4-12. Cross-section of the ion-accelerator grid assembly for the J-series 30-cm thruster showing temperatures used in stress analysis.

cases considered are listed in Table 4-3. It is apparent that the values of the elastic constants have very little effect on the displacements. Figure 4-13 shows the structural deformation that occurrred in Case 1 (magnified by a factor of 50). Although it appears that the screen grid and accel grid have crossed over, this is a mis-representation caused by the magnification. The feature of interest here is the bending of the accel-grid stiffening ring. The computations for Cases 2 and 3 showed no change in this bending; in Case 4, the model was changed to assign uniform temperatures of 180°C and 239°C to the accel and screen grid siffening rings (respectively). Again, very little change was noted in the grid deflections or in the structural deformation.

Table 4-2. Elastic Constants Used to Describe Screen and Accel Grids

Case	Accel Grid		Screen Grid	
	Young's Modulus x 10^6	Poisson's Ratio	Young's Modulus x 10^6	Poisson's Ratio
1	17.9	0.34	1.9	0.92
2	26.7	0.32	0.3	0.32
3	47	0.32	47	0.32
4	47	0.32	47	0.32
5	47	0.32	47	0.32

6758

Table 4-3. Deflections of Screen and Accel Grids on Centerline for the Five Cases Considered

Case	Screen, cm (mils)	Accel, cm (mils)	Differential cm (mils)
1	0.0343 (13.5)	0.0028 (1.1)	0.0312 (12.3)
2	0.0322 (12.7)	0.0028 (1.1)	0.0292 (11.5)
3	0.0327 (12.9)	0.0028 (1.1)	0.0297 (11.7)
4	0.0348 (13.7)	0.0030 (1.2)	0.0318 (12.5)
5	0.0345 (13.6)	0.0264 (10.4)	0.0078 (3.1)

6758

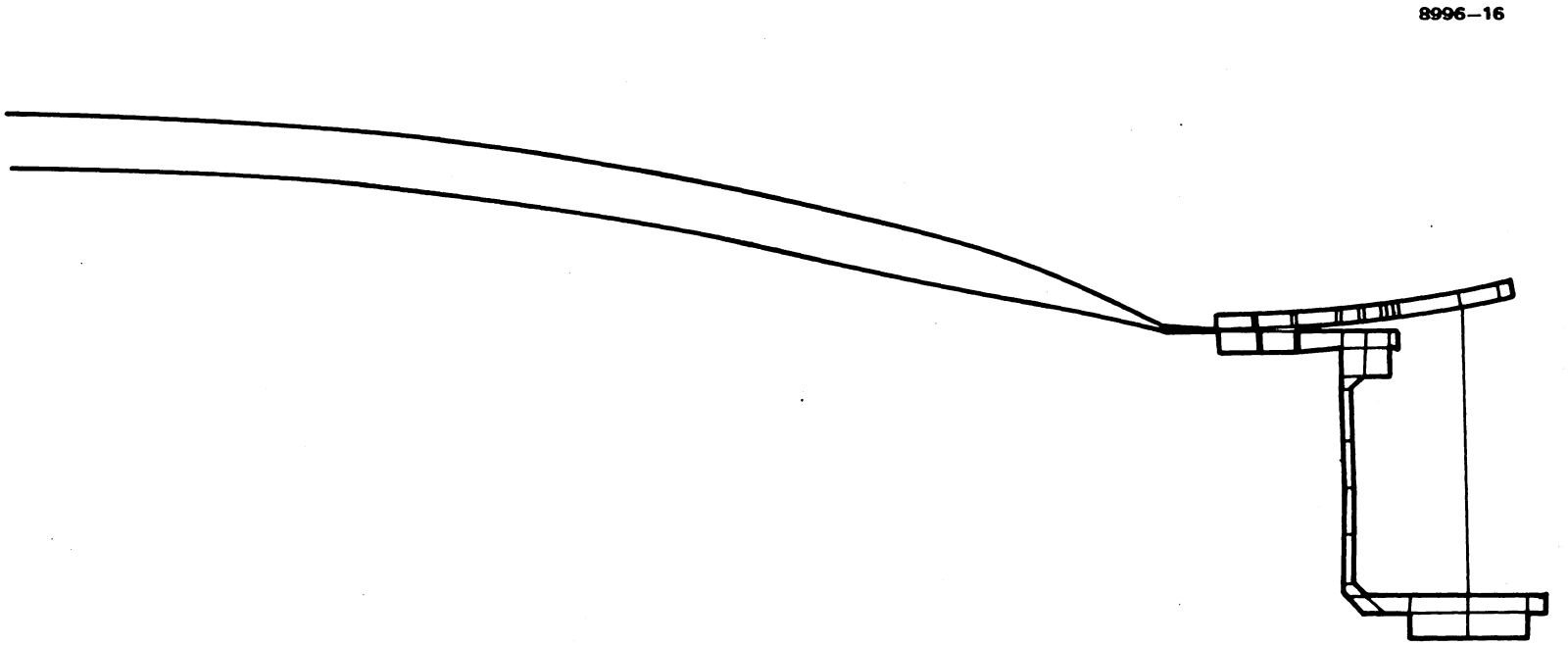

Figure 4-13. Typical structural deformation of the ion-accelerator grid assembly obtained using elastic constants and thermal conditions for Cases 1-4 (magnified by a factor of 50).

We concluded that the deformation of the stiffening ring is a consequence of the bending moment that occurs because of the rigid accel grid support. For Case 5, the pipe elements used to model the accelerator grid spacer were replaced by beam elements that carry only axial loads. The uniform temperatures used for the accel and screen grid stiffening rings were also retained for Case 5. Figure 4-14 shows that the resultant deformation does not bend the accel stiffening ring, and Table 4-3 shows that the relative displacement of the screen and accel grids on centerline is significantly reduced. The results for Case 5 strongly recommend the incorporation of a beam-type accel grid spacer that has very little stiffness in the radial direction.

The time and resources available to this study task had been consumed at the completion of the computations described above. Having the model for describing the variation in ℓ_g with operating conditions, it would now be possible to formulate descriptive models for perveance, backstreaming limit, beam divergence, etc. that could be used to correlate existing data with theoretical expressions. Although refinement of the descriptive models would be verified for analyzing J-series thruster capabilities, Figure 4-14 clearly shows that performance would be significantly improved by modifying the support elements. Consequently, the formulation of models for the purpose of predicting the ultimate limitations of a 30-cm thruster would be more meaningful if the design of the hardware were changed as indicated.

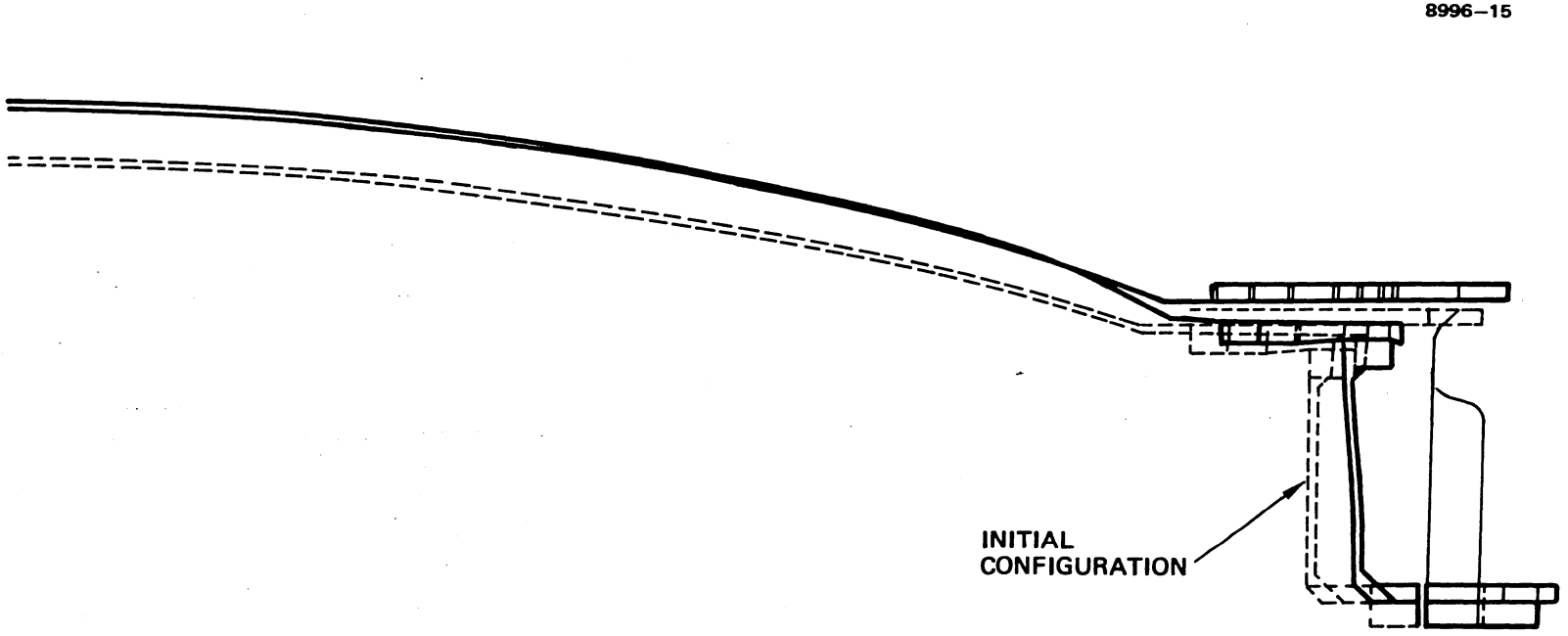

Figure 4-14. Structural deformation of the ion-accelerator grid assembly for the elastic constants and modeling of Case 5 (magnified by a factor of 50).

Page intentionally left blank

REFERENCES FOR SECTION 4

4-1. V.K. Rawlin, "Studies of Dished Accelerator Grids for 30-cm Ion Thrusters," AIAA Paper 73-1086, Lake Tahoe, Nevada, October 1973.

4-2. G. Aston and H.R. Kaufman, "The Ion-Optics of a Two-Grid Electron-Bombardment Thruster," AIAA Paper 76-1029, Key Biscayne, Florida, November 1976.

4-3. G. Aston, "The Ion-Optics of a Two-Grid Electron-Bombardment Thruster," NASA CR-135034, Colorado State University, May 1976.

4-4. H.R. Kaufman, "Accelerator-System Solutions for Broad-Beam Ion Sources," AIAA Journal 15, 7, 1025, July 1977.

4-5. G. Aston, H.R. Kaufman, and P.J. Wilbur, "Ion Beam Divergence Characteristics of Two-Grid Accelerator Systems," AIAA J. 16, 5, 516, May 1978.

4-6. G.A. Meadows and B.A. Free, "Effect of a Decel Electrode on Primary and Charge-Exchange Ion Trajectories," AIAA Paper 75-427, New Orleans, Louisiana, March 1975.

4-7. R.P. Vahrenkamp, "Operation of a 30-cm Ion Thruster with Small-Hole Accelerator Grids," J. Spacecraft and Rockets 14, 10, 587, October 1977.

4-8 P.J. Wilbur, "15 cm Mercury Ion Thruster Research - 1976," NASA CR-135116, Colorado State University, December 1976.

4-9. V.K. Rawlin, "Sensitivity of 30-cm Mercury Bombardment Ion Thruster Characteristics to Accelerator Grid Design," AIAA Paper 78-668, San Diego, California, April 1978.

4-10. H.R. Kaufman, "Technology of Electron-Bombardment Ion Sources," Advances in Electronics and Electron Physics, 36 Acacemic Press, New York, 1974.

4-11. R.L. Poeschel et al., "2.5 kW Advanced Technology Ion Thruster," NASA CR-135076, Hughes Research Laboratories, April 1976.

4-12. R.L. Poeschel et al., "High-Power and 2.5 kW Advanced-Technology Ion Thruster," NASA CR-135163, Hughes Research Laboratories, February 1977.

4-13. R.L. Poeschel et al., "2.5 kW Advanced Technology Ion Thruster," NASA CR-134687, Hughes Research Laboratories, August 1974.

4-14. P.J. Wilbur, "Mercury Ion Thruster Research - 1977," NASA CR-135317, Colorado State University, December 1977.

4-15. V.K. Rawlin, "Performance of a 30-cm Ion Thruster with Dished Accelerator Grids," AIAA Paper 73-1053, Lake Tahoe, Nevada, October 1973.

4-16. R.L. Poeschel and R.P. Vahrenkamp, "High Power Operation of a 30-cm Mercury Bombardment Ion Thruster," AIAA Paper 76-1007, Key Biscayne, Florida, November 1976.

4-17. W.J. O'Donnel and B.F. Langer, "Design of Perforated Plate," ASME J., 1962.

SECTION 5

ISOLATOR DEVELOPMENT

This task, like the cathode lifetime task, builds on the work begun under another NASA program (Contract NAS 3-20395). The high-voltage propellant-flow isolator of interest in this study is based on the approach of dividing the applied voltage across electrically isolated "chambers" in the flow channel so that the voltage drop across any given chamber is below the minimum Paschen-breakdown-voltage. Under the earlier NASA program, we designed an isolator for operation at voltages up to 6 kV and propellant flow rates equivalent to 4 A. An isolator meeting these requirements was fabricated and tested; however, excessive leakage current was observed during an extended test of the isolator. The reasons for the excessive current could not be explored within the scope of that study. Hence the goals for the present study task were to determine those reasons and verify the isolator performance model by demonstrating ultimate breakdown voltage and voltage division across the isolator. An additional goal was to extend isolator performance capability to 10-kV rated voltage and 10-A equivalent propellant flow.

A. HIGH-VOLTAGE ISOLATOR DESIGN

Although the design of this isolator has been described previously,[5-1] a brief description is given here to facilitate discussing the results. The isolator design used in the LeRC/Hughes 30-cm J-series thruster has the vapor flow channel divided into seven chambers. With 1500 V applied, the voltage across any chamber is about 215 V, which is less than the Paschen minimum (~250 V) for mercury (assuming that the voltage divides evenly across each chamber). By increasing the number of chambers to 28, as shown in Figure 5-1, the isolator-voltage rating scales to 6000 V. To keep the high-voltage isolator interchangeable with the J-series design, the isolator envelope and alumina body dimensions were maintained exactly the same as the design used in the LeRC/Hughes 30-cm J-series thruster. Consequently, the internal alumina spacer had to be changed to the design shown in Figure 5-2 to accomplish the voltage scaling.

6268-3R1

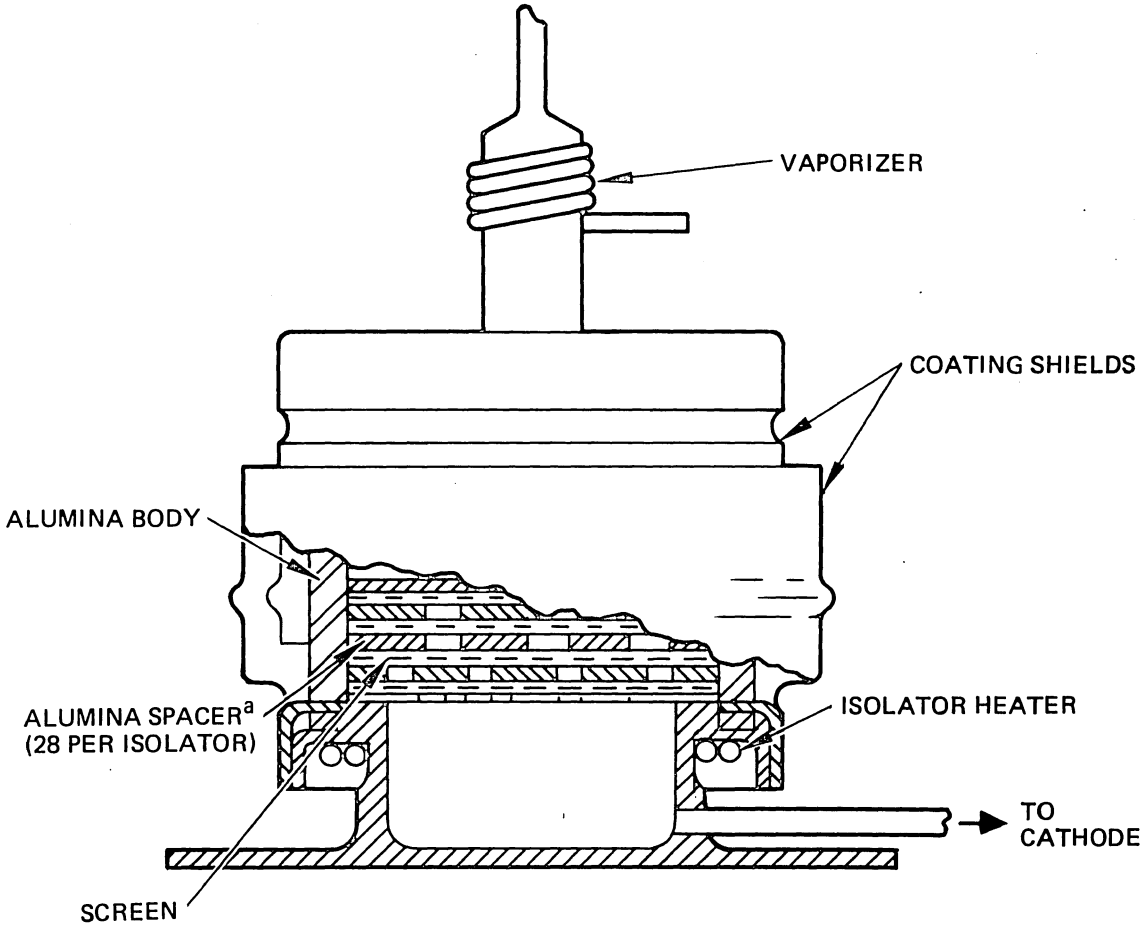

[a]ALUMINA SPACERS 0.65 mm (0.025 in.) THICK (SEE FIGURE 5–2)

Figure 5-1. High-voltage propellant electrical isolator using multi-chamber design concept (internal scaling).

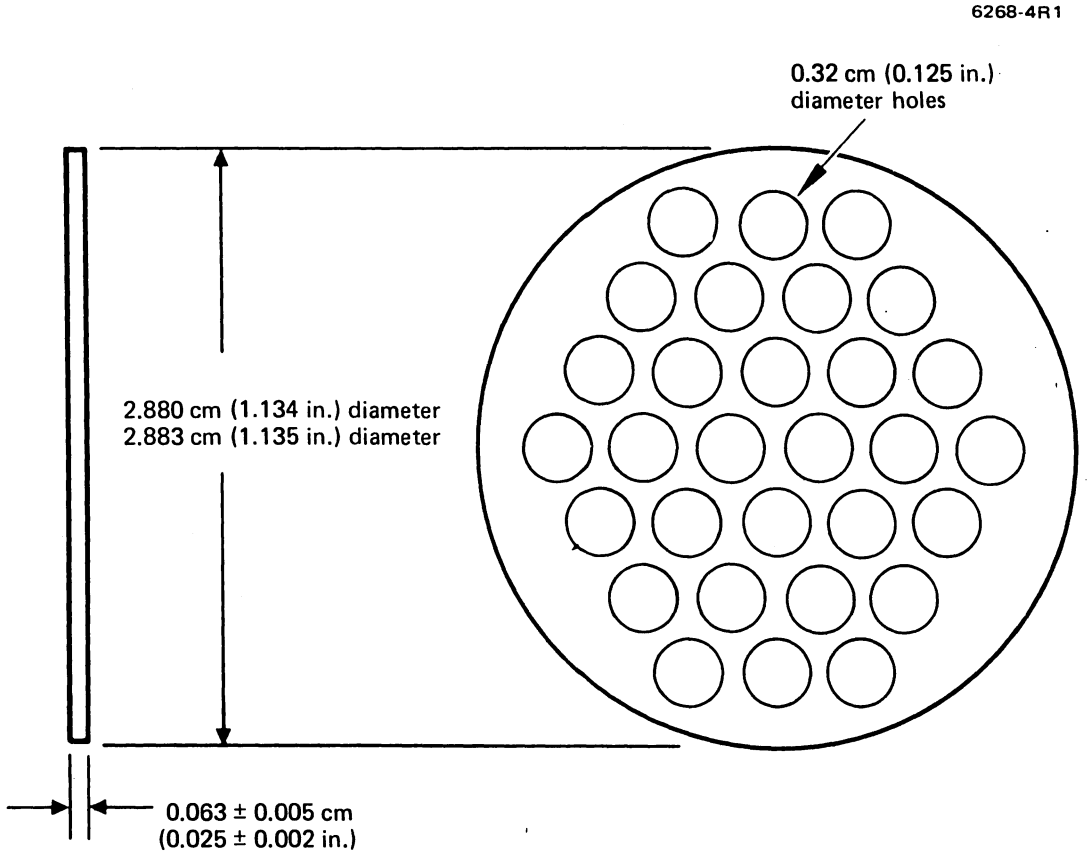

Figure 5-2. Alumina spacer for the 28-chamber isolator.

B. DESCRIPTION OF ISOLATOR TEST AND RESULTS

Isolator-leakage and breakdown-voltage tests were performed with circuitry like that shown in Figure 5-3, and initial testing was performed to determine the cause of the leakage current behavior shown in Figure 5-4 (from Ref. 5-1). The same isolator that was tested under contract NAS 3-20395 was re-evaluated by measuring leakage current as a function of applied voltage. Figure 5-5 shows that the leakage current was still of the same order of magnitude although somewhat lower than in the earlier tests. We thought at the time that the excessive leakage current (5 to 10 nA was typical) was caused by contamination of the outer surface of the isolator ceramic from sources originating within the vacuum test facility, similar to that observed and reported[5-2] during the development of isolator technology for the LeRC/Hughes 30-cm thrusters. The protective shields were removed from the isolator, and, although no discoloring of the ceramic isolator body was evident, the isolator was cleaned by grit blasting. After this surface cleaning, the isolator was reinstalled in the test facility, and the voltage/current tests were repeated. The results were identical to those shown (for this program) in Figure 5-5. After ensuring that no other source of leakage or circuit errors could be responsible for the leakage current observed, the isolator was disassembled, and the ceramic spacers were found to be contaminated.

Several potential sources of contamination were identified, but each was ultimately rejected and, as a result, no conclusive evidence could be found to verify the source of contamination. Several types of chemical and spectroscopic analyses of the contaminated ceramic spacers revealed that the major percentage of foreign constituents was carbon. A carbon coating would readily explain the resistive characteristic of the current leakage shown in Figure 5-5, and the change in resistance with mercury flow is probably a consequence of the increased vaporizer temperature (which also increases the isolator temperature).

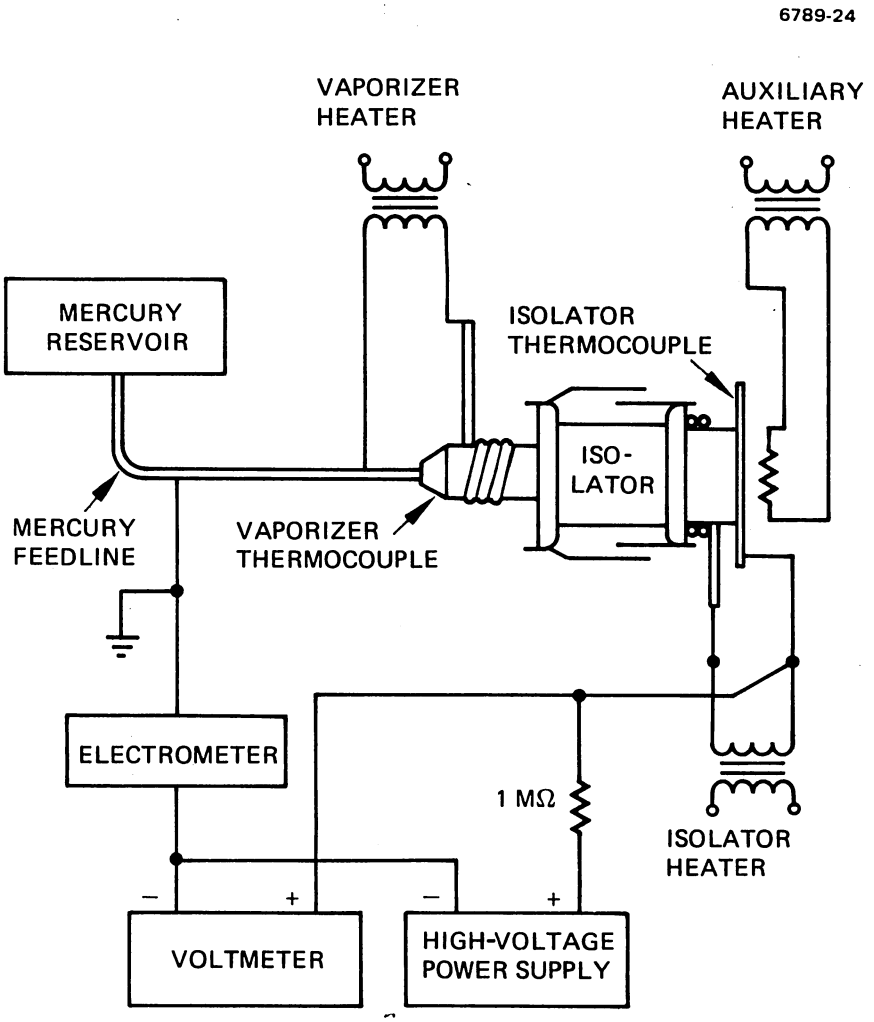

Figure 5-3. Schematic of high-voltage propellant-isolator test apparatus.

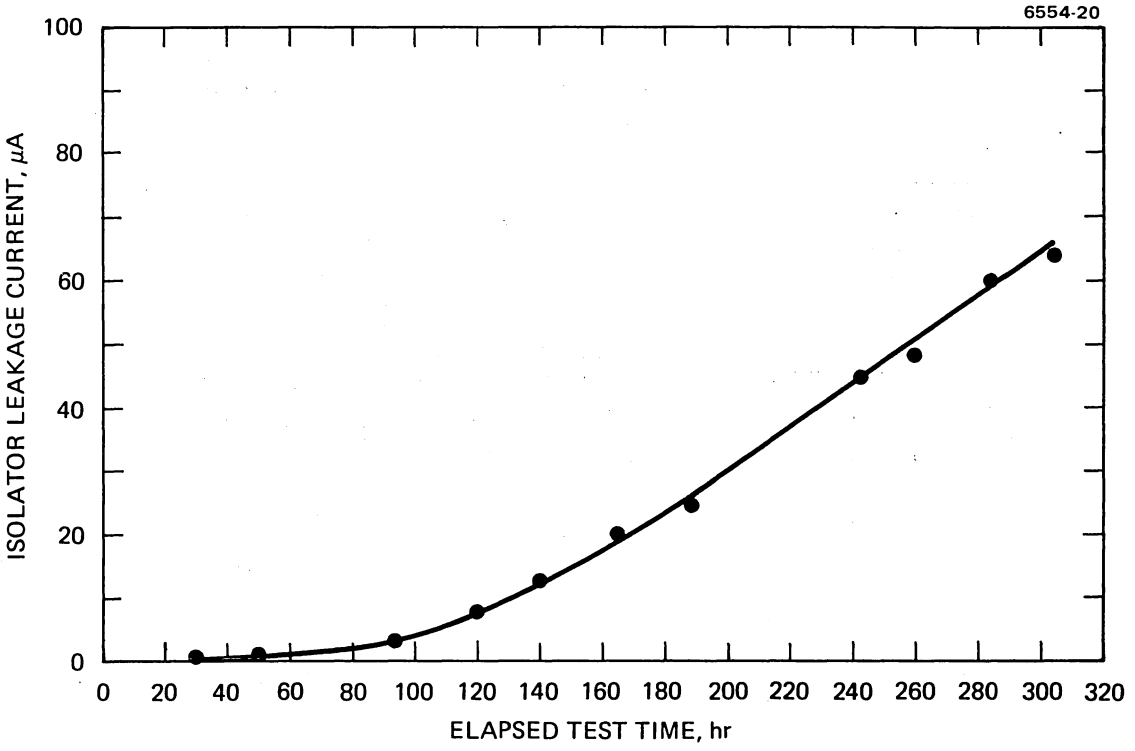

Figure 5-4. Isolator leakage current versus elapsed test time for the multisection isolator design shown in Figure 5-1. (This isolator was later found to be contaminated.)

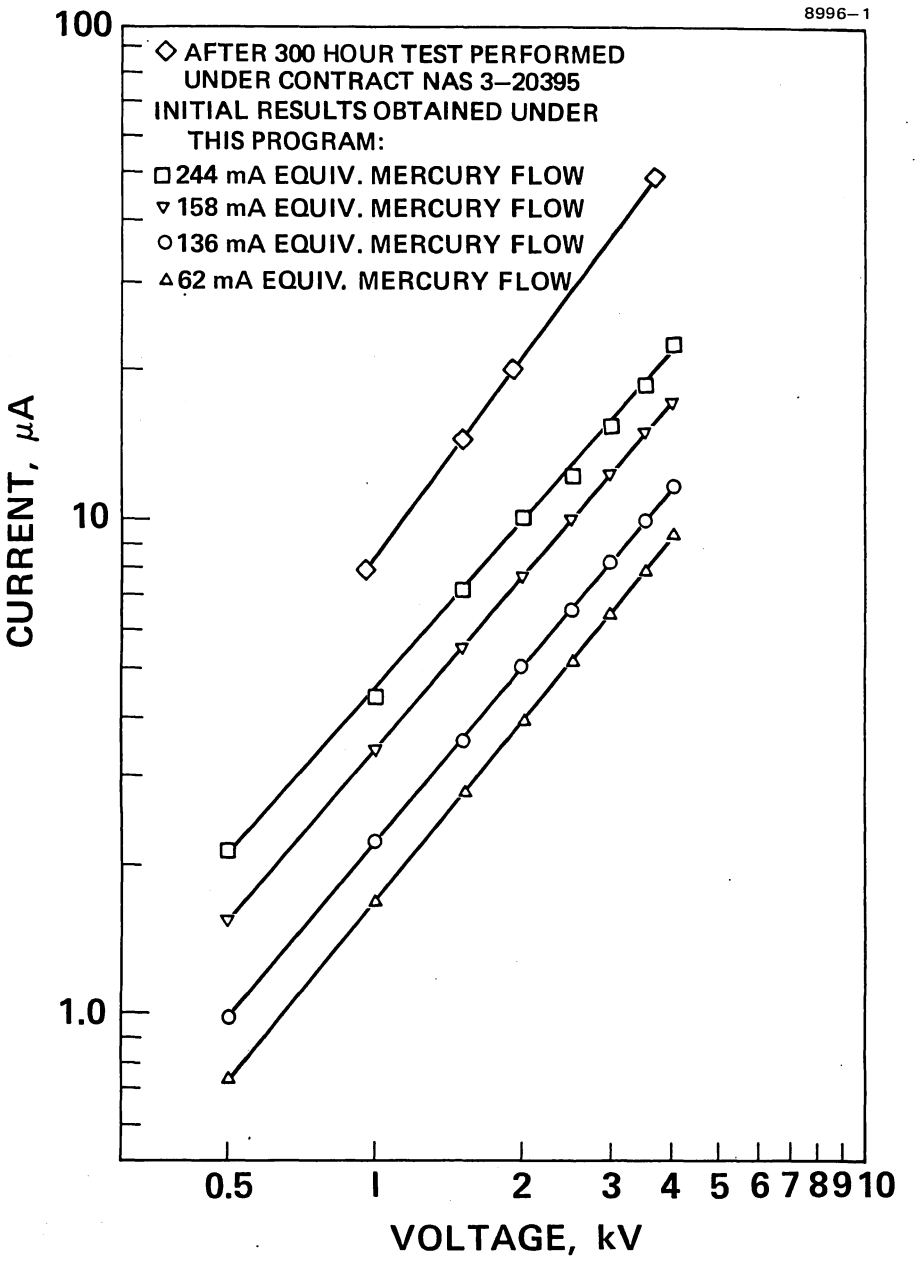

Figure 5-5. Comparison of leakage current versus voltage for test performed after 300-hr test and for initial tests performed under this program. (This isolator was later found to be contaminated.)

In checking assembly procedures and assembly documentation, nothing was found to indicate any abnormalities during fabrication of the isolator, and samples of the ceramic spacer were cleaned by different methods and then analyzed to determine whether any alteration of the cleaning procedure might result in excessive carbon. This comparison of cleaning procedures showed no measurable change in the purity of the samples. Since (1) the alumina used in the spacers is as pure as any alumina available commercially including the type used for the isolator body (AL300) and (2) isolator fabrication and cleaning procedures as documented for the LeRC/Hughes 30-cm J-series thruster design are satisfactory for removing contamination from ceramic surfaces, we concluded that the observed contamination of the high-voltage isolator was an anomalous event. It may be necessary to formulate more precise specifications on storage of isolator parts and/or finished isolators to prevent anomalous contamination from recurring.

To verify that the spacer contamination was an anomalous event, the isolator body was cleaned and fitted with a new set of spacers, which had been cleaned in accordance with the documented fabrication procedures and then hydrogen fired to remove any possible residue of cleaning solutions. The rebuilt isolator was then placed in test with mercury flowing at an equivalent rate of 100 mA (corresponding to a vaporizer temperature of 340°C and an applied voltage of 4 kV). This test was continued for a total of 1648 hr with no increase in leakage current. (The leakage current fluctuated more or less randomly between 5 nA and 10 nA.) These test results demonstrate that the high-voltage design meets the objectives for the intended operating conditions.

The next parameter investigated was the breakdown voltage of the isolator. The test circuit was modified by inserting a series current-limiting resistor (100 MΩ) to prevent damage to either the isolator or the power supply, and the applied voltage was increased until an increase in leakage current was observed (as shown in Figure 5-6). The isolator was tested first with mercury propellant (100 mA equivalent flow) and then with argon (100- to 300-mA equivalent flow) using the vaporizer as a flow-limiting impedance. The current rise, or breakdown, repeatedly was in the 8.3 kV to 8.6 kV range for both gases. This "breakdown" was not

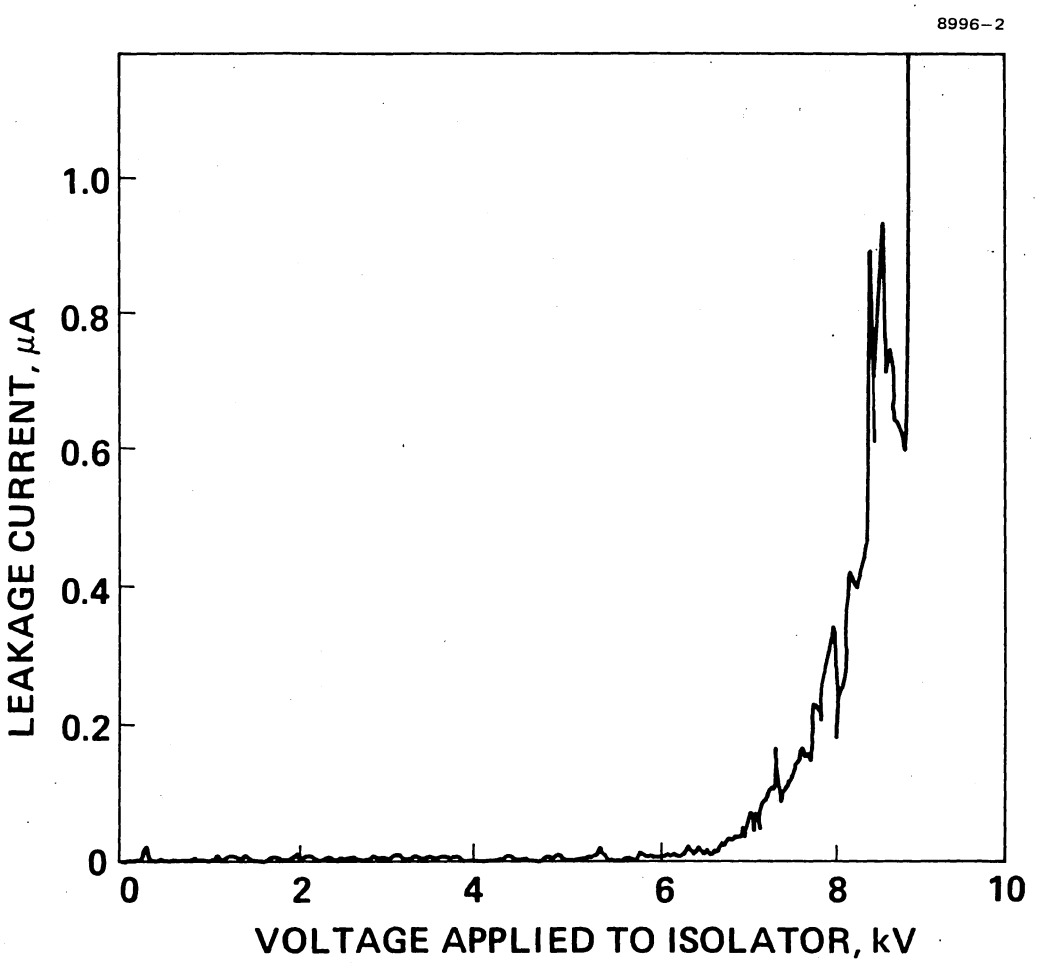

Figure 5-6. Continuous recording of isolator-leakage current preceding high-voltage breakdown for argon gas.

dependent on isolator temperature or propellant flow. The systematic check of the wiring, vacuum feedthroughs, etc. that we conducted led to the conclusion that the breakdown must occur between the isolator shields. The isolator shields were removed, and the isolator was tested with argon propellant to 12 kV without breakdown (no current rise). Higher voltages were not applied because of test-facility limitations (vacuum feedthroughs, etc.). We concluded that the high-voltage-breakdown limit of the isolator itself is well above the design value but that the isolator shields are designed for a 2-kV applied voltage and can only be used up to about 8 kV. For 10-kV operation, a redesign of the shields would be necessary.

The way in which the applied voltage is divided across the seven chambers was also investigated under this program. We constructed a special isolator (shown in a schematic in Figure 5-7 and in a photograph in Figure 5-8) that enabled us to measure the potential of each of the screens that form the chamber boundaries. Initially, the isolator was designed to measure the potential of every fourth screen in the 28-chamber design. When the purity of the thin ceramic spacers was in doubt, the design was modified to have only seven spacers, and hence the design is directly representative of the LeRC/Hughes J-series thruster.

The first technical challenge presented in obtaining the voltage-division measurement was in fabricating an isolator having electrical connections that contact the wire mesh under the constraint that all possibilities for contaminating the ceramic insulator had to be avoided. The next challenge was to find a measurement technique that did not influence the voltage division. Figure 5-9 shows the measurement circuit with the isolator represented by an equivalent resistive network. Since the value of each resistor in this network is estimated to be $\sim 10^{11}\ \Omega$, the input impedance of the measuring circuit must be extremely high ($\sim 10^{14}\ \Omega$). An electrostatic voltmeter was selected for this measurement because it couples capacitively to the point of measurement, and hence no steady-state current is drawn and the input impedance is essentially infinite.

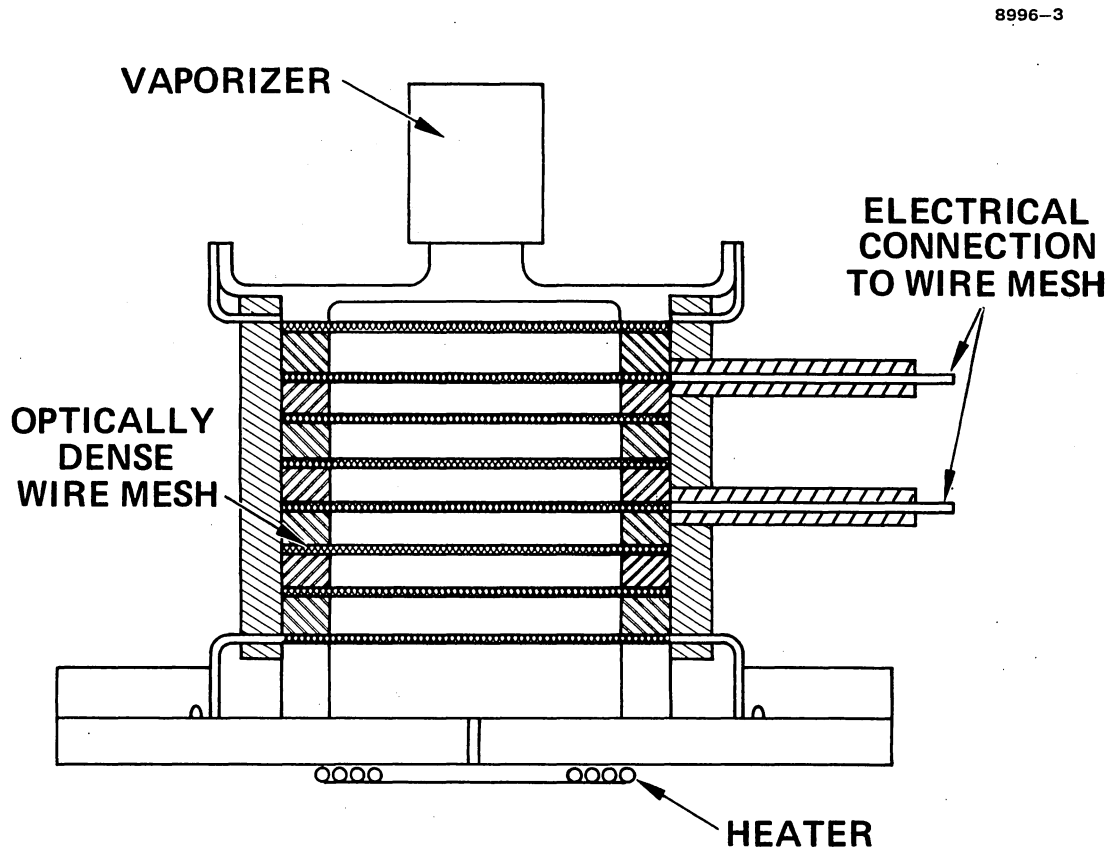

Figure 5-7. Schematic of special isolator used for measuring voltage division across the isolator chambers.

M12823

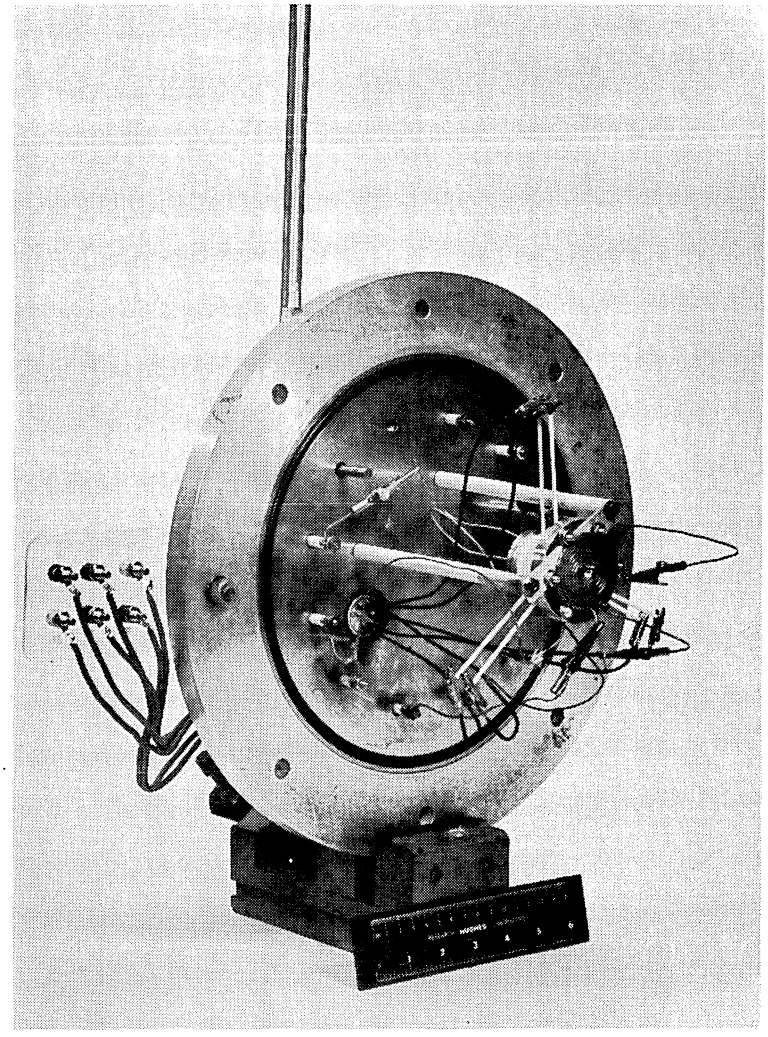

Figure 5-8. Photograph of the demountable isolator with electrical connections for each wire mesh.

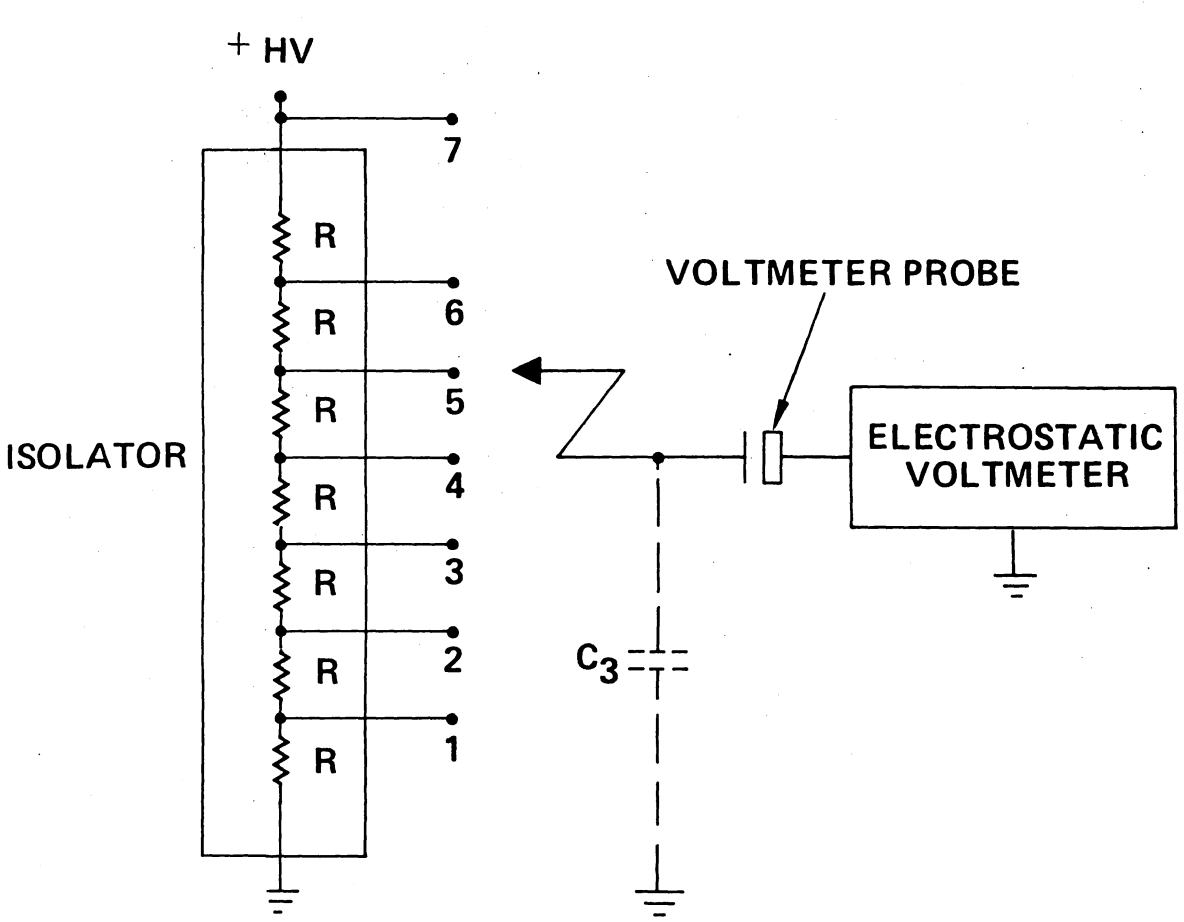

Figure 5-9. Schematic of isolator (initial concept) and voltage-division measurement circuit.

The initial voltage measurements obtained with this circuit were somewhat difficult to understand. The voltage measured at any given test point was more dependent on the technique for connecting the electrostatic voltmeter probe adapter to the point of measurement than on the propellant-flow or isolator-temperature conditions. By discharging the effective probe-adapter capacity and grounding all the test points, uniform initial conditions were established for measurement at each test point. The probe adapter was then connected to the test point of interest, and the voltage was applied across the isolator. The voltage drops across the isolator chambers were then determined by measuring the voltage from each test point to the isolator ground to obtain a characteristic such as the one shown in Figure 5-10. Even with this technique, the voltage division was still independent of propellant flow, isolator temperature, and isolator polarity (that is, the isolator could be connected in the circuit with the vaporizer end positive and the other end grounded without changing the voltage division). This eventually led to identifying an equivalent circuit for the isolator, as shown in Figure 5-11. Analyzing the data shown in Figure 5-10 using this circuit diagram yields

$$C_1 = 0.3\ C_2 \tag{5.1}$$

$$C_3 = 0.18\ C_2 \quad . \tag{5.2}$$

Calculating the voltage of the intermediate measurement points based on this equivalent circuit produced the theoretical curve shown in Figure 5-10, which is in good agreement with the intermediate experimental points. Consequently, we concluded, initially at least, that the internal voltage division is determined by capacitive, rather than resistive, behavior. The question remains as to how representative this result is for long-term steady-state isolator operation since the resistance of internal surfaces may be reduced by some form of contamination. An attempt to model isolator characteristics to account for modified resistance would be extremely speculative without more

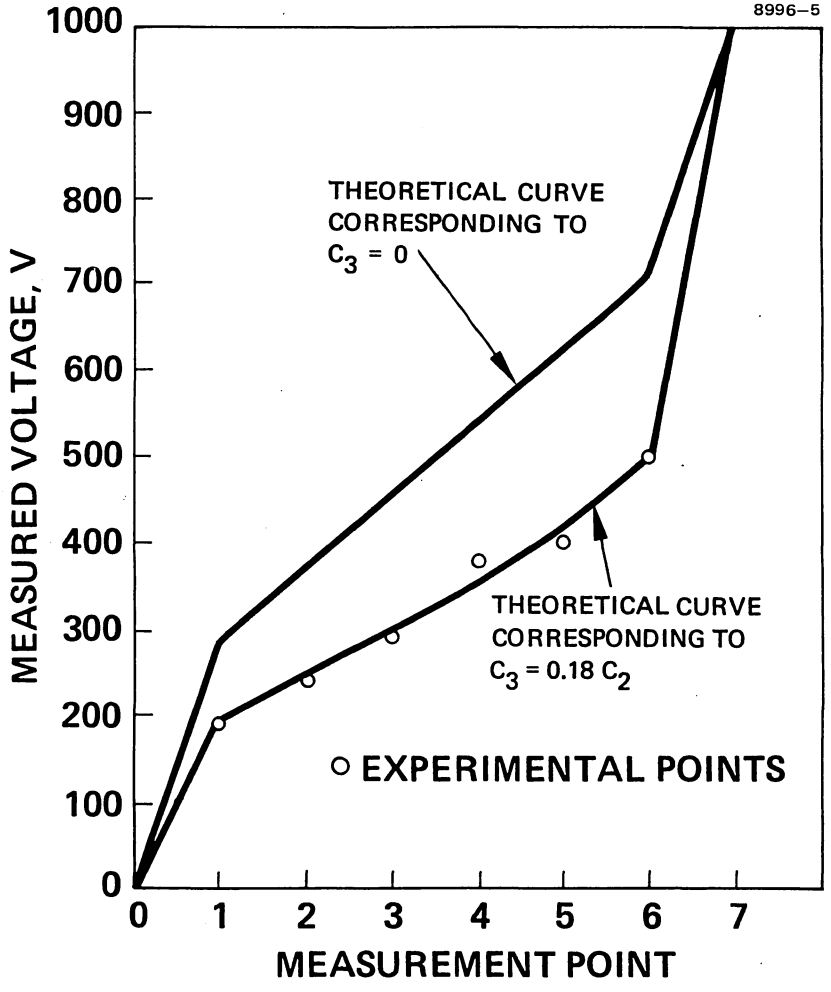

Figure 5-10. Comparison of measured voltage points with theoretical voltage-division curve based on the circuit diagram shown in Figure 5-11.

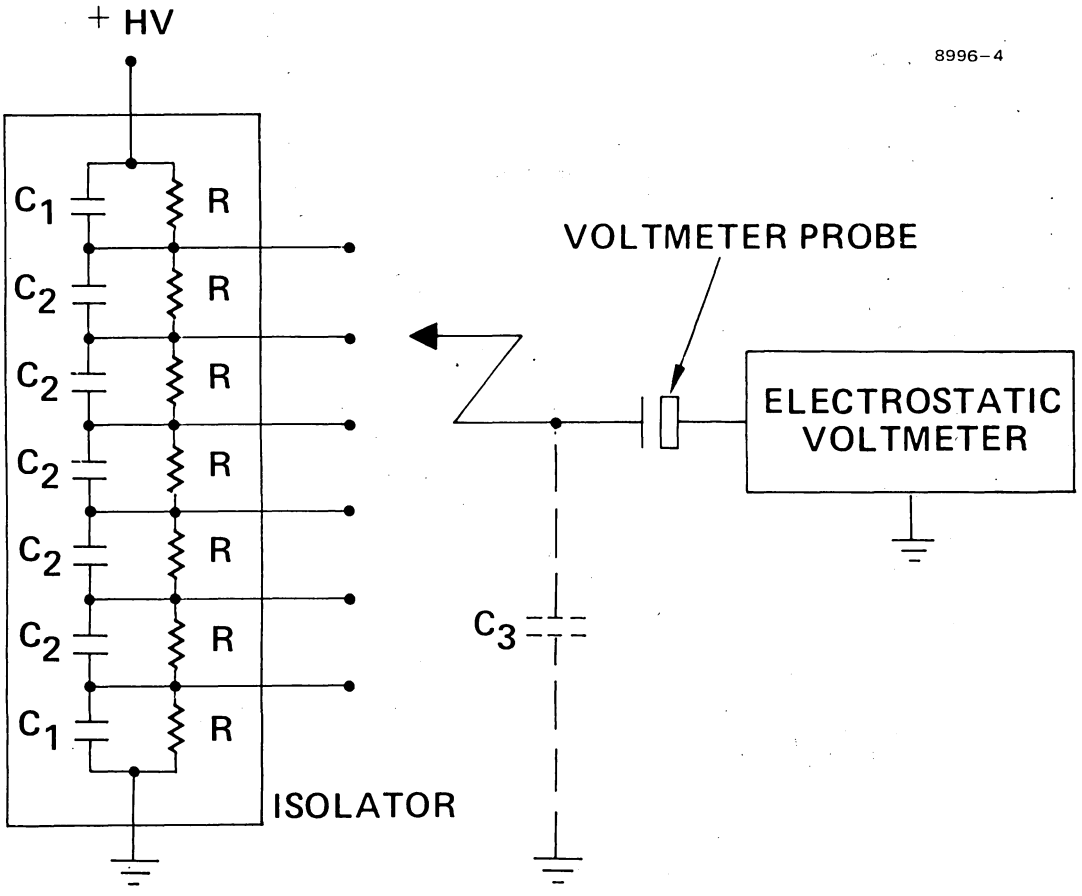

Figure 5-11. Schematic of measurement circuit and equivalent circuit for isolator required to interpret voltage measurements.

information about the type of surface modification that can be expected under "typical" conditions. This measurement also leads to the conclusion that the observed leakage current probably flows on the external surface of the isolator and that the observed propellant flow effect on leakage current (below breakdown) is more accurately a temperature effect.

C. ISOLATOR PERFORMANCE MODEL

In the preceding section, the design of the high-voltage isolator and the measured performance characteristics were discussed in detail. A model for design and performance of a propellant electrical isolator has been formulated on the basis of these results and is discussed below. The model is based on two major assumptions:

- Isolator voltage rating is determined by the Paschen breakdown minimum (modified by geometry effects).
- Voltage division across isolator chambers is a capacitive effect.

The minimum breakdown voltage for mercury vapor can be expressed by[5-3]

$$V_{min} = 282 + 20 \frac{d}{D} \quad , \tag{5.3}$$

where D is the diameter of the isolator channel, and d is the spacing between the wire mesh discs that form the multiple chamber boundaries. For the LeRC/Hughes J-series thruster isolator, D = 2.22 cm (0.875 in.) and d = 0.32 cm (0.125 in.), yielding a V_{min} = 285 V. For the high-voltage isolator design, D = 1.74 cm (0.685 in.) and d = 0.064 cm (0.025 in.), yielding V_{min} = 283 V.

The isolator voltage rating is determined by the total applied voltage that produces a voltage across any of the isolator chambers equal to V_{min}. On the basis of capacitive voltage division and assuming the equivalent circuit shown in Figure 5-11, the voltage across the end two chambers is greater than for other chambers. Equating the

voltage across these chambers to V_{min}, the following relationship was derived for determining the total voltage V_T that can be safely applied to the isolator:

$$V_T = 2\ V_{min} \left[1 + \frac{(n-2)C_1}{2C_2} \right] , \qquad (5.4)$$

where n is the total number of chambers in the isolator. Substituting $C_1 = 0.3\ C_2$ into Eq. 5.4 to compute the maximum voltage yields $V_T \leq 998$ for the J-series-thruster isolator design and $V_T \leq 2773$ for the high-voltage isolator design. Since these values are significantly less than the typical breakdown values measured with either the J-series or the high-voltage isolator design, using $C_1 = 0.3\ C_2$ in Eq. 5.4 is probably not justified for modeling the isolator design. Moreover, the capacitive model requires the values of R (identified in Figure 5-11) to be very large ($\sim 10^{11}\ \Omega$), which may not be the case for all isolator test samples. The applicability of Eq. 5.3 is also open to question since it is based on data obtained with a liquid-mercury pool as one of the electrodes. Values of V_{min} that are both higher and lower than those predicted by Eq. 5.3 can be found in the literature.

On the basis of the data available, it is concluded that isolator phenomena are reasonably well understood, and that minimum, conservative isolator capabilities can be described by Eqs. 5.3 and 5.4, with the provision that the ratio of C_1/C_2 can be specified. The greatest uncertainty lies in knowing whether the model represents typical operation of an isolator after many hours of operation (because of the potential for contamination by the propellant throughput). The measured breakdown of this isolator design was greater than 10 kV, which exceeds the goal, and there was no indication that propellant flow has any effect on the voltage rating. Achieving 10-A equivalent propellant flow to prove this point was not attempted. However, the internal isolator gas pressure required to establish 100 mA equivalent propellant flow through a cathode orifice is greater than the internal pressure required to conduct 10-A equivalent propellant flow directly into a relatively high-conductance

propellant distribution plenum. Consequently, the goals of the task are satisfied by the results discussed here.

Page intentionally left blank

REFERENCES FOR SECTION 5

5-1. R.L. Poeschel and E.I. Hawthorne, Vol. IV, "Thruster Technology Evaluation," Final Report NASA CR-135281, September 1978.

5-2. M.A. Mantenieks, "Status of 30 cm Diameter Mercury Ion Thruster Isolator Development," AIAA Paper 76-1027, 12th International Electric Propulsion Conference, Key Biscayne, Florida (1976).

5-3. D. Smith and D.E. Davies, "International Conference on Ionization Phenomena in Gases, 2, Centre d Etudes Nucleaires, Paris, 1963, pp. 213-216.

Page intentionally left blank

SECTION 6

CONCLUSIONS

A considerable base of information was generated under this study that should aid in the understanding of mercury-ion-thruster operation, testing requirements, lifetime limitations, and ultimate performance capabilities. Several conclusions were drawn from the Task 1 study:

- Thruster test facilities must maintain ambient gases on the order of 10^{-5} Pa (10^{-7} Torr) pressure or below to obtain valid wear-rate measurements.
- Wear rate is very sensitive to factors affecting the formation of doubly charged ions and to the energy of the ions doing the sputtering.
- The use of niobium for fabricating critical chamber components such as the screen electrode could extend the lifetime of the 30-cm thruster.
- Small-hole accelerator grids modify discharge-chamber plasma processes and reduce double ionization (as compared to large-hole accelerator grids operated at the same propellant utilization efficiency).
- An improvement in discharge-plasma uniformity can be achieved with a single-cusp magnetic field geometry, which should, in turn, improve the screen-grid lifetime.

The major conclusions from the Task 2 study were that:

- The barium-aluminate-impregnated porous-tungsten insert can dispense barium for over 50,000 hr at nominal 30-cm-thruster emission currents.
- The results obtained in cathode bell-jar tests that duplicate the discharge-voltage and discharge-current conditions of thruster-operated cathodes should be applicable for describing thruster cathode phenomena.

The Task 3 study produced the following conclusions:

- The important performance parameters cannot be predicted without analyzing the structural deformation of the accelerator grids.
- The LeRC/Hughes J-series-thruster ion-accelerator-grid support assembly is not yet optimal for maintaining minimum deformation.
- The structural-analysis model of the electrode system under thermal stress should be verified experimentally before design optimization is begun.

The Task 4 study showed that:

- The high-voltage propellant-flow-electrical-isolator design can meet performance goals of up to 10-kV applied voltage if the protective shields are redesigned.
- To achieve a predictable voltage distribution across the isolator, (1) the spacers will have to be made predictably resistive or (2) the capacitance from chamber-to-chamber will have to be designed to be equal (accounting for fringe fields).
- Modeling of ultimate breakdown capability requires a measurement of the minimum breakdown voltage for a "typical" isolator chamber with wire-mesh boundaries and ceramic spacers.

APPENDIX A

QUADRUPOLE RESIDUAL GAS ANALYZER CALIBRATION

The discharge-chamber and screen-grid erosion investigation required partial-pressure measurements of various test gases. A quadrupole residual gas analyzer was selected for performing these measurements as well as for determining the relative abundance of residual gases in the HRL 9-ft vacuum chamber. However, since the quadrupole is normally used for relative density measurements, it was necessary to calibrate this instrument for use in obtaining quantitative pressure data. This section describes the calibration procedure and presents representative test results.

A. CALIBRATION PROCEDURE

In the first calibration step, the quadrupole is placed in the scan mode, and a trace of the quadrupole collector current versus mass number is recorded on an x-y recorder. In the next step, the precision leak valve is adjusted to produce the desired chamber pressure (near the maximum calibration pressure), and another scan is recorded. Comparing the two curves verifies that the only mass peaks that changed appreciably are those corresponding to the test gas admitted. A comparison of this type verifies that no extraneous gases are introduced into the vacuum system when the leak valve is opened. In the final calibration step, the quadrupole is placed in the manual mode and adjusted to the mass peak of interest. At this point, the resolution setting is reduced to provide a broader mass peak, thereby rendering the instrument less sensitive to small excursions about the center of mass and resolution settings. Next, the precision leak valve setting is varied and the quadrupole output current is recorded as a function of the ionization-gauge output. This procedure is repeated at least four times, and the resulting calibration data are used to compute an average sensitivity (slope of the calibration curve). For molecular gases, two mass peaks are calibrated corresponding to atoms and molecules of the test gas.

B. RESULTS

Calibration curves are presented in Figure A-1 for carbon monoxide, mass 28. Similar curves were measured for argon, methane, cyanogen, carbon dioxide, water, nitrogen, and oxygen. The curves — plots of quadrupole collector current versus ionization-gauge output — are linear over the pressure range of interest. The slope of the calibration curves represents the sensitivity of the analyzer to the particular mass peak and is typically on the order of 10^{-5} A/Pa (10^{-3} A/Torr). The repeatability of the calibration data is clearly indicated in Figure A-1, where the current origin of curves b through e has been displaced to permit plotting of five separate calibration curves.

Since the analyzer current is linear and must vanish at zero partial pressure, the partial pressure p of the test gas can be calculated using the expression

$$p = \left[\frac{dI}{dP}\right]^{-1} I \ , \qquad \text{(A-1)}$$

where dI/dP is the slope of the calibration curve, I is the quadrupole collector current, and P is the total pressure indicated by the ionization gauge, using a gauge sensitivity appropriate to the particular test gas.

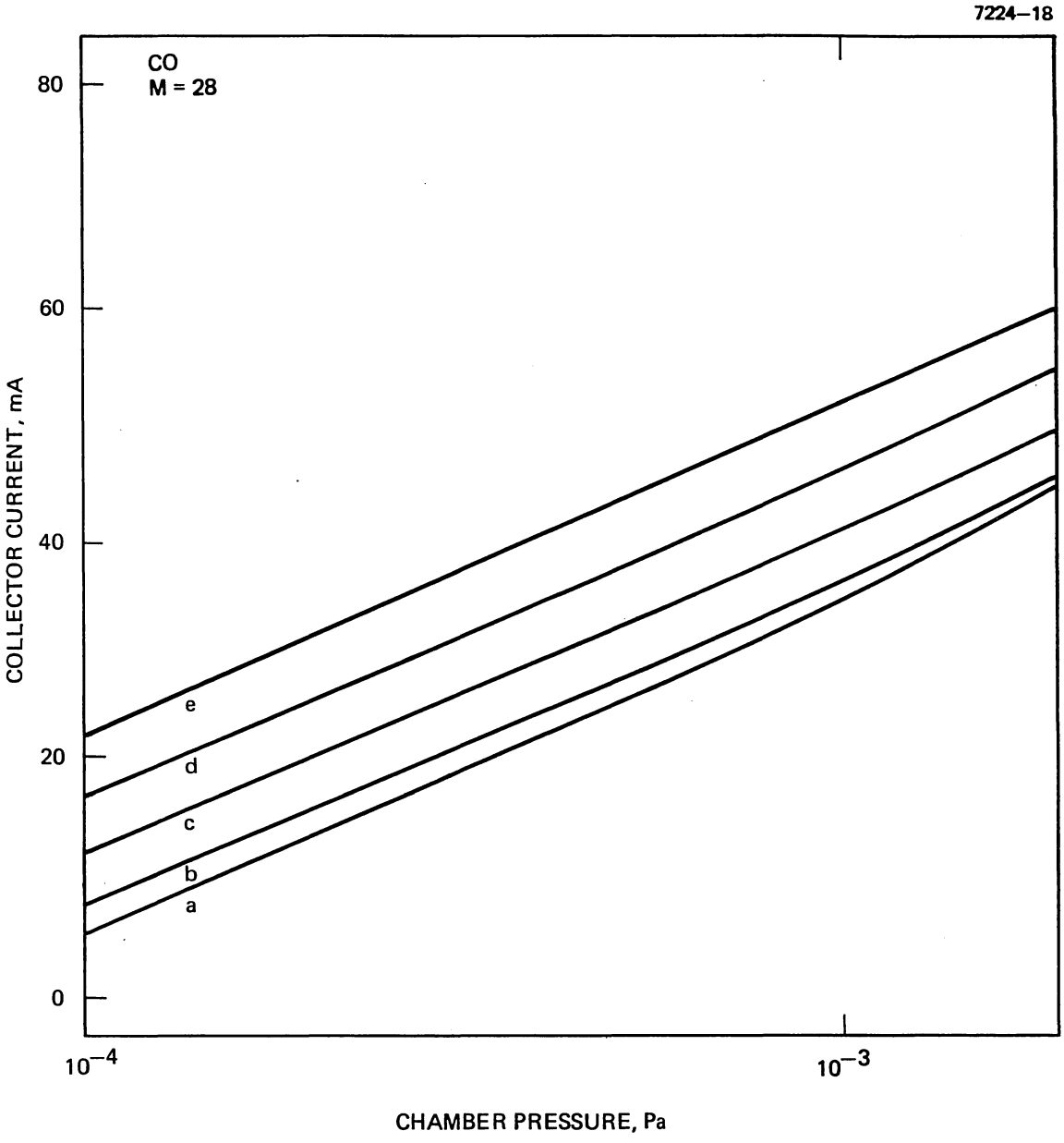

Figure A-1. Calibration curve; mass peak height versus pressure.